People's Democratic Republic of Algeria Ministry of Higher Education and Scientific Research University of 8 Mai 1945Guelma



Faculty: Science and Technology
Department: Civil Engineering and Hydraulics

Domiciliation laboratory: Civil Engineering and Hydraulics

Thesis

Submitted in Candidacy for the Degree of Doctorate in Third Cycle

Field: Science and Technology Stream: Civil Engineering

Speciality: Structures

Presented by: Malek HAMDA

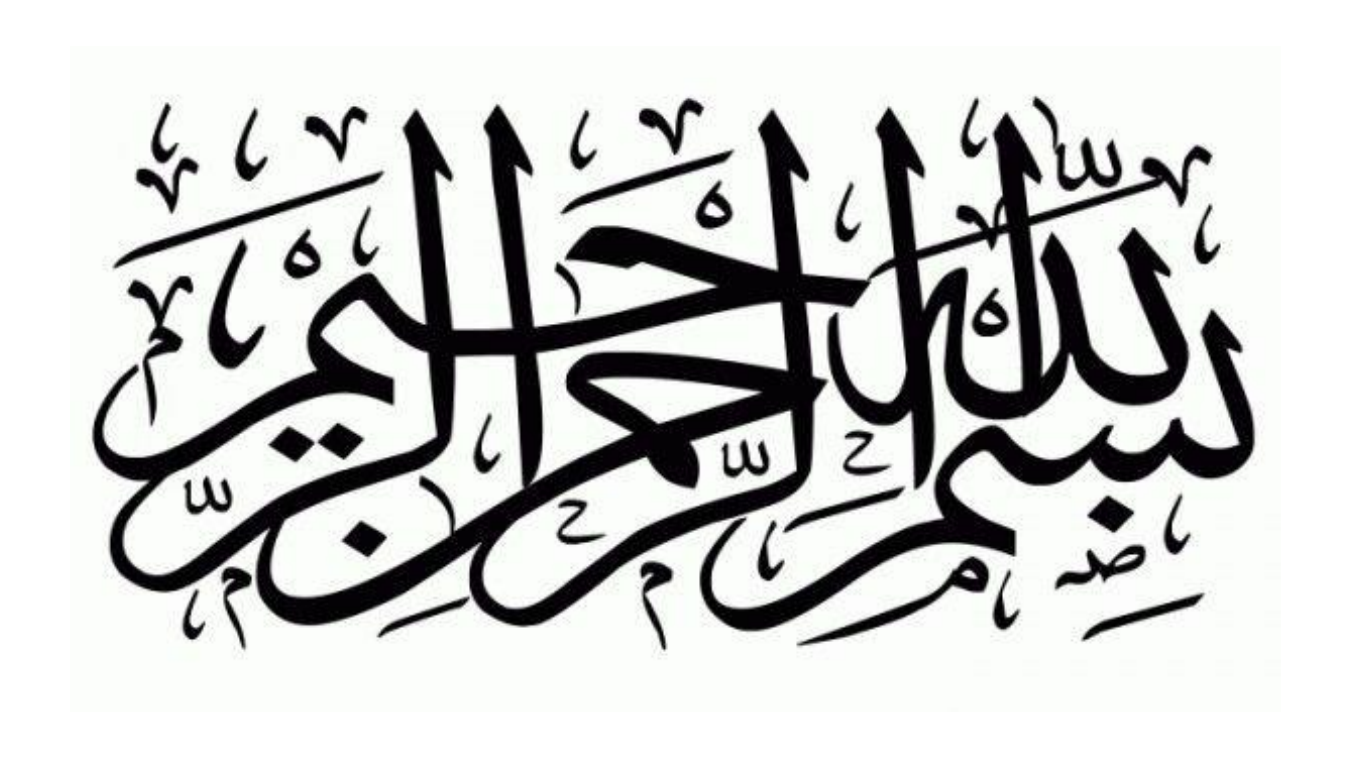
Title

Analysis of some parameters (variation of boundary conditions and reduction of mechanical properties of materials) of high-performance concrete columns, depending on temperature changes

Defended on: 09/07/2025 Before the jury composed of:

Rank	University	
Professor	Univ. of 8 Mai 1945- Guelma	President
Professor	Univ. of 8 Mai 1945- Guelma	Supervisor
MCA	Univ. of Souk Ahras	Co- supervisor
Professor	Univ. of 8 Mai 1945- Guelma	Examiner
Professor	Univ. of Batna 2	Examiner
	Professor MCA Professor	Professor Univ. of 8 Mai 1945- Guelma Professor Univ. of 8 Mai 1945- Guelma MCA Univ. of Souk Ahras Professor Univ. of 8 Mai 1945- Guelma

Academic year: 2024/2025



Dedication

To my beloved parents, Ammar and HALA Zina, whose endless love, sacrifices, and prayers have shaped the person I am today. Your unwavering support has been my greatest strength.

To my dear family, for always believing in me and encouraging me through every challenge.

To my wonderful wife, Ouhiba, who stood by my side through every demanding moment and difficult phase, offering love, patience, and unwavering support. Your faith in me kept me going.

To my precious little baby, Ines, a beacon of joy and motivation, reminding me of the beautiful journey ahead.

And to my best friends, "Elmahdi, Abdelmonim, Abderzak and Kamal", whose encouragement, companionship, and belief in me made this journey more meaningful.

This achievement is as much yours as it is mine.

Acknowledgments

My most distinguished thanks go to my thesis director, **Pr. Benmarce Abdelaziz**, whose continuous encouragement, invaluable guidance, and unwavering support over the past three years have been instrumental in my academic journey. I deeply appreciate your mentorship, patience, and the inspiration you have provided throughout this work. Working under your supervision has been an enriching experience, allowing me to grow both professionally and personally.

I extend my sincere gratitude to my co-supervisor, **Dr. Guergah Cherif**, whose insightful advice and constructive feedback have greatly contributed to shaping this research. Your expertise and dedication have been a source of motivation for me.

I am also deeply grateful to my colleagues and all the staff at the University of Guelma 8 Mai 1945, whose support and collaboration have made this journey more meaningful.

A heartfelt thank you to my beloved family, dear friends, and everyone who has contributed in any way to the completion of this work. Your encouragement, patience, and belief in me have been my greatest source of strength.

Finally, I wish to express my deepest appreciation to all the members of the jury for their time, valuable insights, and evaluation of my work. Your expertise and feedback are truly invaluable.

Abstract

This research examines the fire performance of high-performance concrete (HPC) columns by analyzing the impact of boundary condition variations and the degradation of mechanical properties under elevated temperatures. The study investigates four HPC mixtures: a reference mix (HPC), polypropylene fiber-reinforced HPC (HPCPP), date palm fiber-reinforced HPC (HPCDP), and a hybrid mix combining both fibers (HPCPPQS). The primary objective is to enhance the thermal resistance and structural integrity of HPC through fiber reinforcement.

Experimental results demonstrate that the HPCDP mix exhibits superior fire resistance, retaining 57% of its load-bearing capacity at 650°C while effectively reducing spalling and crack formation. The incorporation of date palm fibers significantly improves the thermal stability of HPC by enhancing moisture dispersion and mitigating internal stresses. Additionally, numerical simulations using SAFIR software were conducted to model RC column behavior under fire exposure, emphasizing the influence of cooling phases and material composition on structural stability.

The findings highlight the effectiveness of fiber-reinforced HPC as a sustainable and costefficient solution for improving fire resistance in structural applications. This study advocates for performance-based fire safety design to enhance the resilience of HPC columns subjected to high-temperature conditions.

Keywords: High-performance concrete, fiber reinforcement, reinforced concrete columns, date palm fibers, SAFIR.

Résumé

Cette recherche examine la performance au feu des poteaux en béton à haute performance (BHP) en analysant l'impact des variations des conditions aux limites et de la dégradation des propriétés mécaniques sous des températures élevées. L'étude porte sur quatre formulations de BHP: un mélange de référence (HPC), un BHP renforcé par des fibres de polypropylène (HPCPP), un BHP renforcé par des fibres de palmier dattier (HPCDP) et un mélange hybride combinant les deux types de fibres (HPCPPQS). L'objectif principal est d'améliorer la résistance thermique et l'intégrité structurelle du BHP grâce au renforcement par fibres.

Les résultats expérimentaux montrent que le mélange HPCDP présente une résistance au feu supérieure, conservant 57 % de sa capacité portante à 650°C tout en réduisant efficacement le délitement et la formation de fissures. L'incorporation de fibres de palmier dattier améliore significativement la stabilité thermique du BHP en favorisant la dispersion de l'humidité et en atténuant les contraintes internes. En outre, des simulations numériques réalisées à l'aide du logiciel SAFIR ont permis de modéliser le comportement des poteaux en béton armé sous exposition au feu, mettant en évidence l'influence des phases de refroidissement et de la composition des matériaux sur la stabilité structurelle.

Les résultats soulignent l'efficacité du BHP renforcé par fibres en tant que solution durable et économiquement viable pour améliorer la résistance au feu des structures. Cette étude plaide en faveur d'une approche de conception basée sur la performance afin de renforcer la résilience des poteaux en BHP soumis à des conditions de températures élevées.

Mots-clés : Béton à haute performance, renforcement par fibres, résistance au feu, poteaux en béton armé, fibres de palmier dattier, SAFIR.

الملخص

تتناول هذه الدراسة أداء أعمدة الخرسانة عالية الأداء تحت تأثير الحريق، من خلال تحليل تأثير تغيّر شروط الحدود وانخفاض الخصائص الميكانيكية عند درجات حرارة مرتفعة. تبحث الدراسة في أربع خلطات من الخرسانة عالية الأداء: الخلطة المرجعية، الخرسانة المسلحة بألياف البولي بروبيلين ، الخرسانة المسلحة بألياف نخل التمر، الهدف الأساسي هو تعزيز المقاومة الحرارية وسلامة الهيكل للخرسانة عالية الأداء من خلال تعزيز ها بالألياف.

أظهرت النتائج التجريبية أن الخلطة تمتلك مقاومة ممتازة للحريق، حيث احتفظت بنسبة 57من قدرتها على التحمل عند 650°C مع تقليل ملحوظ للتشقق والتشظي. كما أن إدراج ألياف نخل التمر حسن بشكل كبير من الاستقرار الحراري للخرسانة من خلال تعزيز توزيع الرطوبة والحد من الإجهادات الداخلية. بالإضافة إلى ذلك، تم إجراء محاكاة رقمية باستخدام برنامج SAFIR لنمذجة سلوك أعمدة الخرسانة المسلحة عند التعرض للنار، مما أبرز تأثير مراحل التبريد وتكوين المواد على استقرار الهيكل.

تؤكد النتائج على فعالية الخرسانة عالية الأداء المسلحة بالألياف كحل مستدام وفعال من حيث التكلفة لتحسين مقاومة الهياكل للحريق. كما تدعو هذه الدراسة إلى تبني نهج تصميم يعتمد على الأداء لتعزيز مقاومة أعمدة الخرسانة عالية الأداء للظروف الحرارية المرتفعة.

الكلمات المفتاحية :الخرسانة عالية الأداء، التدعيم بالألياف، مقاومة الحريق، أعمدة الخرسانة المسلحة، ألياف نخل التمر، المحاكاة باستخدام .SAFIR

Contents

Dedication

Acknowledgments

Abstract

Résumé

الملخص

List of figures

List of tables

General introduction

CHAPTER I: Bibliographical study

I.1 Introduction	04
I.2 Microstructure of hardened concrete	04
I.2.1 Microstructure of cement	04
I.2.2 Water in the hardened cement paste	05
I.2.3 Aggregates	06
I.2.4 Paste-aggregate interface	06
I.3 Development of the concrete material at high temperatures	07
I.3.1 Alterations in the Physical Attributes of Concrete upon Heating	07
I.3.1.1 Evolution of Porosity	07
I.3.1.2 Apparent density variations	08
I.3.1.3 Mass Loss.	08
I.3.2 Effects of temperature on mechanical properties	09
I.3.2.1 Evolution of compressive strength at high temperatures	09
I.3.2.2 Evolution of tensile strength at high temperature	10
I.3.2.3 Evolution of modulus of elasticity in compression	11
I.3.2.4 Evolution of concrete cracking energy (Gf)	11
I.3.2.5 Evolution of Poisson's ratio and elastic shear modulus	12
I.3.3 Residual properties of concrete after heating to different temperatures	13
I.3.3.1 Residual compressive strength	13
I.3.3.2 Influence of aggregate type on residual strength	15
I.3.3.3 Effect of cooling regime on residual strength	15
I.3.3.4 Effect of sample shape on residual resistance.	16

I.4 Review of research on the behavior of structural columns under high temperatures	17
I.4.1 Introduction	17
I.4.2 Experimental studies	17
I.4.3 Numerical studies	19
I.4.4 Codes of practice	20
I.5 Conclusion	21
CHAPTER II: Characterization of materials and formulation of hig	gh-
performance concretes	
II.1 Introduction	24
II.2. Material characterization	24
II.2.1. Cement	24
II.2.2. Mineral additions	25
II.2.2.1. Silica fume	25
II.2.3. Aggregates	27
II.2.3.1 Sand	27
II.2.3.2 Gravel	28
II.2.4. Fibers	29
II.2.4.1 Polypropylene fibers	29
II.2.4.2 Date palm fibers	31
II.2.5 Superplasticizer	32
II.3. Formulation of study concretes	32
II.4. Fabrication and curing of specimens	34
II.5. Thermal treatment cycle of concretes	35
II.6. Procedures for determining the properties of fresh concrete	36
II.6.1. Workability	36
II.6.2 Density	37
II.6.3 Entrained Air	37
II.7. Results and interpretations of the properties of fresh concrete	38
II.7.1. Workability	38
II.7.2 Density	39
II.7.3. Air Entrapment	40
II.8. Conclusion	41

CHAPTER III: Physical and mechanical behavior of high-performance concrete under temperature effects

III.1 Introduction	43
III.2. Physical properties	43
III.2.1. Residual mass loss	43
III.3 Mechanical properties	44
III.3.1. Residual compressive strength	44
III.3.2. Residual tensile strength	45
III.3.3. Dynamic deformation modulus (non-destructive testing)	46
III .4 Results and analysis	48
III .4.1 Residual compressive strength	48
III .4.2 Modulus of elasticity in compression	50
III .4.3 Residual flexural strength	51
III .4.4 Mass loss	52
III .4.5 Ultrasonic Pulse Velocity (UPV)	53
III .4.6 Observations of spalling behavior	54
III .5 Conclusion	57
CHAPTER IV: Study of the load-bearing capacity of columns expose	d to fire
IV.1 Introduction	59
IV.2 Introduction to the SAFIR code	60
IV.2.1 General organization of the software	61
IV.2.2 Beam element presentation (BEAM)	61
IV.2.3 Thermal actions	62
IV.2.4 Thermal analysis	62
•	
•	65
IV.2.5 Structural analysis	65
IV.2.5 Structural analysis	65 69 70
IV.2.5 Structural analysis	65 69 70
IV.2.5 Structural analysis	65 69 70 70
IV.2.7 Comparison and verification of the SAFIR code IV.2.7.1 Validation of the thermal model IV.2.7.2 Structural model validation	
IV.2.5 Structural analysis	

Annex	
Referances	
General conclusion	91
IV.4 Conclusion	90
IV.3.4.5 The influence of different concrete mix types on the residual strength (Nr)	88
IV.3.4.4 Influence of support conditions on load-bearing capacity (N r)	87
IV.3.4.3 Influence of column section dimensions on (N r)	85
IV.3.4.2 Influence of the effective height of the column on (N r)	84
IV.3.4.1 Evolution of (N_r) as a function of temperature	83
$IV. 3.4\ Parametric\ analysis\ for\ evaluating\ vertical\ load-bearing\ capacity\ (N_r)\$	83
IV.3.3.2 Simulation process	82
IV.3.3.1 Temperature distribution in the sections	78
IV.3.3 Thermo-Mechanical modeling of the behavior of columns	78
IV.3.2.2 Structural analysis	78
IV.3.2.1 Thermal analysis of reinforced concrete columns	77
IV.3.2 Numerical analysis process	76

Liste of figures

- Figure I. 1 Scanning electron microscope view of a cement paste [5]
- Figure I. 2 State of water in C-S-H [9]
- Figure I. 3 Total water porosity as a function of conditioning temperature [17]
- Figure I. 4 Pore size distributions in ordinary concrete after exposure to various temperatures [16]
- Figure I. 5 Apparent density variations of concrete with temperature from the bhp 2000 project [17, 18].
- Figure I. 6 Mass loss during heating and rate of mass loss as a function of temperature [19].
- Figure I. 7 Compressive strength variation curves (Eurocode 2 and DTU) [22]
- Figure I. 8 Tensile Strength Test Results Compared With Standards [26].
- Figure I. 9 Evolution Of Modulus Of Elasticity As A Function Of Temperature [22].
- Figure I. 10 Relative Variations In Concrete Cracking Energy With Temperature [29].
- Figure I. 3 Gf Ratio of the 3 concretes tested as a function of temperature [19].
- Figure I. 4 Evolution of the fish coefficient as a function of temperature.
- Figure I. 13 Evolution of high-temperature resistance and residual resistance [30].
- Figure I. 14 Strength reduction of normal and high-strength concrete [30].
- Figure I. 15 Residual compressive strength after heating at different temperatures [37].
- Figure I. 16 Residual strength as a function of aggregate type [41].
- Figure I. 17 Residual resistance for different cooling regimes [20].
- Figure I. 18 Strength reduction in prismatic vs. cubic specimens during heating and cooling
- Figure I. 19 Comparison of fire resistance predictions from simplified equation and test data. [51]
- Figure II. 1 Silica fume
- Figure II. 2 Diffractogram of silica fume
- Figure II. 3 Different aggregates used in the test
- Figure II. 4 The different aggregate tests used in the test
- Figure II. 5 Granulometric analysis of all aggregates
- Figure II. 6 Polypropylene fibers
- Figure II. 7 ATG curve for polypropylene fibers
- Figure II. 8 Illustrations of palm fibers
- Figure II. 9 Flowchart of the proposed method for formulating HPC
- Figure II. 10 Curves of heating and cooling according to temperature
- Figure II. 11 Naberthen furnace (University of Ouargla)
- Figure II. 12 Abrams cone slump test (University Of GUELMA).
- Figure II. 13 Concrete air meter (University of GUELMA).
- Figure II. 14 Variation in the slump for different types of concrete.
- Figure II. 15 Density variation among different types of concrete.
- Figure II. 16 Air entrapment
- Figure III. 1 Measurement of mass loss (LGCH, University of GUELMA)
- Figure III. 2 Compression Test (LGCH, University of Guelma).
- Figure III. 3 Tensile strength test
- Figure III. 4 Measurement of sound speed (NIZOLP Eloued).
- Figure III. 5 Residual compressive strength (a) and reduction factors (b) as a function of temperature.

Figure III. 6 Relative modulus of elasticity of all types of concrete as a function of temperature

Figure III. 7 Residual tensile strength in (a) and reduction factors in (b) versus Temperature

Figure III. 8 Residual Mass loss and reduction factors as a function of temperature

Figure III. 9 Ultrasonic pulse velocity and reduction factors as a function of temperature

Figure III. 10 Condition of the concrete surface at 250 ° C

Figure III. 11 Condition of the concrete surface at 450 ° C

Figure III. 12 Condition of the concrete surface at 650 ° C

Figure III. 13 Condition of the samples after testing their compressive strength after exposure at 450 $^{\circ}$ C

Figure IV 1: Analysis procedure using SAFIR

Figure IV 2: Presentation of the beam element

Figure IV 3: Linear iso parametric elements

Figure IV 4 Description of the beam element.

Figure IV 5 : Comparison between the calculated and measured temperatures on the surface of the steel tube across various tests.

Figure IV 6: Comparison between the calculated and measured temperatures in the reinforcements across various tests.

Figure IV 7: Comparison between the calculated and measured temperatures in the concrete core across various tests.

Figure IV 8:Comparison of temperatures calculated by safir and measured in different

sections: (A) RC+12, (B) RCT11, and (C) RCL12 [5]

 $Figure\ IV\ 9: Axial\ displacement-time\ relationships.$

Figure IV 10: Axial force-time relationships.

Figure IV 11: Behavior of materials exposed to fire. a) Evolution of strength as a function of temperature (T°). (b) Behavior of concrete after cooling.

Figure IV 12: Thermal treatment curve of the column: heating – stabilization – cooling

Figure IV 13: Evolution of temperature distribution during heating phase

Figure IV 14: Evolution of temperature distribution during cooling phase

Figure IV 15: Evolution of the load and applied temperature.

Figure IV 16: Evolution (N_r) of the column as a function of temperature

Figure IV 17: Influence of the variation in the height of the column on (N r).

Figure IV 18: Evolution of (N r / N 20) as a function of section and temperature.

Figure IV 19: Evolution of the bearing capacity as a function of the support conditions.

Figure IV 19: Bearing capacity evolution across different concrete mixes.

List of tables

Table I. 1 Main constituents of ordinary cement

Table II. 1 Chemical composition of cement

Table II. 2 Physical and mechanical characteristics of cement

Table II. 3 Chemical composition of silica fume

Table II. 4 Physical properties of silica fume

Table II. 5 Main physical properties of quarry sand (Annaba) and dune sand (Tébessa)

Table II. 6 Properties of limestone gravel (Annaba)

Table II. 7 Polypropylene fibers characteristics

- Table II. 8 Physical and mechanical properties of the palm fibers used [43].
- Table II. 9 Batches quantities in Kg/m³
- Table II. 10 Types and shapes of specimens with conducted tests.
- Table III. 1 Reduction in residual compressive strength as a function of temperature
- Table III. 2 Reduction factors of compressive strength.
- Table III. 3 Elastic modulus reduction factor
- Table IV. 1: Fire resistance of columns, measured and calculated
- Table IV. 2: Characteristics of the HPC mix
- Table IV. 3: Temperatures at selected points in the column section
- Table IV. 4 Evolution of the bearing capacity as a function of (H) And (T°).
- Table IV. 5: Evolution of the bearing capacity as a function of the column section.
- Table IV. 6: Evolution of the bearing capacity as a function of the support condition

General introduction

High-performance concrete (HPC) is widely used in modern construction due to its high strength, durability, and resistance to harsh environmental conditions. Its low porosity and improved resistance to aggressive agents contribute to the longevity and reliability of structures. However, understanding its behavior under high temperatures is essential, especially in fire conditions. Major fire incidents, such as those in the Channel Tunnel, Mont Blanc Tunnel, and Tauern Tunnel, have revealed significant gaps in knowledge about the effects of extreme heat on concrete, where temperatures can exceed 1000°C.

When exposed to fire, concrete undergoes significant physical and mechanical changes that can compromise its structural integrity. High temperatures cause thermal expansion, internal stress buildup, and loss of strength, often leading to cracking or spalling. Research has shown that adding polypropylene fibers to concrete can reduce spalling by increasing microporosity, allowing gases to escape and lowering internal pressure.

Although fire safety regulations aim to prevent and control fires, real-life incidents often result in severe structural damage despite these measured. Current fire resistance assessments mainly focus on factors such as element dimensions and reinforcement cover but do not always consider the overall stability of structures under fire conditions.

This research aims to improve the understanding of HPC behavior at high temperatures, with a particular focus on reinforced concrete columns. by studying the effects of heat exposure and the role of materials such as granulated slag fillers, polypropylene fibers, and date palm fibers. This research work seeks to provide valuable insights for improving fire-resistant concrete structures.

In this context, the present thesis is structured into four chapters.

Chapter I: this chapter presents a synthesis of research on the evolution of the physical and mechanical properties of concrete subjected to high temperatures. The results found in the literature vary and are sometimes contradictory. First, the hypotheses concerning the structure of concrete are outlined, followed by a description of the changes in chemical composition and microstructure due to heat exposure. The thermal deformations of concrete and its constituents are then analyzed. The chapter also examines the evolution of mechanical properties, such as compressive strength, tensile strength, and elastic modulus, under different temperature conditions. The impact of testing methods on these properties is also discussed.

Furthermore, this chapter includes a review of research on the fire behavior of reinforced concrete columns. The fire resistance of these columns is influenced by multiple factors, such as fire exposure conditions, load levels, and concrete properties—many of which are not fully

considered in current fire design methodologies. Existing fire resistance provisions, mainly based on prescriptive approaches, assume failure when the steel reinforcement reaches a critical temperature but often overlook essential structural interactions, such as column-beam behavior and biaxial bending effects. A review of experimental and numerical studies highlights the existing gaps in knowledge, particularly concerning high-performance concrete (HPC) columns. Additionally, the limitations of current fire resistance design codes, including Eurocode 2, ACI-318, and AS 3600, are discussed.

Chapter II: This chapter defines and justifies our foundational choices regarding the compositions of the materials studied. We conduct a systematic optimization of high-performance concrete (HPC) formulations, both with and without fibers. This includes selecting constituents such as cement, aggregates, silica fume, and additives to enhance performance characteristics.

Additionally, the roles of polypropylene fibers and date palm fibers are explored, focusing on their ability to improve resistance to cracking and spalling, especially under high temperatures. The chapter concludes with experimental results that characterize how polypropylene fibers and date palm fibers influence the fresh properties of HPC, including workability, setting time, and density. These findings underscore the potential for optimized HPC formulations to enhance structural durability and resilience

Chapter III: presents the experimental protocols and analyzes results related to key properties of high-performance concrete (HPC) subjected to heating-cooling cycles at temperatures of 20°C, 250°C, and 650°C.

We begin by detailing the methodologies for sample preparation and testing. Key assessments include:

- 1. Mass loss: Measured to evaluate material degradation and changes due to elevated temperatures.
- 2. Accessible porosity: Assessed to understand permeability and structural integrity.
- 3. Residual Compressive Strength: Evaluated to determine load-bearing capacity after exposure to heat.
- 4. Residual tensile strength: Similar to compressive strength, this indicates the material's ability to resist tensile forces.
- 5. Elastic modulus (Non-Destructive Testing): Measured to assess stiffness and structural integrity without damaging the samples.

The chapter concludes with a comparative analysis of HPC performance at different temperatures, discussing the implications for its use in fire-prone environments.

Chapter IV: The first part provides a comprehensive overview of the SAFIR software, outlining its theoretical foundations, algorithms, and the validation processes employed to ensure its accuracy and reliability in simulating fire behavior and structural response.

The second part is dedicated to the theoretical study of the resistance of columns, emphasizing the principles governing their structural integrity. This section elaborates on the key factors influencing column performance under various loading conditions.

The core of this chapter is focused on numerical simulations designed to evaluate the load-bearing capacity of reinforced concrete columns when subjected to vertical loads. The analysis incorporates several critical physical and mechanical parameters, including:

- Fire considerations: The duration of heating, modeled to reflect realistic fire scenarios, enabling the assessment of how thermal effects impact structural performance.
- Reinforced concrete column parameters: This includes the height and thickness of the columns, as well as various support conditions that influence their stability and loadcarrying capabilities.

Through these simulations, the chapter aims to provide valuable insights into the behavior of columns in fire conditions, thereby contributing to the development of more resilient structural designs.

General conclusion and perspectives

As a general summary of this research conducted on HPC and HPC reinforced with fiber under high temperature. This study aimed to contribute to a better understanding of material performance under fire conditions and explore the potential of fiber reinforcement in enhancing fire resistance.

Future research should focus on the long-term durability of HPC after fire exposure, the optimization of numerical models for more accurate predictions, and the integration of improved formulations into fire-resistant design standards. The use of sustainable materials, such as date palm fibers, also presents an interesting avenue for further investigation

Chapter I: Bibliographical study

I.1 Introduction

Reinforced concrete structures can withstand natural disasters such as earthquakes and fires, but these events pose a significant threat to their structural integrity, causing severe damage. Fires, in particular, can be devastating, affecting not only the load-bearing parts but also the aesthetic aspects of buildings. When exposed to fire, concrete can undergo dramatic changes, reaching temperatures exceeding 1000°C, depending on the intensity and duration of the fire. This chapter provides a comprehensive understanding of concrete's thermal and mechanical behavior when exposed to high temperatures to help mitigate potential damage.

I.2 Microstructure of hardened concrete

Concrete is composed of the matrix (hardened cement paste) and aggregates (gravel and sand), resulting in a heterogeneous microstructure due to the wide range of aggregate sizes and hydration products, which are sensitive to hydration and preservation conditions like temperature and relative humidity. Understanding the microstructure of hardened concrete is essential to prevent catastrophic failures during disasters. With this knowledge, we can confidently ensure the safety and longevity of concrete structures.

I.2.1 Microstructure of cement

Cement is a hydraulic binder that, when mixed with water, forms strong, durable materials, even underwater. Portland cement, the most widely used binder, consists of clinker and gypsum [1]. Clinker is produced by heating limestone (80%) and clay (20%) at 1,450°C in a kiln [2]. Gypsum (CaSO4·2H2O) is crucial in Portland cement, preventing "flash setting" by forming ettringite crystals on C3A grain surfaces, delaying hydration and hardening [3]. This process ensures controlled setting, avoiding rapid hardening due to insufficient SO42- ions [4]. Table I.1 lists the main dehydrated components and mineral composition of Portland cement.

Table I.1:Main Constituents of Ordinary Cement

Designation	Exact chemical formula	Simplified chemical	Proportion in ordinary
		formula	cement
Tricalcium silicate	3CaO.SiO2	C3S	60 to 65%
Dicalcium silicate	2CaO.SiO2	C2S	20 to 25%
Tricalcium aluminate	3CaO.Al2O3	C3A	8 to 12%
Tetracalcium	4CaO.Al2O3.Fe2O3	C4AF	8 to 10%
alumino-ferrite			

When water and cement mix, they trigger hydration reactions, forming durable hydrate compounds. Hydration involves chemical reactions between water and cement, transforming a fluid suspension into a solid. Key hydrates include CSH gel (hydrated calcium silicate), calcium hydroxide (Portlandite), and hydrated calcium aluminates with ettringite. This process

creates the cement's strength and structure as shown in the Figure I.1.

These hydrates primarily arise from the cement's dicalcium and tricalcium silicates, as indicated by the simplified reaction (I.1).

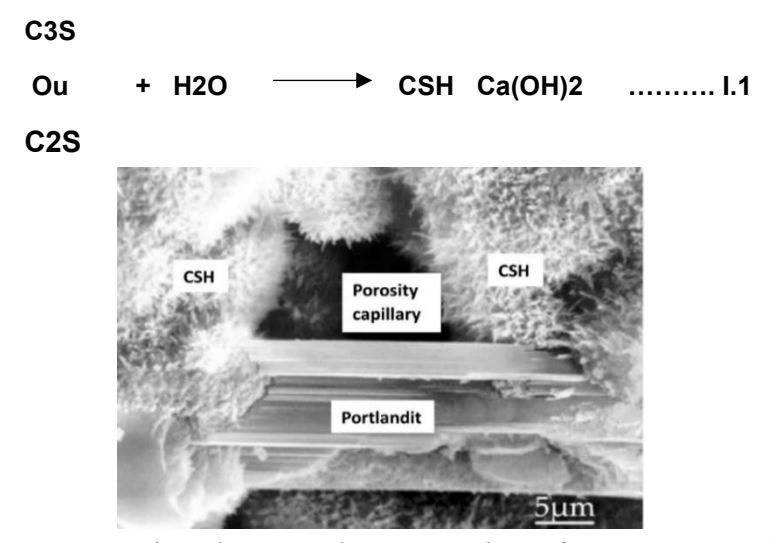


Figure I.1: Scanning electron microscope view of a cement paste [5]

The CSH gel is the main component of hydrated Portland cement, making up 50% to 70% of its weight. It is essential for providing strength, though its structure remains poorly defined. The term "CSH gel" reflects its amorphous nature, low crystallinity, and inclusion of water molecules [6]. Portlandite, the only solid phase in cement paste that appears relatively pure, forms hexagonal flakes, often in stacked formations among partially hydrated cement grains. Its large crystal size results in a small specific surface area, leading to weak bonding. High concentrations are found at the transition zone (between cement paste and aggregates) or near air bubbles. In confined spaces, portlandite can also appear in an amorphous form [7].

I.2.2 Water in the hardened cement paste

Water plays a dual role in cement paste, enhancing fluidity and workability initially, then aiding in solid particle connections during hardening. However, it also introduces drawbacks like increased porosity, reduced strength, harmful substances, and shrinkage or creep. Water in cement paste is classified based on its binding [8]:

- 1. Free (capillary) water: Fills pores and migrates first, evaporating at 30°C–120°C.
- 2. Adsorbed water: Bound physically (Van Der Waals forces) or chemically (modified molecular structure).
- 3. Chemically bound water: Reacts with cement's anhydrous elements, existing in three forms within the C-S-H structure, classified by bonding energy (see Figure I.2) [9].

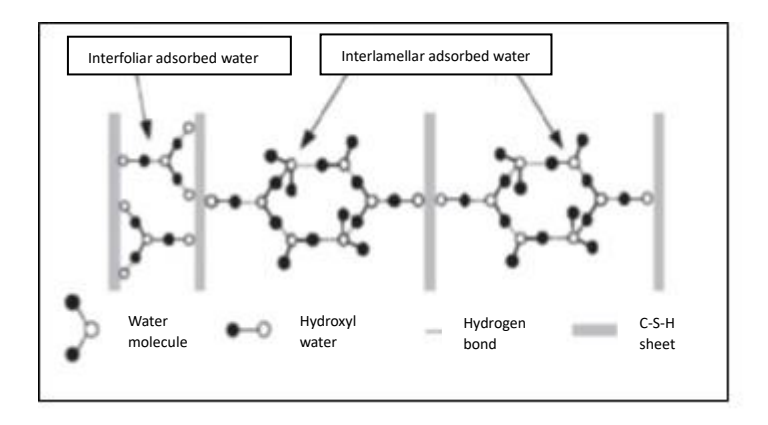


Figure I.2: State of water in C-S-H [9]

I.2.3 Aggregates

Aggregates make up 60-80% of concrete volume and are sourced from natural (mechanically processed minerals), artificial (processed materials like expanded shale), or recycled (crushed concrete) origins. Reactive aggregates, such as limestone, bond strongly with cement paste through chemical reactions, while siliceous aggregates, being neutral, form weaker bonds [10]. The selection of aggregates depends on their mineralogical origin, shape, and size distribution, which significantly influence concrete's performance. Proper aggregate choice is crucial for optimizing concrete strength and durability.

I.2.4 Paste-aggregate interface

In the hydration process of concrete, a critical bond forms between the cement paste and granular aggregates, creating the "interfacial transition zone (ITZ)." The properties of this zone depend on the aggregate type. Limestone aggregates, for example, form strong bonds with cement paste, reducing permeability due to reactions between calcium carbonate (CaCO3) and tricalcium aluminate, forming calcium monocarbo-aluminates (C3A-CaCO3H11) [11, 12]. In contrast, neutral aggregates result in an ITZ with lower mechanical strength and higher gas permeability, making it a potential weak point in the structure.

In conventional concrete, the ITZ is a porous, mechanically weaker section compared to the surrounding cement paste. Its higher porosity facilitates mass transport, compromising structural integrity and durability [13, 14]. The ITZ thickness, typically below 50 µm, depends on aggregate size and the water-to-cement (W/C) ratio [15]. This underscores the importance of aggregate selection and concrete composition in ensuring performance and longevity.

I.3 Development of the concrete material at high temperatures

Under the influence of high temperatures, concrete undergoes numerous physicochemical phenomena and transformations that change its microstructure. The simultaneous changes in the cement matrix and the aggregates lead to a strong deterioration of the concrete microstructure and to changes in its mechanical, thermal and transport properties. These

modifications also lead to the formation of free water in the material and thus to an increase in interstitial pressure. In addition to the direct effects on these two basic components, behavioral incompatibilities between them contribute to specific damage in the concrete material.

I.3.2 Alterations in the Physical Attributes of Concrete upon Heating

I.3.2.1 Evolution of Porosity

Concrete is a biphasic porous material, consisting of a solid phase and a porous phase.

Research indicates that porosity escalates with temperature [16-17].

This increase is partly due to the expansion of the total pore volume as well as the microcracking caused by differential expansion between the paste and the aggregates. Figure I.3 illustrates the variation in total porosity as a function of temperature for ordinary concrete (OC) and high-performance concrete (HPC), as measured by [17] using the water saturation method.

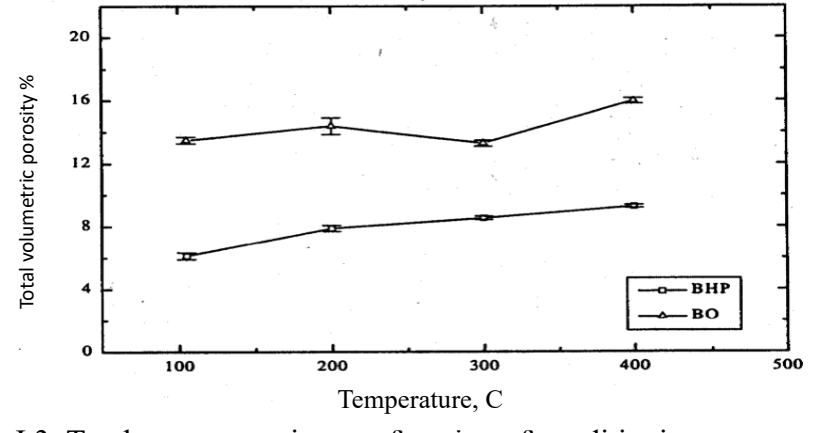


Figure I.3: Total water porosity as a function of conditioning temperature [17]

From 105°C to 400°C, there's a 3% increase in porosity for ordinary concrete (OC) and a 0.9% rise for high-performance concrete (HPC). This elevation in porosity is linked to the release of water, both from within the pore network and in a chemically bonded state.

A study observed the change in total porosity with temperature in ordinary concrete (OC) with a compressive strength of 38.1 Mpa and high-performance concrete (HPC) with a compressive strength of 61.1 Mpa [16], using mercury intrusion porosimetry. The findings revealed a minimal increase in porosity between 22°C and 120°C. This minimal increase indicates that while free water is released in this temperature range, the concrete's microstructure remains largely unaffected. Figure I.4 presents the pore size distributions in ordinary concrete obtained at various temperatures through mercury intrusion porosimetry.

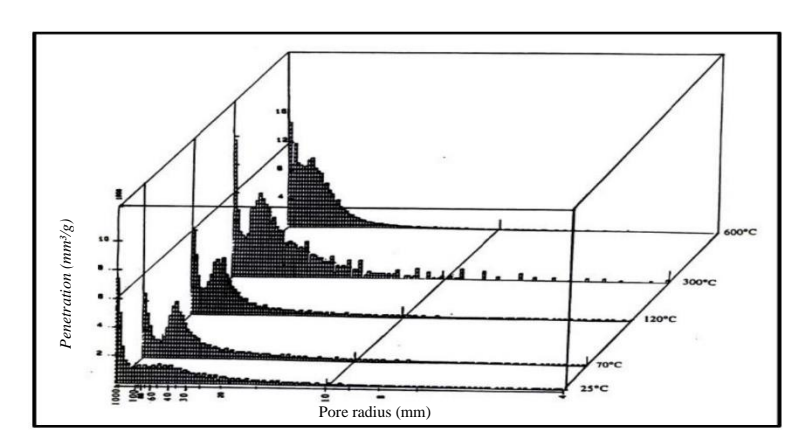


Figure I. 4 Pore Size Distributions in Ordinary Concrete After Exposure to Various Temperatures [16]

I.3.2.2 Apparent density variations

Measurements of the bulk density for three high-performance concretes (HPC) and one ordinary concrete (OC) (M75SC, M75C, M100C, and M30C) are depicted in Figure I.5 This figure illustrates a slight reduction in density across the temperature range from 100°C to 400°C. Notably, a difference in densities between ordinary concrete (OC) and high-performance concrete (HPC) at 100°C can be observed, with values of 2.28 and 2.43 [g/cm³], respectively. These results stem from the HPC 2000 Project [17, 18].

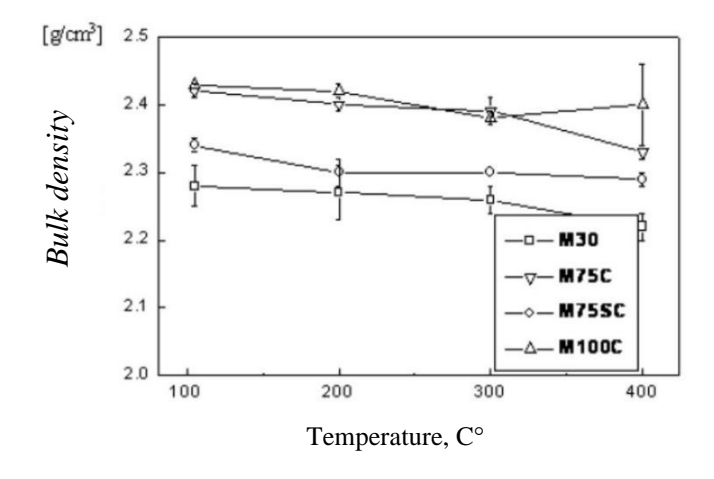


Figure I.5: Apparent density variations of concrete with temperature from the HPC 2000 project [17, 18].

I.3.2.3 Mass Loss

During the heating of concrete, the mass decreases due to the evaporation of water and the gradual dehydration of the cement paste hydrates. Figure I.6 displays a characteristic curve of mass loss during heating, as well as the curve of the rate of mass loss [19].

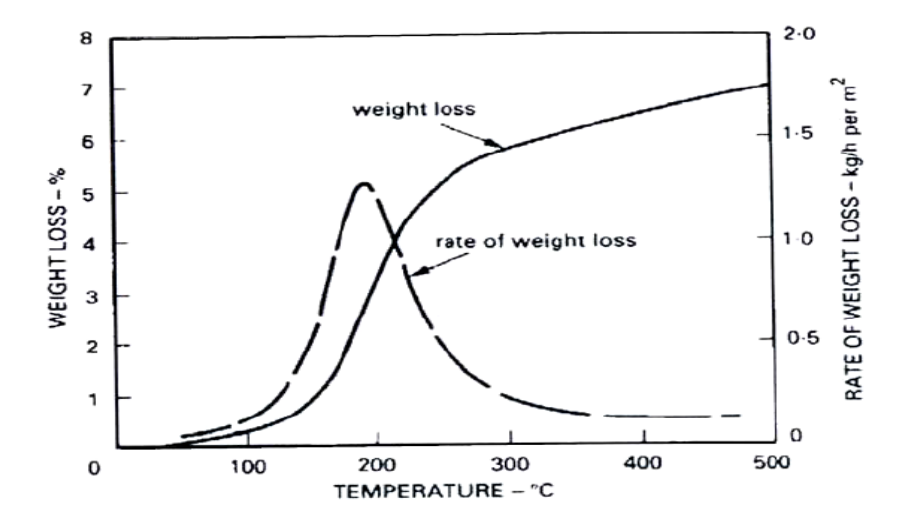


Figure I.6: Mass loss during heating and rate of mass loss as a function of temperature [19].

I.3.4 Effects of temperature on mechanical properties

Under the influence of temperature, concrete undergoes significant physico-chemical changes which influence the evolution of its mechanical properties with temperature. Dehydration, transformation reactions, pore pressure and differential expansion between cement paste and aggregates all have significant effects on the strength of concrete at high temperatures. These changes appear to be irreversible, due to the irreversible nature of the dehydration and breakdown of the concrete microstructure that occur.

I.3.4.1 Evolution of compressive strength at high temperatures

To characterize the variation of concrete compressive strength with temperature, several experimental methods are used:

- Steady-state method: The specimen is heated to a specific temperature, then loaded at a controlled rate.
- Transient state method: The specimen is loaded first, held at a fixed load, and then heated at a controlled rate.
- Residual state method: The residual compressive strength is measured after cooling to room temperature.

Hot specimens generally exhibit higher compressive strength than cooled ones, with additional strength loss observed during cooling compared to the maximum temperature [20]. The evolution of compressive strength with temperature depends on factors like binder and aggregate type, water/cement ratio, heating rate, and additions, with aggregate type and G/C ratio being the most influential [21]. Figure I.7 illustrates Eurocode 2 and DTU curves for various concrete types [22].

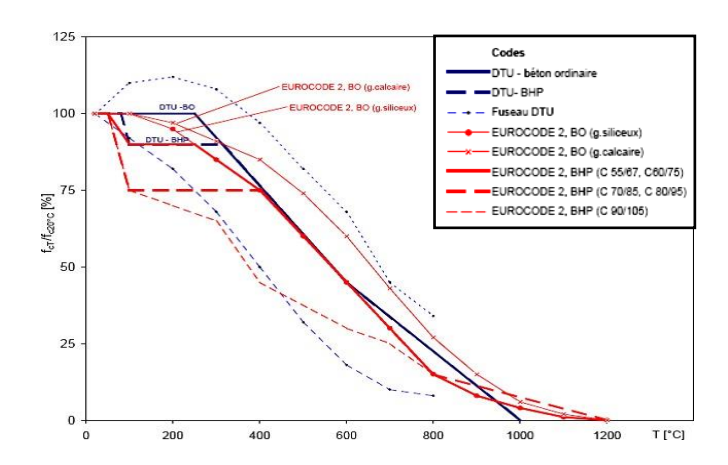


Figure I.7: Compressive strength variation curves (Eurocode 2 and DTU) [22]

Compressive strength decreases slightly up to around 400°C, then drops significantly between 400°C and 800°C. At 800°C, strengths reach values of less than 20% and 30% of the value at ambient temperature for siliceous and limestone concretes respectively.

I.3.4.2 Evolution of tensile strength at high temperature

Most tests on the evolution of tensile strength as a function of temperature are carried out after cooling by splitting [23]. Tensile strength partly determines the thermal stability of RILEM TC44 concretes (spalling and bursting) [24]. Residual tensile strength tests were conducted, revealing that the values obtained through direct tension are the most representative. Additionally, it is shown that residual tensile strength is somewhat lower than tensile strength at elevated temperatures [25, 21].

Figure I.8 illustrates the residual tensile strengths determined through both splitting and direct tension methods, alongside the direct hot tensile values. These findings are compared with those outlined in Eurocode 2 and DTU, with the DTU curve showing higher values than those obtained experimentally. The results indicate that tensile strength is more adversely affected by temperature compared to compressive strength. Specifically, from 150°C onward, direct tensile strength decreases by 15-20%, while compressive strength exhibits a decline of only 8-9%. Following exposure to 500°C, concrete retains 60 to 63% of its compressive strength, in contrast to only 42 to 53% of its tensile strength [24, 26].

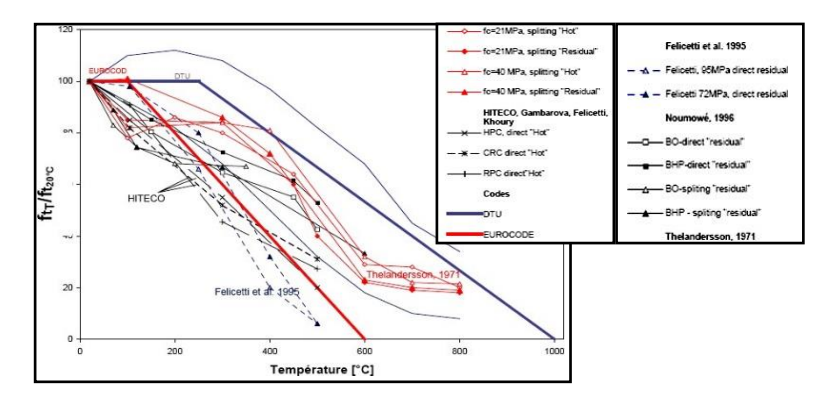


Figure I.8: Tensile strength test results compared with standards [26].

I.3.4.3 Evolution of modulus of elasticity in compression

The variation in the modulus of elasticity is primarily influenced by the microstructure of the cement paste, particularly due to increased material damage from dehydration and matrix cracking. Higher temperatures accelerate the creep process in the short term, leading to a reduction in the modulus of elasticity [27]. These changes are affected by several factors, including the initial elastic modulus, the water content of the concrete, the nature of the aggregates, and the heating rate [28, 27]. Figure I.9 presents experimental values alongside those provided by normative codes [22]. The modulus consistently decreases across all types of concrete tested (e.g., BV, BAP), exhibiting a monotonically decreasing trend with a noticeable dispersion in the experimental results.

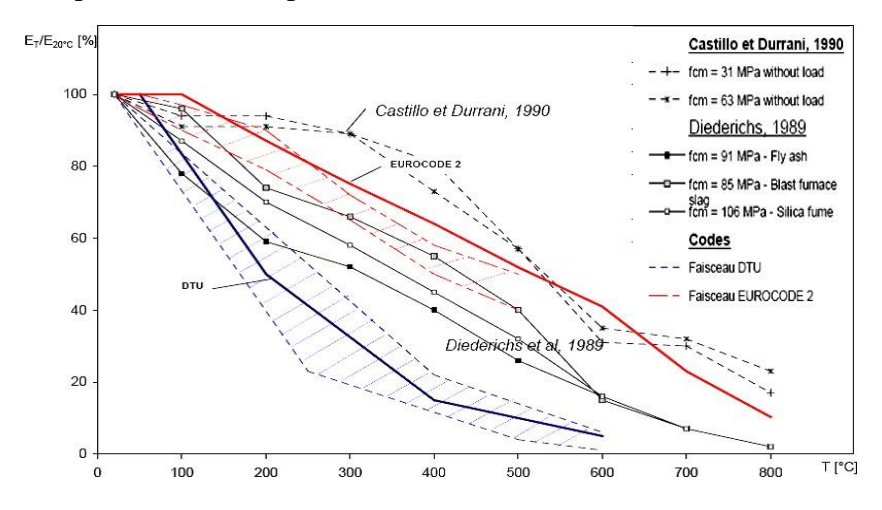


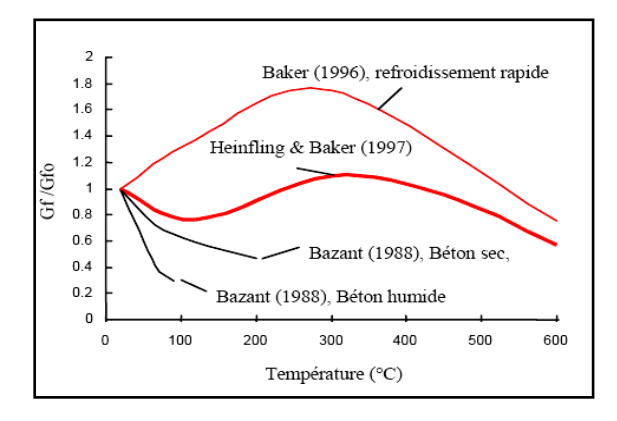
Figure I.9: Evolution of modulus of elasticity as a function of temperature [22].

I.3.4.4 Evolution of concrete cracking energy (Gf)

Cracking energy is defined as the energy required to create a unit surface crack. The degradation of the modulus of elasticity, compressive strength, and tensile strength results in a variation of cracking energy as a function of temperature. An analysis of the work conducted

by various authors [29, 30] reveals a significant dispersion in the results, primarily attributed to factors such as different heating and cooling rates, testing conditions (hot or cold), concrete compositions, grain sizes, specimen geometries, storage conditions, and cement types.

Figure I.10 illustrates the evolution of the mean cracking energy with temperature. Additionally, Figure I.11 presents the evolution of the Gf/Gf0 ratio at 20°C, 120°C, 250°C, and 400°C, as obtained by [31], for three types of concrete tested as a function of temperature.



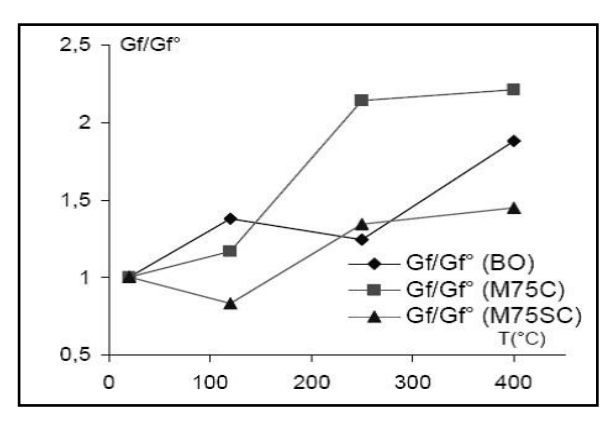


Figure I.10: Relative variations in concrete cracking energy with temperature [29].

Figure I.10: Gf Ratio of the 3 concretes tested as a function of temperature [19].

The variation of concrete cracking energy with temperature is a critical parameter for the thermomechanical behavior model in simulations, as specified by [29]. It serves as a coupling term between thermal and mechanical degradation in concrete [19].

I.3.4.5 Evolution of Poisson's ratio and elastic shear modulus

The study of concretes with siliceous aggregates tested up to 400°C indicates that Poisson's ratio values evolve with temperature in a manner similar to that of the shear modulus. Research conducted on cement paste within a temperature range of 20 to 300°C revealed a 20% decrease in Poisson's ratio at 150°C, followed by a 7.5% increase at 300°C [32].

In tests performed, Poisson's ratio was evaluated after cooling to room temperature under two different cooling regimes: a slow cooling regime (where the specimen was left in the oven) and a rapid cooling regime (where the specimen was rapidly cooled with a jet of cold water for half an hour) [33]. Figure I.12 displays the results from [34] and [33], as reported by [35], illustrating the evolution of the elastic shear modulus (G) and Poisson's ratio (v) of concretes as a function of temperature. Additionally, the work shows that G varies similarly to the modulus of elasticity (E) [46].

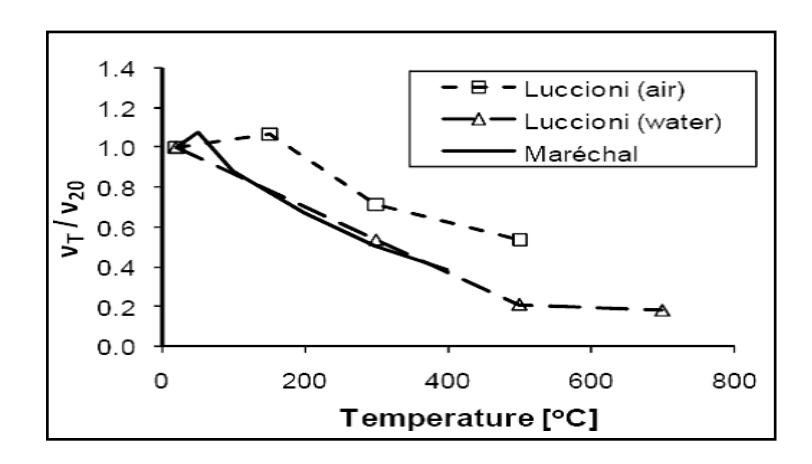


Figure I.12: Evolution of the fish coefficient as a function of temperature

I.3.5 Residual properties of concrete after heating to different temperatures

Reinforced concrete structures generally behave well in fire. Most concrete buildings damaged by fire can be repaired and put back into use, even after severe fires, damaged structural elements can be repaired to have minimum strength, stiffness and ductility again. To assess and repair damaged elements, it is essential to understand the effect of temperature on the residual properties of concrete, in particular the stress-strain relationships used to predict the behavior of structures after cooling.

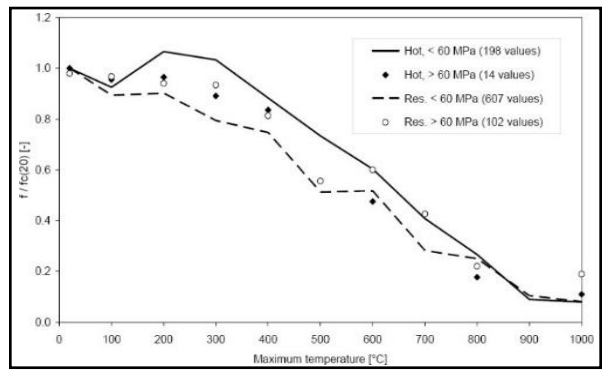
Numerous studies have been carried out on the residual mechanical properties of concrete after exposure to elevated temperatures, such as compressive strength, tensile strength, and modulus of elasticity: [37, 38, 39, 61, 62, 63, 64,65]. The results obtained by different works in different countries are not easy to compare quantitatively, due to differences in materials, sample sizes and test conditions.

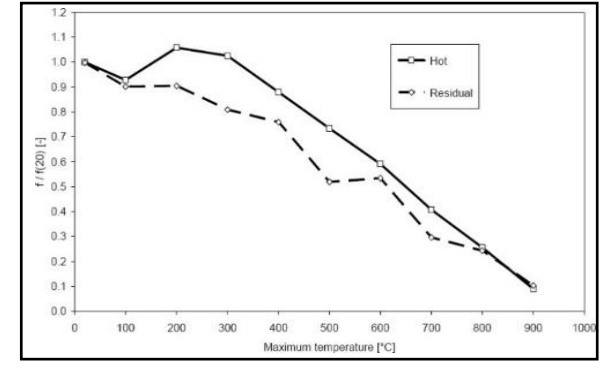
I.3.5.1 Residual compressive strength

The compressive strength and stiffness of concrete significantly decline when exposed to high temperatures during a fire, and this degradation persists even after the temperature returns to ambient conditions. Figure I.13 illustrates this decline, showing the reduction in compressive strength during heating (solid line) and the residual strength after cooling (dotted line). A further decrease in strength is observed post-cooling, likely due to the formation of additional microcracks caused by thermal gradients or opposing stresses between the cement paste and aggregates during heating and cooling.

The residual strength curve displays two peaks at 500°C and 700°C, which may result from an insufficient number of test results or physicochemical changes in the concrete during cooling [30-20]. Figure I.14 compares the compressive strength at high temperatures and residual

strength for ordinary concrete and high-strength concrete (HPC), with a strength threshold set at 60 MPa. Ordinary concrete shows a significant additional drop in strength after cooling (solid vs. dashed line), while HPC exhibits minimal degradation up to 400°C. Interestingly, at temperatures between 600°C and 1000°C, HPC's residual strength after cooling tends to exceed its strength at high temperatures, highlighting its superior thermal resilience. These findings emphasize the importance of material selection in enhancing fire resistance and





structural performance.

Chang et al. [37] studied the residual strength of concrete by testing 12 cylindrical specimens (8 with fc28=40MPa and 4 with fc28=27MPa) made from siliceous aggregates and Portland cement. Specimens were exposed to temperatures from 100°C to 800°C in 100°C increments, heated at 1–4.5°C/min, and stabilized for 1.5–2.5 hours to ensure uniform heat distribution.

Figure I. 13 Evolution of high-temperature resistance and residual resistance [30].

Strength (f') at 200°C retained ~90% of initial strength, dropping to 65%, 40%, and 15% at 400°C, 600°C, and 800°C, respectively, with a sharper decline above 200°C. Equations (I.1) and (I.2) [37-40] aligned well with test data, closely matching Abrams' experimental results [50] and EN 1994-1-2 values. Figure I.15 illustrates these findings.

$$f_{cr}^{'}/f_{c}^{'} = 1.008 + \frac{T}{450 \ln (T/5800)} \ge 0,$$
 $20^{\circ}C < T \le 800^{\circ}C$ (I.1)

$$f_{cr}^{'}/f_{c}^{'} = \begin{cases} 1.01 - 0.00055T & ,20^{\circ}C < T \le 200^{\circ}C \\ 1.05 - 0.00125T & ,20^{\circ}C < T \le 800^{\circ}C \end{cases}$$
 (I.2)

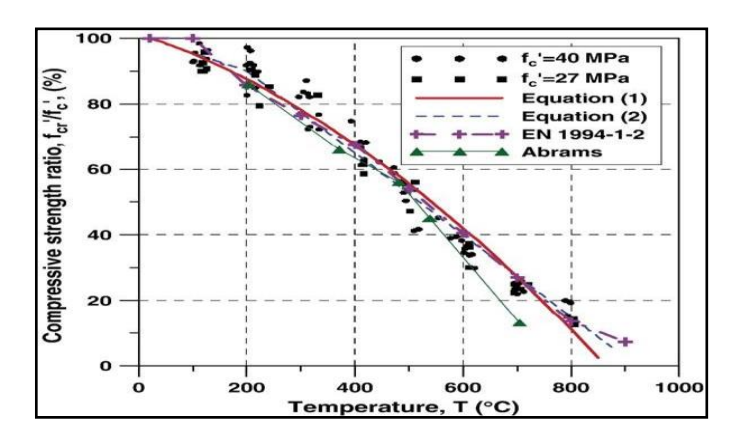


Figure I.15: Residual compressive strength after heating at different temperatures [37].

I.3.5.2 Influence of aggregate type on residual strength

Test results for 5 different cement mixes (350Kg/m3) to 450kg/m3) and using different aggregates (siliceous, calcareous and basaltic) are reported by [41], figure I.16 shows the results obtained for mix1 (cement: 32.5 R and c = 350 kg/m3).

- Basalt- and limestone-based concretes are less affected by temperature than siliceous concretes, at least up to 400° C.
- Overall, siliceous and calcareous concretes lose more than 2/3 of their initial strength after being heated to 600°C, whereas basalt concretes lose less (around 1/2)

In the T = 20-600°C range, normal-strength concretes (fc20 = 41-66 MPa) lose just over 60%.

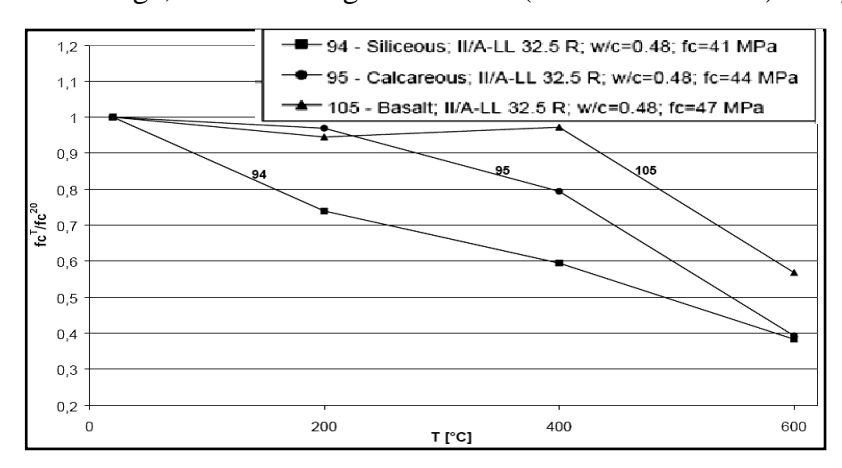


Figure I. 16 Residual strength as a function of aggregate type [41].

I.3.5.3 Effect of cooling regime on residual strength

The heating level and cooling regime significantly influence concrete degradation rates [42]. Faster cooling increases the temperature gradient, causing greater concrete damage. Even with natural cooling, the internal temperature of concrete remains higher than during heating [42]. Figure I.17 illustrates the residual strength evolution for two cooling regimes (air and water), showing that strength loss during cooling is likely due to thermal stresses [20]. These stresses

arise from differences in thermal deformation between aggregates and cement paste, despite uniform heat flow. The divergence in the curves in Figure I.17 is attributed to thermal gradients between the sample's surface and interior.

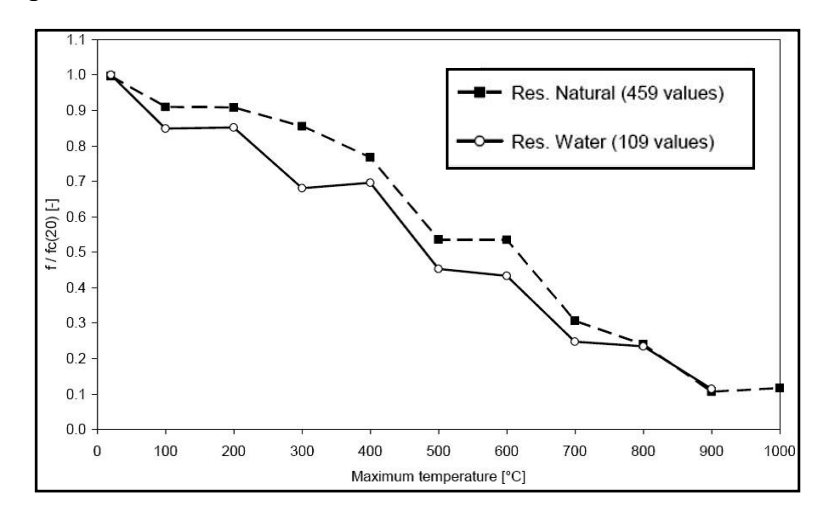


Figure I.17: Residual resistance for different cooling regimes [20].

I.3.5.4 Effect of sample shape on residual resistance

The shape of specimens significantly affects residual strength after cooling [20]. Figure I.18 compares residual strength evolution for cubic (100 mm or 150 mm) and prismatic (circular or square base, height-to-base ratio of 2–3) specimens. Prismatic specimens exhibit greater strength reduction during heating and cooling compared to cubic ones. While fracture mechanisms differ between thin cubic and prismatic specimens, they remain consistent across room temperature, heated, and cooled conditions. The variation is likely due to differing aspect ratios, influencing thermal gradient distributions. Notably, only cubic specimens show strength increases at 200°C and 300°C. The additional strength reduction during cooling is most pronounced for cubes below 500°C and for prismatic specimens above 400°C.

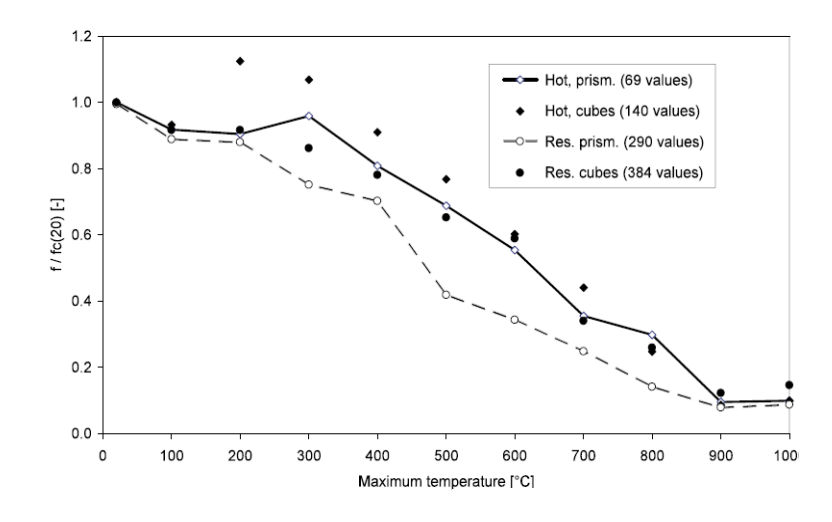


Figure I. 18 Strength reduction in prismatic vs. cubic specimens during heating and cooling [20]

I.4 Review of research on the behavior of structural columns under high temperatures I.4.1 Introduction:

The fire resistance of reinforced concrete (RC) columns is influenced by several factors, including fire scenarios, exposure conditions, load levels, restraint, and concrete strength. However, many of these factors are not adequately considered in the fire design of RC columns. Current code provisions for evaluating fire resistance are based on a prescriptive methodology, which assumes that a column fails when the steel reinforcement reaches a critical temperature. These provisions are derived from standard fire tests conducted on RC columns.

Since the 1970s, numerous experimental and analytical studies have been carried out to better understand the behavior of RC columns under fire conditions. However, most of these studies have focused on standard fire scenarios, often neglecting critical aspects such as structural interactions (e.g., column-beam interactions), biaxial bending, and realistic fire conditions. Furthermore, due to a lack of data on the high-temperature thermal and mechanical properties of newer types of concrete, variations in these properties are not accounted for in fire resistance evaluations.

This section provides a detailed review of the state-of-the-art research on the fire performance of RC columns, encompassing both experimental and analytical studies. It also examines the fire resistance provisions outlined in various codes and standards, highlighting gaps and areas for improvement in current practices.

I.4.2 Experimental studies

In recent years, the construction industry has shown great interest in applications of high-performance concrete (HPC) due to its superior performance such as higher strength and better durability. Although normal strength concrete (NSC) generally exhibits good fire resistance, HPC may be susceptible to fire due to faster deterioration of strength and a higher probability of explosive spalling under fire conditions when compared with NSC [43], [44]. Since HPC is normally used in columns to utilise its high compressive strength, special attention should be paid to fire design of columns made of HPC.

The behaviour of HPC columns under fire conditions has been experimentally investigated by a number of researchers. Aldea et al. [45] tested six reinforced concrete (RC) columns to investigate the effect of concrete strength and steel reinforcement (number and diameter of reinforcing bars). The columns were made of NSC (20–50 MPa) and HPC (90 MPa) with two different steel reinforcement configurations subjected to axial loading that equals 50% of

column design strength. It was found that HPC columns exhibited severe corner spalling which led to premature heating of steel reinforcement and a reduction in fire resistance. Spalling of NSC columns was not observed. It was concluded that material characteristics had a greater impact on failure modes than structural detailing.

Spalling behaviour of HPC columns was also observed by Ali et al. [46] who tested 18 HPC columns (90–110 MPa) under two parametric fire curves (low heating rate and BS476). The columns were subjected to three levels of axial loading which equal 0.2, 0.4 and 0.6 of the design strength. Among the 18 columns, 17 suffered various degrees of spalling (i.e. minor, major and severe). It was concluded that with an increase of load level, fire endurance was decreased but the probability of spalling was not increased. A lower heating rate could minimise the risk of spalling.

Kodur and McGrath [47] conducted a test programme on six full-scale HPC columns to investigate the effects of cross-section dimensions (305 and 406 mm), aggregate type (siliceous and carbonate) and tie configuration (bending of ties at 135°, lapped with 90° bending at the ends ties, additional cross-ties). The columns were tested under concentric loading and the applied load ranged from 54% to 123% of full service load. Cracks at the corner led to spalling of chunks of concrete at the end of the test. It was concluded that with an increase in load level, fire resistance was reduced.

Ali et al. [48] conducted a comprehensive experimental study on 99 columns under fire conditions to explore the influence of concrete strength (43 and 106 MPa), heating rate (high and low), degree of axial restraint (0, 0.1 and 0.2) and loading level (0, 0.2, 0.4 and 0.6 of column design strength). Explosive spalling happened in all the tests, and NSC and HPC columns showed similar susceptibility to spalling. It was reported that an addition of 3 kg/m³ of polypropylene (PP) fibres could reduce the degree of spalling from 22% to less than 1%.

The effectiveness of PP fibres in mitigating spalling was also investigated by other researchers. Kodur et al. [49] tested five columns to study the effects of concrete strength (40–100 MPa), aggregate type (siliceous and carbonate) and fibre reinforcement (42 kg/m³ of steel and 0.9 kg/m³ of PP fibres). The columns were subjected to concentric loading under fixed–fixed boundary conditions. The test results showed that the addition of PP fibres in HPC columns could reduce spalling and improve fire resistance. The presence of steel fibres could enhance the ductility of HPC columns and increase fire resistance.

To further explore the effect of fibre reinforcement, Khaliq and Kodur [50] tested another five columns made of NSC and HPC with plain, PP (1 kg/m³), steel (42 kg/m³) and hybrid fibres under concentric loading. It was found that the hybrid fibre (PP and steel) reinforced HPC

column could completely prevent spalling and exhibit better fire performance compared to columns reinforced with only one type of fibres.

Benmarce and Guenfoud [51] studied the fire behavior of high-strength concrete (HSC) columns by testing twelve specimens, focusing on load ratio, restraint ratio (column stiffness relative to structural restraint stiffness), and heating rate. Results showed that fire resistance decreased with higher load ratios, leading to lower failure temperatures for steel and concrete, as less restraint force was needed to cause failure. Restricting axial expansion reduced internal forces, and higher loads required less additional force to induce failure. Axial deformation during fire exposure depended on load levels but was unaffected by heating rate. Columns under low heating rates had failure times nearly double those under high heating rates, given identical restraint and load conditions.

I.4.3 Numerical studies

A review of literature indicates that a fair number of analytical studies have been conducted on the fire behavior of RC columns. The main objective in many of these studies was to trace the response of columns under fire conditions and to demonstrate the inherent fire resistance of RC columns. Most of the studies concentrated on developing numerical models, which were generally based on finite element or finite difference methods. In majority of these studies, the focus was mainly on NSC columns. In cases where HPC was considered, spalling was not fully incorporated in the analysis.

• Franssen and Dotreppe [52] utilized data from their fire tests, as well as that in the literature, to develop simplified calculation methods. The first of the two methods developed is an empirical equation, which expresses the fire resistance of RC columns as a function of influencing parameters. This method has been incorporated into Eurocode EC2-1-2[53] and yields conservative predictions. The second model developed by the authors is more elaborate and is classified as a simplified calculation method in Eurocode (level II according to EC2-1-2). This method has been validated against data from four circular columns tested by authors. In this model, the ultimate load capacity of the heated RC column is expressed as a fraction of the plastic crushing load of the section. This formulation gives safe, though rather conservative, fire resistance values for design purposes. Again these methods are applicable for standard fire exposure only as they were derived based on standard fire tests and do not account for fire induced biaxial bending. Figure I. 19 shows a graphic presentation of the comparison of fire resistance obtained with this method and experimental results.

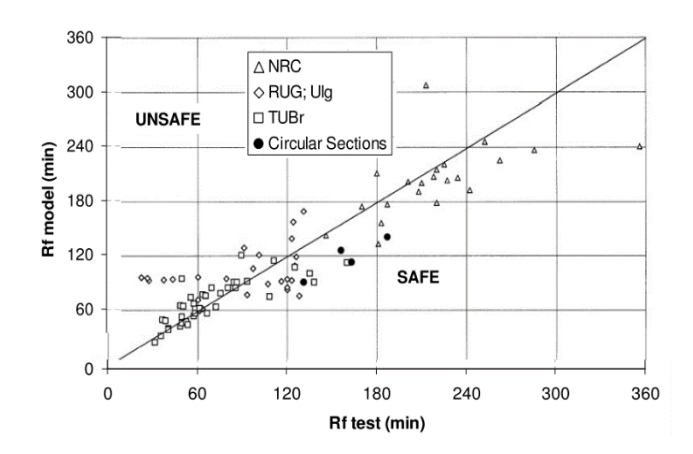


Figure I. 19 Comparison of fire resistance predictions from simplified equation and test data.

[52]

• Gernay and Dimia [54] developed a numerical model to predict the structural behavior of RC columns subjected to a natural (or realistic) fire, and attention was specifically given to the decay phase of fire exposure. A two-dimensional finite element analysis was performed on various cross sections. The main objective of the study was to get an insight to the parameters and conditions that could lead delay the collapse of a column after fire exposure. The parameters considered are the duration of the heating phase of the fire, effective length of the column, and the section size of the column. The main findings of the numerical study are that a failure during the cooling phase of a fire is possible in RC columns. Temperatures in the central portion of the modeled RC columns continue to increase even after the heating phase of a fire scenario has ceased. A failure during the cooling phase can also be ascribed to the additional strength loss of concrete that will occur during the cooling phase, when peak concrete temperatures are reached. The most critical situation for a delayed failure are a short fire exposure and for columns that have a low slenderness ratio (short length and/or massive cross sections).

I.4.5 Codes of practice

In most countries, fire-resistant design requirements are outlined in building codes and national standards, which typically follow a prescriptive approach. These codes and standards provide tabulated fire resistance values based on standard fire tests. These values are largely determined by factors such as concrete cover thickness and minimum cross-sectional dimensions of structural elements.

Eurocode 2, Part 1–2 [2004] [53] provides three methods for evaluating the fire resistance of reinforced concrete (RC) columns: simplified, tabular, and advanced methods. The tabular

method, the quickest and simplest, determines minimum dimensions and concrete cover thickness based on the nominal axis distance. The simplified equation method, derived from Franssen and Dotreppe [52], offers more economical designs for smaller columns or structures requiring longer fire resistance. Eurocode 2 outlines two simplified approaches: Method A and Method B. While both are valid, Method A is simpler but imposes stricter load eccentricity limits. For columns supporting the uppermost storey, load eccentricity often exceeds these limits, requiring analysis as beams. The code also mandates minimum reinforcement ratios and spacing criteria to ensure fire resistance.

Concrete structure design follows the ACI-318 [2008] [55] standard, which references ACI 216.1 [2007] [56] for fire resistance guidelines. ACI 216.1 specifies concrete cover thickness, minimum cross-sectional dimensions, and tie reinforcement spacing for reinforced concrete (RC) columns, with requirements varying based on aggregate type (siliceous or carbonate) and the number of sides exposed to ASTM E119 fire [57]. The latest edition includes provisions for high-strength concrete (HSC) columns, recommending 135° bent ties to enhance fire resistance ratings [58]. These measures improve fire performance and safety under elevated temperatures.

The Australian Standard AS 3600 [2001] [59] incorporates two distinct clauses for determining the fire resistance of reinforced concrete (RC) columns. The first clause applies to columns with all faces exposed to fire, while the second clause addresses columns that are partially exposed to fire. The standard provides a specific equation to calculate the fire resistance of RC columns, taking into account several critical parameters, including the steel reinforcement ratio, the compressive strength of the concrete, the cross-sectional dimensions of the column, the axial load acting on the column, and the effective length of the column. This equation offers a systematic approach to evaluating fire resistance, ensuring that structural safety and performance are maintained under fire conditions.

A detailed analysis of fire resistance specifications across various codes reveals significant variations in their provisions. The fire resistance of a typical reinforced concrete (RC) column tested by Lie and Woolerton [60] under ASTM E119 fire exposure, was computed using three distinct codes. The experimentally measured fire resistance was 183 minutes. Using ACI 216.1 provisions, the computed fire resistance was 180 minutes, closely aligning with experimental results. However, ACI 216.1 bases fire resistance ratings solely on concrete cover thickness and minimum cross-sectional dimensions, assigning the same rating to similar columns regardless of load level, slenderness, or reinforcement ratio. This highlights a limitation in the

prescriptive approach, as it does not account for these critical factors influencing fire performance.

The empirical equation provided in Eurocode predicts a fire resistance of 161 minutes for the analyzed RC column, while the simplified equation in the Australian code yields a significantly higher prediction of 234 minutes. This discrepancy underscores the considerable variation in fire resistance predictions derived from the provisions of current codes and standards.

I.5 Conclusion

This chapter synthesizes research on the effects of temperature on concrete degradation, emphasizing the intricate interplay of physical, chemical, and mechanical mechanisms. High temperatures induce physical changes such as heat transfer, free water evaporation, and conductivity variations, alongside chemical processes like dehydration, carbonation, and chemical transformations. Mechanical effects, including deformations and micro cracking, are exacerbated by incompatibilities at the paste-aggregate interface, leading to mass loss and property degradation. Residual mechanical properties post-high-temperature exposure exhibit significant variability, with Eurocode models providing foundational insights. However, the influence of heating and cooling regimes, particularly on steel, remains critical, as steel properties are often reversible. The presence of water in liquid and vapor forms further complicates thermal and mechanical behavior.

Research on reinforced concrete (RC) columns under thermal and mechanical actions reveals gaps, especially regarding cooling phases in natural fires and realistic fire scenarios. Most studies focus on nominal fire curves (e.g., ISO 834, ASTM E119) without considering cooling, and mechanical actions are often simplified. Additionally, post-fire seismic performance of RC columns is underexplored. Future research should prioritize advanced analytical models incorporating biaxial bending, multi-side fire exposure, spalling, creep, and realistic fire conditions. Reliable experimental data and parametric studies are essential to validate these models and develop design guidelines, including spalling mitigation for high-strength concrete. This will enable a performance-based fire safety design approach, ensuring cost-effective solutions for evaluating residual load-bearing capacity and seismic performance post-fire.

Chapter II:

Characterization of materials and formulation of high-performance concretes

II.1 Introduction

In this second chapter, we explore the physical and chemical characteristics of the materials used in the production of high-performance concrete (HPC). These materials include gravel, natural and crushed sand, cement, as well as silica fume. Each component plays a crucial role in the final properties of the concrete, and their selection and proportion in the mix are key to achieving the desired performance.

We will also present the formulation method for high-performance concrete. This method relies on a systematic and precise approach that considers the interactions between the various components, aiming to optimize both the workability of the concrete in its fresh state and its mechanical properties and durability when hardened.

Furthermore, we will examine the results related to the influence of silica fume and the integration of polypropylene fibers and date palm fibers on the characteristics of HPC in its fresh state. Silica fume can significantly alter the properties of the initial mix and hardened concrete, while polypropylene fibers and date palm fibers are considered to enhance impact resistance and prevent early cracking.

This chapter will highlight how these variables influence the performance of the concrete and will provide guidelines for designing HPC mixes suited to various construction applications and requirements.

II.2. Material characterization

II.2.1. Cement

For the experimental works, we utilized Portland composite cement classified as CEM II/A 42.5. This cement incorporates granulated blast furnace slag and 5% gypsum, produced in accordance with stringent quality standards. Specifically, it is manufactured by the Hdjar-Soud cement plant, conforming to both European standard EN 197-1 [1] and Algerian standard NA 442 [2], ensuring its suitability for high-performance applications.

The various chemical, physical, and mechanical characteristics of the cement used are established in the laboratories of the plant and the civil engineering department. The different results obtained are presented in Tables II.1 and II.2 respectively.

Table II. 1: Chemical composition of cement

Constituent	Percentage (%)
CaO (calcium oxide)	60.8
SiO ₂ (silicon dioxide)	23.45
Al ₂ O ₃ (aluminum oxide)	4.86
Fe ₂ O ₃ (iron oxide)	3.2
SO ₃ (sulfur trioxide)	2.2
MgO (magnesium oxide)	1
Na ₂ O (sodium oxide)	0.1
K ₂ O (potassium oxide)	0.45
Cl (chloride)	0.05
CaOl	0.9

Table II. 2: Physical and mechanical characteristics of cement

Property	Value	Units
Bulk density	1.06	g/cm ³
Absolute density	3.10	g/cm ³
Blaine fineness	3480	cm ² /g
Normal consistency	29	%
Initial Setting Time	154	minutes
Tensile strength	7	MPa
Compressive strength	42.5	MPa

II.2.2. Mineral additions

Mineral addition plays a significant role in the formulation of high-performance concrete. It enhances key properties of the concrete while contributing to its overall performance. This subsection focuses on the selected mineral addition, its chemical composition, and its impact on the physical and mechanical properties of high-performance concrete.

II.2.2.1. Silica fume

Silica fume is a mineral additive used in hydraulic concrete in accordance with the standard NF EN 13263-1 [3]. It is a pozzolanic material that plays a critical role in the development of mechanical strength and the enhancement of concrete durability. The silica fume commercially available from the Algerian company "CARACLA". It is supplied as a fine white powder (Figure II.1).

The chemical composition and physical properties of the silica fume are presented in Tables II.3 and II.4, respectively.

Table II.3: Chemical composition of silica fume

Oxide	Percentage (%)
SiO ₂ (silicon dioxide)	97.54
Al ₂ O ₃ (aluminum oxide)	0.10
Fe ₂ O ₃ (iron oxide)	0.21
CaO (calcium oxide)	0.02
MgO (magnesium oxide)	0.01
Na ₂ O (sodium oxide)	0.04
K ₂ O (potassium oxide)	0.15

Table II.4: Physical properties of silica fume

Physical property	Value	Units
Particle size	0 - 0.08	mm
Specific surface Area	5000	cm ² /g
Bulk density	1.51	g/cm ³
Absolute density	2.64	g/cm ³
Sand equivalent	87.00	%
Sand absorption SAb	3.87	%
Sand friability SF	18.05	%



Tridymite Cristobalite 2 θ (Ka, Co) °C

Figure II.1:Silica fume

Figure II.2: Diffractogram of silica fume

The X-ray diffraction analysis of the silica fume, as depicted in Figure II.2, reveals that the material is primarily vitreous, containing small quantities of crystallized minerals in the form of tridymite and cristobalite.

II.2.3. Aggregates

The aggregates used are local products, in accordance with current Algerian standards (or their equivalents): NA 2607-1 (NF P18-560), NA 2608, NA 455 (NF P18-598), NA 5130, NA 463 (NF P18-554), NA 5089, NA 255 (NF P18-555), and NA 5125 (NF P 18-561). These materials are rough and clean crushed limestone. The aggregates are stored in bins and kept in the laboratory for air drying several weeks before use. The granular classes used for concrete manufacture are: (0/2) for dune sand, (0/4) for quarry sand, and (5/12) for gravels. Figure II.3.



Figure II.3: Different aggregates used in the test

II.2.3.1 Sand

In our study, we utilized two types of sand: Quarry sand 0/4 (from the Annaba region) and Dune sand 0/2 (from the Tébessa region). The main physical properties of both sands are presented in Table II.5, and the tests conducted are illustrated in Figure II.4.

Table II.5: main physica	1 properties of	quarry sand (Annaha)	and dune sand (T	'ébessa)
Table 11.5. Illam blivsica	i biobeides oi (duali v Saliu (Alillaba)	and dunc sand ()	CUCSSAI

Property	Quarry sand 0/4 (Annaba)	Dune sand 0/2 (Tébessa)	Units
Particle size	0 - 4	0 - 2	mm
Bulk density	1.46	1.51	g/cm³
Absolute density	2.60	2.62	g/cm³
Fineness modulus	2.98	2.28	-
Intergranular porosity	45.25	45.85	%

II.2.3.2 Gravel

The gravel used in this study is limestone gravel sourced from the Annaba region. It is characterized by a particle size ranging from 5 to 12.5 mm. The properties of this gravel are compiled in Table II.6.

Table II. 6: Properties of limestone gravel (Annaba)

Property	Value	Units
Particle size	5 - 12.5	mm
Bulk density	1.45	g/cm³
Absolute density	2.69	g/cm³
Intergranular porosity	49.23	%
Los-angles test	24.50	%



Figure II.4: Different aggregate used in the test

Granulometric analysis

The granulometric analysis test is conducted in accordance with standards [4], [5]. This test is used to determine the cumulative mass proportions that pass-through sieves of various mesh diameters from a sample of sand or gravel. The percentages of cumulative pass-through are represented in the form of granulometric curves, as shown in Figure II.5.

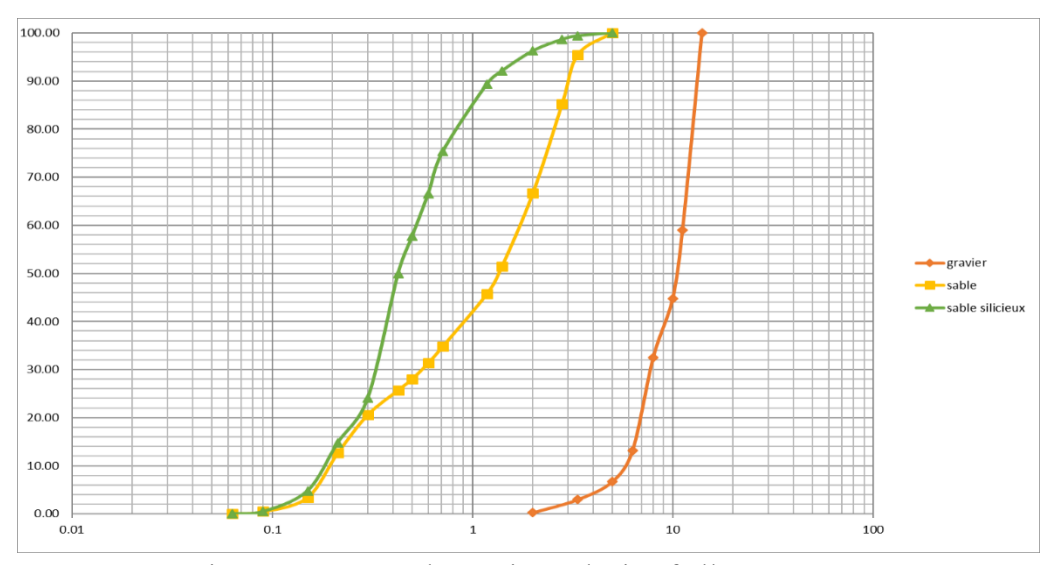


Figure II.5: Granulometric analysis of all aggregates

The granulometric analysis results indicate that the three granular fractions utilized in this study form a continuous granular skeleton, achieving optimal compactness. This suggests a well-graded particle size distribution that enhances density and structural stability.

II.2.4. Fibers

Using fibrers in high-performance concrete (HPC) involves incorporating small, discrete fibers into the concrete mix to improve various physical properties and performance characteristics. This modification aims to address the inherent brittleness and limited crack resistance of traditional concrete.

In this study we use two type of fibre polypropylene fibers and the date palm fibers.

II.2.4.1 Polypropylene fibers

The fibers used are polypropylene fibers (figure II.6) marketed by the Algerian company Sika El-Djazair. They are used in high-performance concrete to improve the fire resistance of these structures. Their technical characteristics are given by the manufacturer.

Table II. 7: Polypropylene fibers characteristics



Property	Value	Units
Fiber length	12	mm
Density	0.9	-
Melting point	150	°C
Young's modulus	3	KN/mm ²
Fiber cross- section	30	microns

Figure II.6: Polypropylene fibers

Thermogravimetric analysis of polypropylene fibers (TGA) was performed using a Netzsch STA 499 F3 device coupled with Netzsch Proteus Software for data analysis and deconvolution of the derivative curve. The TGA and DTG curves are presented in Figure II.7.

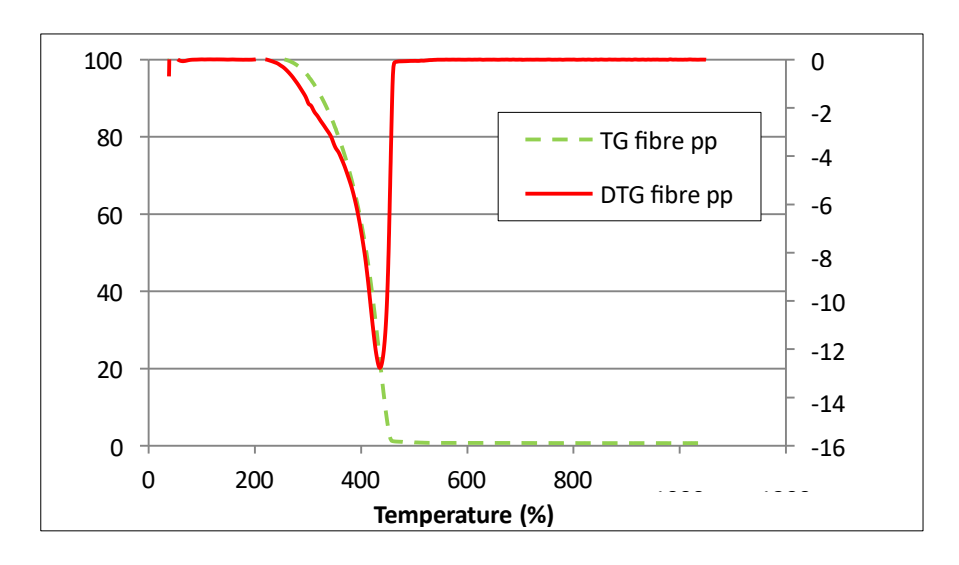


Figure II.7: ATG curve for polypropylene fibers

According to the above Figure II.7, a peak can be observed around the temperature of 460 °C, corresponding to the mass loss of the material, which is due to the combustion of polypropylene fibers [6].

II.2.4.2 Date palm fibers

The use of date palm fibers in concrete represents a promising direction in sustainable construction. These fibers, extracted from the trunks and leaves of date palm trees, as depicted in Figure II. 8 Drawing from the research conducted by Kriker et al. [7], which examined four types of fibers harvested from the exteriors of the date palm varieties dokar, deglette-nour, degla-bida, and elguers (using their local nomenclatures), dokar fibers were identified to possess superior tensile strength. Consequently, dokar fibers were selected for inclusion in our study. The physical and mechanical properties of dokar fibers are delineated in Table II.8. Within the HPCD mixtures, date palm fibers were incorporated at a rate of 1.85 kg/m³.



Figure II.8: Illustrations of palm fibers

Table II.8: Physical and mechanical properties of the palm fibers used [43].

Physical characteristics	Lower-Upper	Coefficient of variation CV (%)
Length (mm)	20-100	-
Diameter (mm)	0.1 - 1	0.45-54.43
Tensile Strength (MPa)	285 ± 15	-
Apparent density (kg/m ³)	512.20-1088.80	900-17.64
Absolute density (kg/m ³)	1300-1455	1383-5.52
Natural Water Content (%)	9.50-10.50	10-5.00
Ultimate strain (%)	11.00-16.00	-
Modulus of elasticity (GPa)	4.74-5.25	-
Water absorption (%)	96.84-202.65	-

II.2.5 Superplasticizer

The superplasticizer VISCOCRETE TEMPO 12, marketed by Sika El-Djazair in Algeria, is a high-performance concrete admixture conforming to NF EN 934-2 standards. This product is essential for enhancing the properties of both fresh and hardened concrete. It significantly reduces the water required without compromising workability, thereby facilitating the placement and processing of concrete under complex conditions. VISCOCRETE TEMPO 12 also increases the fluidity of the concrete, allowing for higher initial and final strengths, crucial for projects requiring high performance and enhanced durability.

The essential properties provided by the manufacturer are as follows:

Form: Liquid.

Color: Light brown.

pH: 6 ± 1 .

Density: 1.06 ± 0.01 .

Chloride Content: $\leq 0.1\%$.

II.2.6. Mixing water

The conditions imposed on mixing water are specified by the standard NF EN 1008 [94]. This water must be clean and free from organic materials. The water used in our study is potable tap water from the laboratory (city of Guelma).

II.3. Formulation of study concretes

In our research, we adopted the concrete formulation method developed by Aïtcin at the university of Sherbrooke [8], recognized for effectively integrating empirical outcomes with theoretical calculations. This method employs the absolute volume approach, which meticulously calculates the required volumes of each concrete component to achieve optimal performance characteristics.

A key aspect of this methodology is the comprehensive consideration of water sources, including the water content in superplasticizers as part of the total mixing water. This approach ensures precise control over the water-to-cement ratio, which is crucial for enhancing the concrete's mechanical properties and ensuring its durability.

The process is methodically outlined in a flowchart, illustrating the systematic steps from the selection of materials, through detailed volumetric calculations, to adjustments based on trial mixes. This procedure ensures that the formulated high-performance concrete meets stringent standards, maintains consistent quality across batches, and adapts effectively to diverse applications. The flowchart provided below details these steps, offering a clear guide to replicating and optimizing the mix design for High-Performance Concretes.

Figure II.9. Flowchart of the proposed method for formulating HPC (High Performance Concrete)

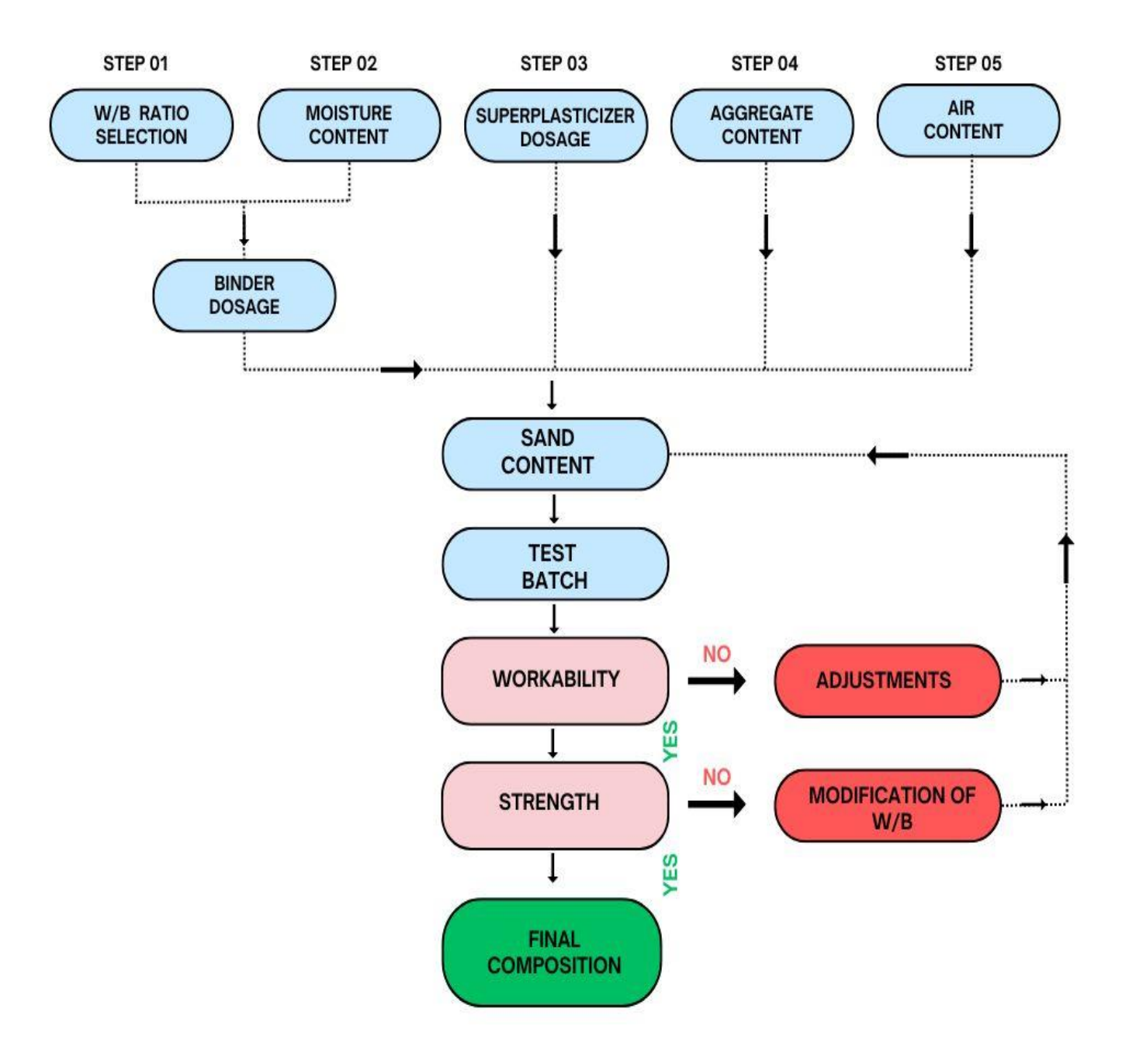


Figure II. 9: Flowchart of the proposed method for formulating HPC

Mix compositions for one cubic meter of concrete are shown in Table II.9.

Table II.9: Batches quantities in Kg/m³

MIX	HPC	HPCPP	HPCDP	HPCPPQS
W/B	0.275	0.275	0.275	0.275
Cement kg/m ³	489.20	489.20	489.20	489.20
Water kg/ m ³	150	150	150	150
Dune Sand kg/m ³	368.970	368.970	368.970	184.485
Quarry Sand kg/m ³	368.970	368.970	368.970	553.455
Gravel kg/ m ³	1070	1070	1070	1070
Superplasticizer kg/ m ³	7.338	7.338	7.338	7.338
Silica Fume kg/ m ³	48.920	48.920	48.920	48.920
PP Fiber kg/ m ³	-	1.85	-	1.85
DP fiber kg/ m ³			1.85	

Designation of concrete used:

HPC: High-performance concrete.

HPCPP: High-performance concrete with polypropylene fibers.

HPCDP: High-performance concrete with date palm fibers.

HPCPPQS: High-performance concrete with polypropylene fibers based on quarry sand.

II.4. Fabrication and curing of specimens

The mixing of the concrete was performed using a concrete mixer with a capacity of 30 liters, adhering to the normative references [9] and [10]. The total mixing duration was set at 5 minutes. The mixing sequences were as follows:

- 1 minute of dry mixing: Introduction of gravel, sand, cement, and fillers. In the case of fiber-reinforced concretes, polypropylene fibers were added and dispersed manually to ensure even distribution throughout the mix.
- 2 minutes of mixing: Introduction of 75% of the mixing water.
- 2 minutes of mixing with the remaining 25% of water, in which the superplasticizer was dissolved.

Vibration was performed on a vibrating table with adjustable vibration amplitude. The vibration duration was 30 + 30 seconds. The specimens were demolded after 24 hours and

stored in a saturated humidity environment (a temperature close to 20 °C and a humidity level nearly equal to 100%) until the day of testing.

The specimens were aged 7, 28, and 1 year at the time of testing. The experimental study was conducted on different shapes of specimens, which are grouped in Table II.10. This structured approach ensures that each concrete specimen is consistently prepared and cured, providing reliable data for performance assessment across various ages and condition.

Table II.10: Types and shapes of specimens with conducted tests.

Shapes of specimens	Conducted tests
Cube (10X10X10) cm	Mass loss Mechanical strength in compression
Cube (15X15X15) cm	Mechanical strength in tension Dynamic modulus of elasticity (non-destructive testing)

II.5. Thermal treatment cycle of concretes

Fire resistance tests were conducted on four samples under a severe fire scenario, where the specimens were exposed to fire on all sides. The temperature was systematically increased from an initial ambient temperature of 20 °C to three distinct target levels: 250 °C, 450 °C, and 650 °C. The heating phase lasted 60 minutes, with an average heating rate of 8 °C per minute. Once the maximum temperatures were reached, they were maintained for one hour to simulate sustained fire exposure. Subsequently, the samples were cooled under conditions designed to replicate typical post-fire scenarios in building environments. The results of each test represent the average performance of three cubic concrete specimens. Figure II.8 illustrates the heating and cooling curve of the furnace, while Figure II.9 provides a visual representation of the furnace utilized during the experimental process.

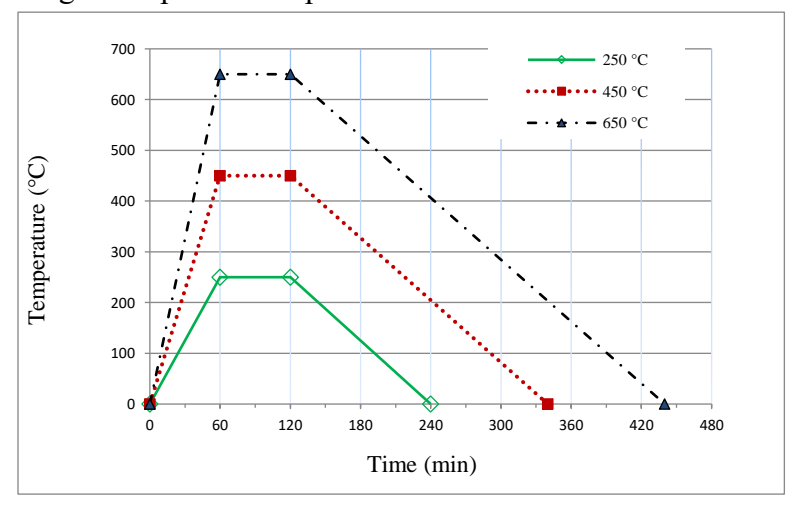


Figure II.10: Curves of heating and cooling according to temperature





Figure II.11: Naberthen furnace (University of Ouargla)

II.6. Procedures for determining the properties of fresh concrete

The characterization of fresh concrete is achieved by measuring its workability, characterized by the slump using the Abrams cone, density, and entrapped air.

II.6.1. Workability

The slump test with the Abrams cone is the most commonly used test to measure the workability of concrete. This test is conducted according to the standard NF EN 12350-2 [11]. It determines the consistency of fresh concrete by measuring the slump, which is the difference between the height of the conical mold used and the highest point of the collapsed test sample. The cone used has dimensions (D=20 cm, d=10 cm, and h=30 cm). The cone should be placed on a slightly moistened horizontal metallic plate as shown in Figure II.12. The cone is filled in three equal layers, each compacted with 25 strokes using a standardized rod. Once filled, the mold should be removed vertically. The slump h is measured after the slump has stabilized using a ruler.



Figure II.12: Abrams cone slump test (University of GUELMA).

II.6.2 Density

The actual density of fresh concrete was measured according to the standard NF EN 12350-6 [12]. This measurement involves weighing an empty container and then filled with vibrated concrete. The difference in these two weights divided by the volume of the container gives the density, as indicated in the following expression:

$$Mv = \frac{Mf - Me}{Vr}$$
 (g/cm3)

Where:

Mv: density of concrete in g/cm3

Mfilled: mass of the container filled with concrete in g

Mempty: mass of container in g

Vrecipient: volume of the container in cm3

II.6.3 Entrained Air

The compressibility method is utilized to measure the entrained air in fresh concrete. As air is the only compressible element in fresh concrete, compressing it results in a reduction in pressure applied to the concrete. This reduction is directly proportional to the amount of entrained air. The test adheres to French Standard EN 12350-7 [13], and is conducted using an 8-liter capacity concrete air meter, illustrated in Figure II.13.

The lower chamber of the air meter is filled with concrete, and the upper chamber is securely sealed with an airtight mechanism. An air pump located at the top of the cover applies pressure, causing the water level to drop proportionally to the reduction of air voids. The air meter is calibrated to indicate the total air content as a percentage, allowing for a direct reading of the water level on the graduated scale.



Figure II.13:Concrete air meter (University of GUELMA).

II.7. Results and interpretations of the properties of fresh concrete

II.7.1. Workability

The values measured for the slump using the Abrams cone are displayed in Figure II.14.

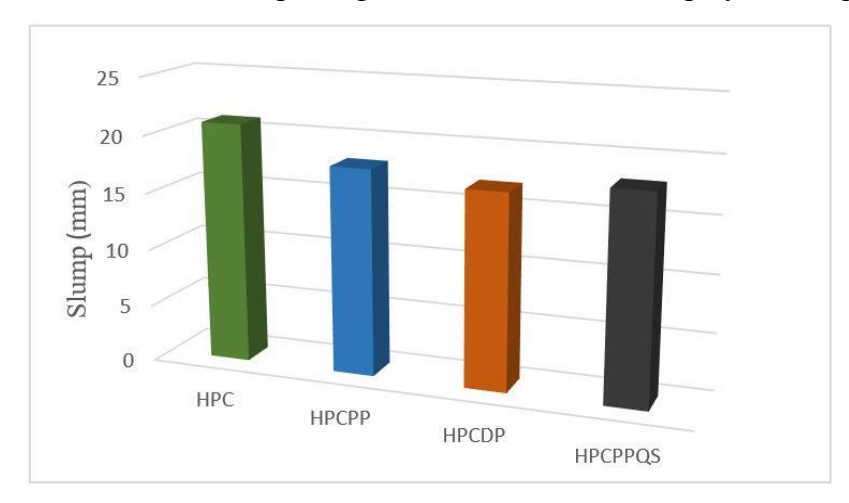


Figure II.14: Variation in the slump for different types of concrete.

The slump test results highlight distinct workability characteristics among the high-performance concrete (HPC) mixes. The reference mix (HPC) achieved the highest slump value of 21, reflecting optimal workability due to the absence of fibers or additional reinforcements that could impede flow. In contrast, the mix with polypropylene fibers (HPCPP) exhibited a slump of 18, indicating reduced workability. This decline is attributed to the polypropylene fibers, which enhance resistance to deformation and limit flow while reinforcing the matrix and mitigating shrinkage cracking.

The mix incorporating date palm fibers (HPCDP) recorded the lowest slump value of 17, demonstrating the most significant reduction in workability. This is due to the natural fibrous texture of date palm fibers, which increase viscosity and restrict mobility owing to their surface roughness and structural properties. The mix combining polypropylene fibers and quarry sand (HPCPPQS) achieved a slump of 18, comparable to HPCPP. The inclusion of quarry sand appears to counterbalance the restrictive effect of the fibers, maintaining acceptable workability while providing structural stability.

In summary, the addition of fibers generally reduces workability, with polypropylene fibers causing a moderate decrease and date palm fibers having a more pronounced impact. The combination of fibers with quarry sand (HPCPPQS) preserves adequate workability while leveraging the reinforcing benefits of the fibers. These findings emphasize the importance of

selecting appropriate fiber types and aggregates to achieve targeted workability and performance characteristics for specific applications

II.7.2 Density

The results of the variation in the density of different HPC in the fresh state are illustrated in Figure II.15.

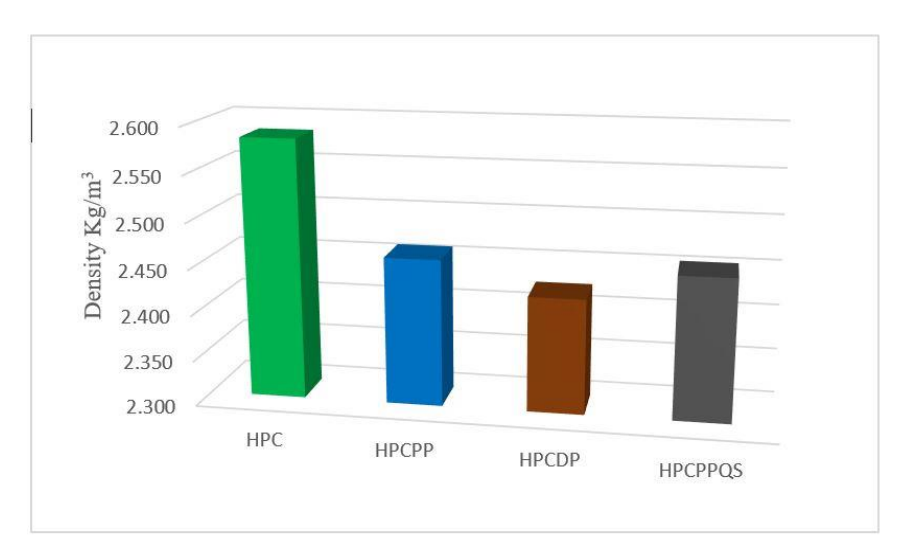


Figure II.15: Density variation among different types of concrete.

The bar graph illustrates the density variations across four high-performance concrete (HPC) formulations: the reference mix (HPC), HPC with polypropylene fibers (HPCPP), HPC with date palm fibers (HPCDP), and HPC with polypropylene fibers and quarry sand (HPCPPQS). The reference mix (HPC) achieves the highest density at 2583.80 kg/m³, indicative of its densely packed matrix. The mix with polypropylene fibers (HPCPP) exhibits a lower density of 2460.9 kg/m³, attributable to the lightweight nature of the fibers, which enhance crack resistance and toughness through stress distribution.

The mix incorporating date palm fibers (HPCDP) records the lowest density at 2425.8 kg/m³, resulting from the low-density fibers that improve energy absorption and flexibility. The mix combining polypropylene fibers and quarry sand (HPCPPQS) achieves a density of 2455.9 kg/m³, where the quarry sand enhances compactness due to its uniform grain size, partially offsetting the density reduction caused by the fibers.

In summary, the inclusion of fibers reduces density, while quarry sand contributes to a denser matrix. Each formulation offers distinct mechanical properties, making them suitable for specific structural applications.

II.7.3. Air Entrapment

The measurements of the entrapped air quantity in different HPCs are presented in Figure II.16.

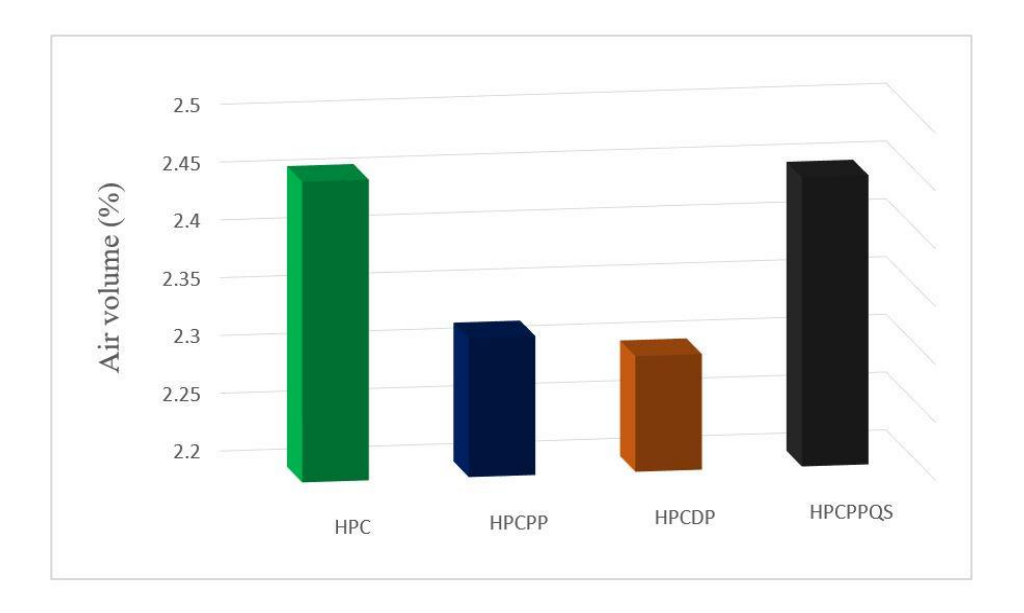


Figure II.16: Air entrapment

The bar graph illustrates the performance variations among four high-performance concrete (HPC) formulations: the reference mix (HPC), HPC with polypropylene fibers (HPCPP), HPC with date palm fibers (HPCDP), and HPC with polypropylene fibers and quarry sand (HPCPPQS).

The reference mix (HPC) achieves the highest performance value of 2.46, reflecting its dense and tightly packed matrix. The mix with polypropylene fibers (HPCPP) shows a slightly lower performance of 2.32, as the lightweight fibers reduce density and compressive strength marginally while enhancing toughness, crack resistance, and impact strength.

The mix incorporating date palm fibers (HPCDP) exhibits a performance value of 2.30. The natural fibers reduce density but improve ductility and energy absorption, offering a sustainable alternative to synthetic fibers. The mix with quarry sand (HPCPPQS) achieves a performance of 2.45, nearly matching the reference mix. The uniform grain size and angular shape of quarry sand enhance compactness and workability without significantly compromising performance. In summary, the addition of fibers improves toughness and crack resistance at the expense of a slight reduction in compressive strength, while quarry sand provides a viable alternative to natural sand, maintaining comparable performance. Each formulation offers distinct mechanical properties, making them suitable for specific structural applications based on the desired balance of strength, durability, and sustainability.

II.8. Conclusion

This chapter examines the characteristics of materials used in high-performance concrete (HPC) production and their impact on mix performance. Key materials include cement, mineral additives, sand, gravel, and reinforcing fibers such as polypropylene and date palm fibers. Each material influences HPC's workability, strength, and durability. Fibers, in particular, enhance crack resistance and energy absorption, while quarry sand maintains compactness and structural stability.

Slump test results indicate that fiber additives generally reduce workability, with polypropylene fibers moderately decreasing flow and date palm fibers significantly increasing viscosity. Quarry sand effectively balances these effects, ensuring adequate workability and performance.

In summary, the chapter highlights the importance of material selection and understanding their interactions to optimize HPC performance. The next chapter will focus on characterizing the influence of mineral additives and polypropylene fibers on the physical and mechanical properties of HPC under high-temperature condition

Chapter III:

Physical and mechanical behavior of highperformance concrete under temperature effects

III.1 Introduction

This chapter presents detailed experimental protocols and analyzes residual results related to the mass loss, compressive strength, tensile strength, and modulus of elasticity of high-performance concrete at various temperatures (20°C, 250°C, 450°C, and 650°C) across different maturity stages (14, 28, and 365 days). Each test aims to quantify the thermal durability and mechanical integrity of the concrete under sustained high temperatures. The methodology includes controlled thermal cycling and mechanical testing to simulate environmental and operational conditions. This comprehensive analysis helps delineate the critical thresholds beyond which the physical and mechanical properties of the concrete begin to deteriorate significantly. The results are discussed in the context of enhancing the design and formulation of concrete mixes for improved performance in high-temperature environments. This chapter contributes to a better understanding of how temperature influences the evolution of the physical and mechanical properties of concrete, providing essential insights for engineers and designers in the construction industry.

III.2. Physical properties

III.2.1. Residual mass loss

To determine the evolution of mass loss as a function of the heating-cooling cycle, specimens are weighed before and after each cycle of heating and cooling [1, 2]. Specimens are weighed immediately after heating to prevent any rehydration with the ambient environment.

The test aims to determine the material loss that the specimens undergo during heating compared to their initial state (state before heating). The mass loss, expressed as a percentage, is calculated as follows:

Percentage of Mass Loss (%)=
$$\frac{Mi-Mt}{Mi}$$
 x 100 (III.1)

Where:

Mi: is the initial mass of the specimen before the heating-cooling cycle.

Mt: is the mass of the specimen after the cycle, once it has cooled down.

The specimens utilized are cubic in shape with dimensions of $10 \times 10 \times 10$ cm³. They are weighed using an electronic scale with a precision of 0.1 g, as shown in Figure III.1. This high level of accuracy ensures reliable data collection critical for analyzing the effects of thermal cycles on concrete's mass stability. The figure illustrates the setup of the weighing process, emphasizing the meticulous approach taken in experimental measurements to minimize errors and ensure repeatability of results.

This approach allows for an accurate assessment of the durability and thermal stability of the concrete under simulated environmental conditions, providing crucial data for understanding the structural integrity of the material after thermal exposure.



Figure III.1:Measurement of mass loss (LGCH, University of GUELMA)

III.3 Mechanical properties

III.3.1. Residual compressive strength

The compressive strength test was conducted on cubic specimens with dimensions of $10\times10\times10$ cm³, in accordance with the European standard NF EN 12390-3 [3]. The specimens tested include those kept at ambient temperature and those cooled down after the heating cycle. The specimens are stored in water until the test deadlines of 7, 28, days. For each concrete type and each heating cycle, the compressive strength recorded is the average from three specimens. The crushing of the specimens was carried out using a hydraulic press with a maximum capacity of 2000 kN and a loading speed of 2.4 ± 0.2 kN/sec, as illustrated in Figure III.2. the maximum load recorded during the test. The compressive strength at "j" days (fcj) is calculated as the ratio of the breaking load to the cross-sectional area of the specimen (Equation III.2):

$$f_{cj} = \frac{P_{max}}{A} \times 100$$
 (III.2)

Where:

 f_{cj} : represents the compressive strength at 'j' days, typically measured in megapascals (MPa).

 P_{max} : is the maximum load sustained by the specimen during the test, measured in newtons (N).

A: is the cross-sectional area of the specimen, calculated as the side length squared for cubic specimens, typically measured in square millimeters (mm²).



Figure III.2: Compression test (LGCH, University of Guelma).

III.3.2. Residual tensile strength.

The residual tensile strength test was conducted on cubic specimens with dimensions of $15\times15\times15$ cm³, in accordance with the relevant standard (EN 12390-6). The specimens tested include those kept at ambient temperature and those subjected to specific exposure conditions, such as high-temperature heating cycles or chemical exposure. After exposure, the specimens were stored in water until the test deadlines of 7, 28. For each concrete type and each exposure condition, the residual tensile strength recorded is the average value obtained from three specimens.

The splitting tensile strength test (Brazilian test) was performed using a hydraulic press with a maximum capacity of 2000 kN and a loading speed of 2.4 ± 0.2 kN/sec, as illustrated in Figure III.3. The specimens were placed horizontally between the loading platens, and a compressive load was applied along the vertical diameter until failure occurred by splitting.

The maximum load recorded during the test was used to calculate the residual tensile strength. The splitting tensile strength at "j" days (fct,j) is calculated as the ratio of the breaking load to the cross-sectional area of the specimen, using the following formula (EquationIII.2):

$$f_{ct,j} = \frac{2P}{\pi \cdot d^2} \qquad \text{(III.3)}$$

Where:

- P is the maximum load applied (in Newtons),
- d is the side length of the cube (in meters).



Figure III.3: Tensile strength test

III.3.3. Dynamic deformation modulus (non-destructive testing)

The stress-strain relationship in concrete is complex, primarily due to the unique behavior of the gel structure and how water is retained in hardened concrete. The static modulus of elasticity, determined through actual loading of concrete, may not accurately reflect its true elastic behavior. The phenomenon of creep significantly impacts the elastic modulus, especially at higher stress levels where creep effects are more pronounced. Efforts have been made to estimate the modulus of elasticity using non-destructive testing methods. One effective method to determine this modulus involves subjecting the concrete to longitudinal vibrations at its natural frequency. This process can either involve measuring the resonant frequency of a concrete specimen or assessing the pulse velocity that travels through the concrete. Using these parameters, the modulus of elasticity can be calculated based on the established relationship.

$$E_d = kn^2L^2P \quad \text{(III.4)}$$

Where:

E_d: is the dynamic modulus of elasticity

K: is constant N- is resonant frequency

L:is length of specimen

P: is the density of concrete.

The ultrasonic pulse velocity (UPV) method involves measuring the travel time of an ultrasonic pulse through concrete Figure III.4. This method uses a pulse generator circuit that includes an electronic circuit to generate pulses and a transducer to convert these electronic pulses into mechanical energy, which vibrates at frequencies ranging from 15 to 50 kHz. The travel time of the pulse is measured electronically from its initial onset to reception. The average velocity of wave propagation is then calculated by dividing the path length between transducers by the travel time. The propagation speed or celerity is then given by the equation:

$$V = \frac{d}{t}$$
 (III.5)

Where:

V: is the speed of the waves,

d: is the distance between the transmitter and receiver,

t: is the measured propagation time.

For determining the dynamic modulus of elasticity using UPV, the velocity of ultrasonic waves is measured. From this measurement, the dynamic modulus of elasticity, E, can be calculated as follows:

$$E = \rho . V^2 \frac{(1-v)}{(1+v)(1-2v)}$$
 (III.6)

where ρ is the density of the concrete, and ν is the Poisson's ratio of the concrete.

For a Poisson's ratio ranging between 0.2 and 0.3, it can be accepted that the ratio $\frac{(1-v)}{(1+v)(1-2v)}$ is equal to 1, thus defining the increased dynamic modulus:

$$E = \rho V^2$$
 (III.7)

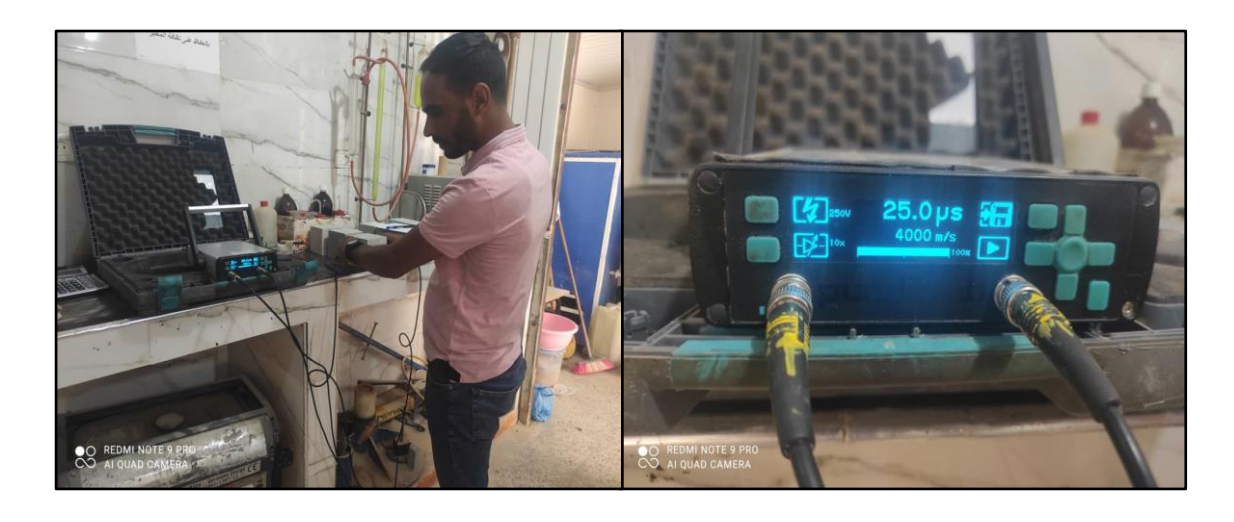


Figure III.4: Measurement of sound speed (NIZOLP ElOUED).

III .4 Results and analysis

Different concretes' fire performance is evaluated by comparing their residual compressive strength, residual flexural strength, ultrasonic pulse propagation velocity (UPV), mass loss, and spalling progression.

III .4.1 Residual compressive strength

According to literature reviews [4,5,6], the properties of concrete subjected to high temperatures are influenced by various factors, including initial strength, composition of materials, age of the concrete, moisture content, among others. It is widely acknowledged that both standard-strength and high-performance concrete exhibit a marked reduction in compressive strength when exposed to rapid temperature increases, typical of fire conditions [7]. This study involved analyzing and comparing samples from different concrete formulations, as illustrated in Figure III.5.

The findings related to the residual compressive strength at ambient temperature (20 ± 2) °C and following exposure to temperatures of 250, 450, and 650 °C are documented in Table III.1, with each entry representing the mean of three specimens. clearly demonstrates a decline in the compressive strength of concrete as the temperature rises. The average residual compressive strengths, in comparison to those at room temperature, were observed to be between 88% to 95% at 250°C, 69% to 82% at 450°C, and 35% to 52% at 650°C.

The study's analysis up to 650 °C, showcased in Figure III.5, reveals a consistent decrease in compressive strength with escalating temperatures, underscoring the significant impact of thermal exposure on this property. The reduction in compressive strength relative to room temperature was approximately 5% to 12% at 250°C, 18% to 31% at 450°C, and 48% to 65% at 650°C, as determined in this investigation.

The comparative analysis indicates that the mechanical performance of high-performance concrete (HPC) and high-performance concrete with polypropylene fibers (HPCPP) under high temperatures significantly surpasses that of high-performance concrete with date palm fibers (HPCDP) and high-performance concrete with quarry sand (HPCPPQS) within the studied temperature spectrum.

This research emphasizes the beneficial effect of integrating palm fibers as an alternative to polypropylene in enhancing the fire resistance of high-performance concrete (HPC). Notably, Figure III.5 reveals that after three hours of exposure to elevated temperatures, a 65% reduction in concrete strength was recorded, mirroring the loss observed with polypropylene fibers. These encouraging outcomes underscore the potential of palm fibers as an effective replacement for polypropylene in improving the fire resilience of HPC.

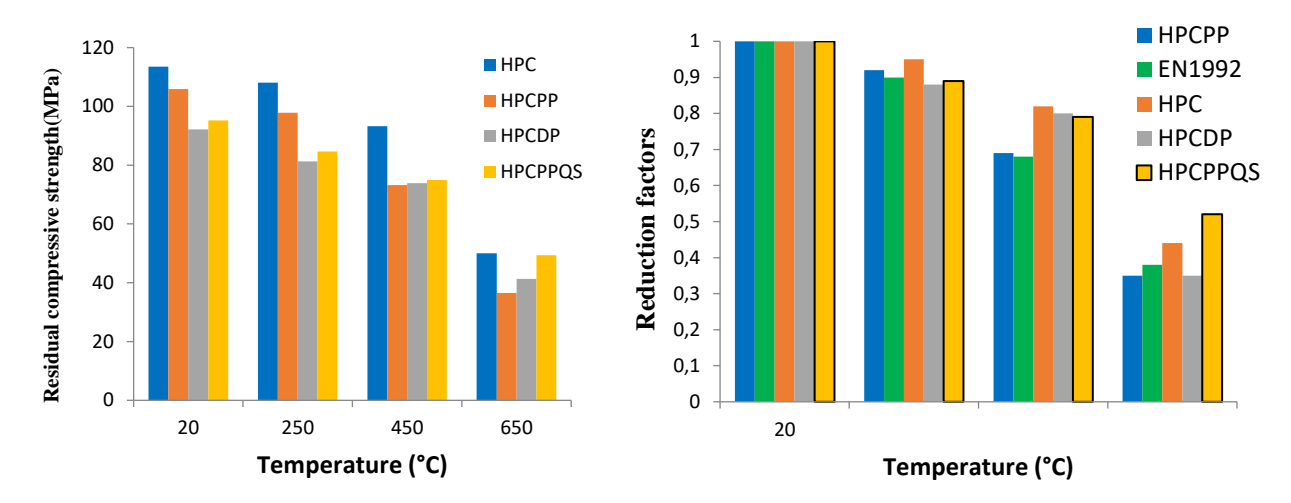


Figure III.5: Residual compressive strength (a) and reduction factors (b) as a function of temperature.

Table III. 1 Reduction in residual compressive strength as a function of temperature

Compressive Strength (MPa)				
Temperature	Room temp.	250 °C	450 °C	650 °C
HPC	113.50	108.10	93.31	50.06
НРСРР	105.92	97.81	73.21	36.56
HPCDP	92.12	81.26	73.91	41.30
HPCPPQS	95.17	84.70	75.01	49.40

To examine the results of this study, the strength reduction factor recommended by EC-2 [8], which depends on the exposure temperature, was used according to the following formula:

$$R_{ck} = \frac{f_{c(\theta)}}{f_{ck(20^{\circ}C)}}$$
 (III.7)

Where:

 R_{ck} : is the strength reduction factor,

 $f_{ck(20^{\circ}C)}$: is the compressive strength at room temperature,

 $f_{c(\theta)}$: is the compressive strength at elevated temperature.

This equation has been validated as a suitable method to evaluate the decrease in the strength of concrete exposed to elevated temperatures. The strength reduction factors, obtained from equation (1), are summarized in Table III.2. It is notable that the strength reduction factor of palm

fiber concrete presents an accepted value and is very close to other types of concrete such as HPC, HPCPP, and HPCDP.

The compressive strength reduction factor determined in this study can be compared with those suggested by EC-2 [8], which recommends the reduction factor for normal weight concrete with silica aggregates. However, all samples exhibit values slightly higher than those recommended by the Eurocodes standards, especially within the temperature range of 250 to 450 degrees (Figure III.5).

Table III.2:Reduction factors of compressive strength.

Reduction factor of compressive strength (R_{ck})								
Temperature °C	EN1992 (REF) HPC	HPC	НРСРР	HPCDP	HPCPPQS			
Room temp.	1.00	1.00	1.00	1.00	1.00			
250 °C	0.90	0.95	0.92	0.88	0.89			
450 °C	0.68	0.82	0.69	0.80	0.79			
650 °C	0.38	0.44	0.35	0.35	0.52			

III .4.2 Modulus of elasticity in compression

The modulus of elasticity of concrete is consistently related to its initial compressive strength. However, as shown in Figure III.6 below, the series of curves for all types of concrete studied show performance superior to those recommended by EC-2 [7], with differences varying between 12% and 24% over a temperature range of 200 ° C to 650 ° C. The largest differences occur at a temperature of 450 ° C. Additionally, palm fiber concrete HPCDP and polypropylene concrete HPCPP showed significant degradation beyond 450 ° C compared to other types of concrete. This seems logical because fibers generally have a negative effect on the elastic modulus; this has been demonstrated by research conducted by Hager and Pimienta [9]. The elastic modulus reduction factors are summarized in Table III. 3.

Table III.3: Elastic modulus reduction factor

Temperature °C	EN1992 (Ref)HPC	HPC	HPCPP	HPCDP	HPCPPQS
20	1	1	1	1	1
250	0.9	0.95	0.92	0.88	0.89
450	0.68	0.82	0.69	0.8	0.79
650	0.38	0.44	0.35	0.35	0.52

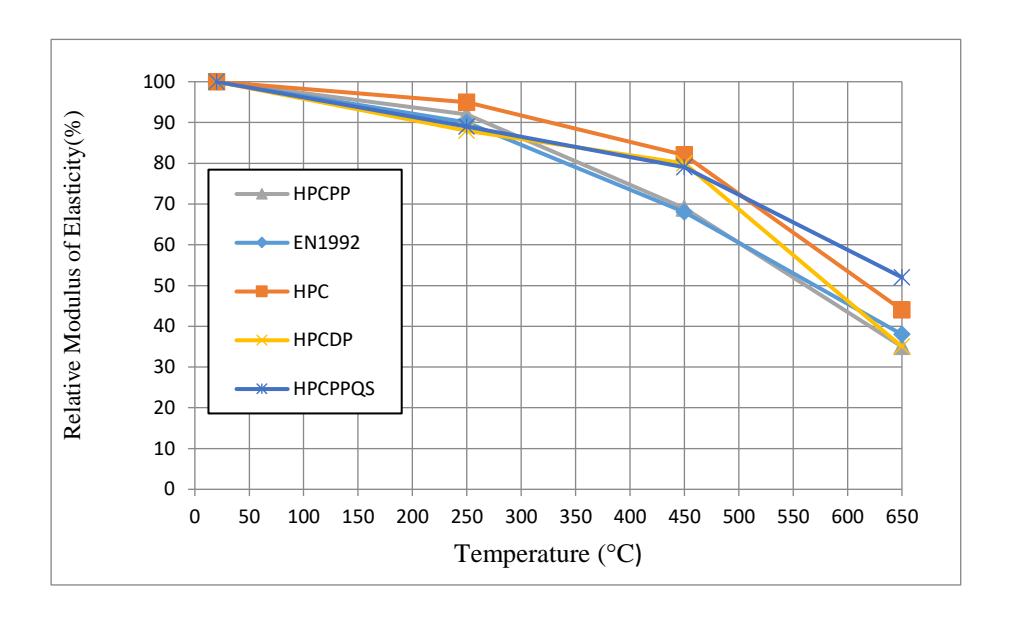


Figure III.6: Relative modulus of elasticity of all types of concrete as a function of temperature

III .4.3 Residual Tensile strength

Figure III. 7 clearly illustrates a continuous and linear drop in Tensile strength up to 450°C for all concrete samples. The curves describe the change in residual tensile strength as a function of temperature for various kinds of concrete. However, a notable loss in strength is shown in every instance as the temperature above this 450°C threshold. In particular, concrete that incorporates palm fibers shows a relatively acceptable Tensile strength compared to other types of concrete, exhibiting only a 55% reduction, similar to the outcome observed with polypropylene-based concrete.

This result arises from the ductile nature of the internal structure of these fibers, which enhances the flexibility of the concrete and prevents the formation of cracks, thus improving its flexural resistance [10,11,12].

Consequently, it can be inferred that replacing polypropylene (PP) with palm fibers (PF) is a viable option to improve the tensile strength of high-performance concrete under fire conditions.

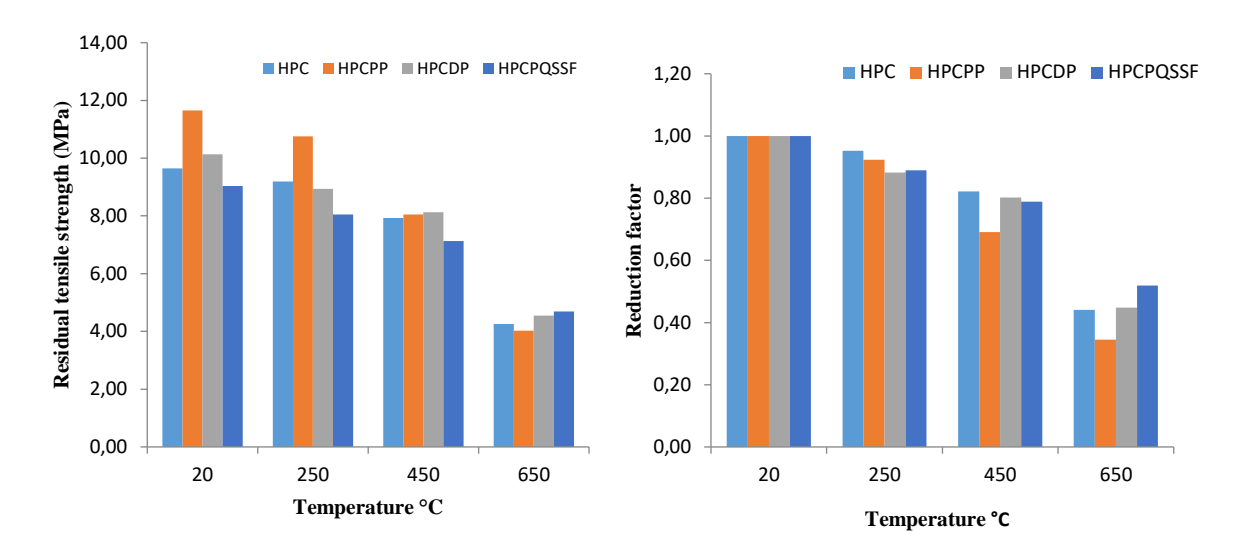


Figure III.7:Residual tensile strength in (a) and reduction factors in (b) versus Temperature

III .4.4 Mass loss

To assess mass loss, we measured the weight of the cubic samples before and after their exposure to elevated temperatures, as shown in Figure III. 8. This representation highlights how the increase of temperature influences the reduction of the concrete mass samples. The correlation between variation in mass loss and temperature is clear for all four types of concrete examined, as noted by several authors [12,13,14]. They found that the variation in mass loss as a function of temperature exposure is linked to the presence of water in the concrete in free, bound, or adsorbed form, which gradually escapes and represents the main cause of the loss of concrete mass. These authors identified three phases in the evolution of mass loss:

In the first phase, from room temperature to 150°C, a slight loss of approximately 3% was observed, corresponding to the release of water contained in the capillary pores.

Between 150 and 300°C, a significant increase in mass loss is observed;

Above 300°C, a slowdown in mass loss is observed. The main physicochemical transformation undergone by heated concrete between 150 and 300 °C is the dehydration of C–S–H;

Above 300°C, a slowdown in mass loss is observed. The main physicochemical transformation undergone by the heated concrete between 150 and 300 °C is the dehydration of CSH.

However, all concrete samples examined in the present study exhibited a significant mass loss from room temperature to 650 ° C. At 250°C, the samples (HPC, HPCPP, HPCDP, and HPCPPQS) recorded a mass loss of approximately 3%, 5%, 7% and 10%, respectively. This trend continues with increasing temperature, reaching approximately 3%, 5%, 7%, and 10% at 450 ° C. On the contrary, mix having palm fibers experiences minimal mass loss between 250 ° C and 450°C, unlike other types of concrete. This difference can be attributed to the fact that palm fibers only melt at very high temperatures, around 1170 ° C [15], thus preserving their

internal structure and improving the properties of this type of concrete. Above 600°C, a significant increase in the rate of mass loss is observed. According to research conducted by Xiao et al. and Zhang et al. [16,17], the phenomena of splitting or degradation of the concrete surface may be linked to many reasons, including the breakdown of limestone particles and CO2 emissions. When compared to other mixes, HPCDP mixes exhibit comparatively less mass loss, but HPC mixes exhibit a more noticeable mass loss than the others. The HPCDP and HPCPPQS blends showed a mass loss of 3.95% at 650°C, but the HPC and HPCPP blends showed a mass loss of 5.02% at that temperature.

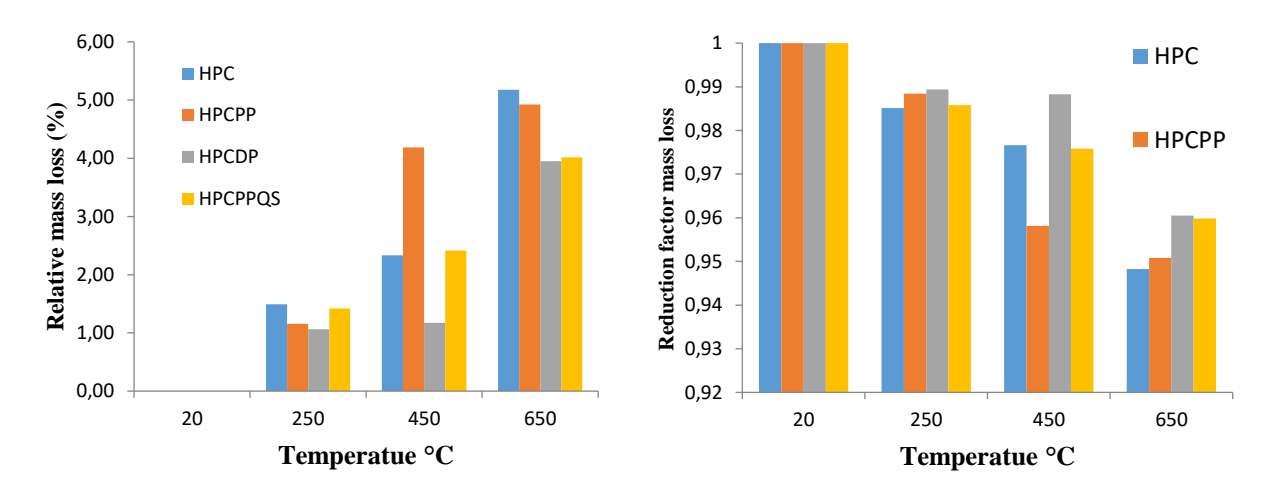


Figure III.8: Residual mass loss and reduction factors as a function of temperature

III .4.5 Ultrasonic Pulse Velocity (UPV)

The evaluation of the elastic modulus and material density was performed utilizing an ultrasonic pulse velocity (UPV) test, in order examine the structural integrity of the different HPC, HPCPP, HPCDP, and HPCPPQS specimens. Figure III. 9 graphically depicts the degradation of concrete integrity as determined by ultrasonic pulse measurements. A discernible decline in UPV values across the temperature spectrum from 250 °C to 650 °C suggests an incremental formation of microcracks within the concrete matrix. At 250°C, the velocity of ultrasonic pulses saw a reduction of 11% in HPCPP specimens and 12% in the different HPC, HPCDP, and HPCPPQS specimens. Moreover, a notable decrease of 58% in ultrasonic pulse velocity was observed at 650°C for all specimens, as illustrated in Figure III .9.

The observed trends indicate a uniform decrease in ultrasonic pulse velocity across the board for specimens of high-performance concrete at elevated temperatures, showing a deterioration in their physical properties and structural integrity.

Additionally, the findings from the UPV test further establish that concrete reinforced with palm fibers exhibits comparable outcomes to other tested concrete variants. This parallel in performance serves as a robust affirmation of the effectiveness and dependability of palm fibers as a reinforcing agent in high-performance concrete (HPC).

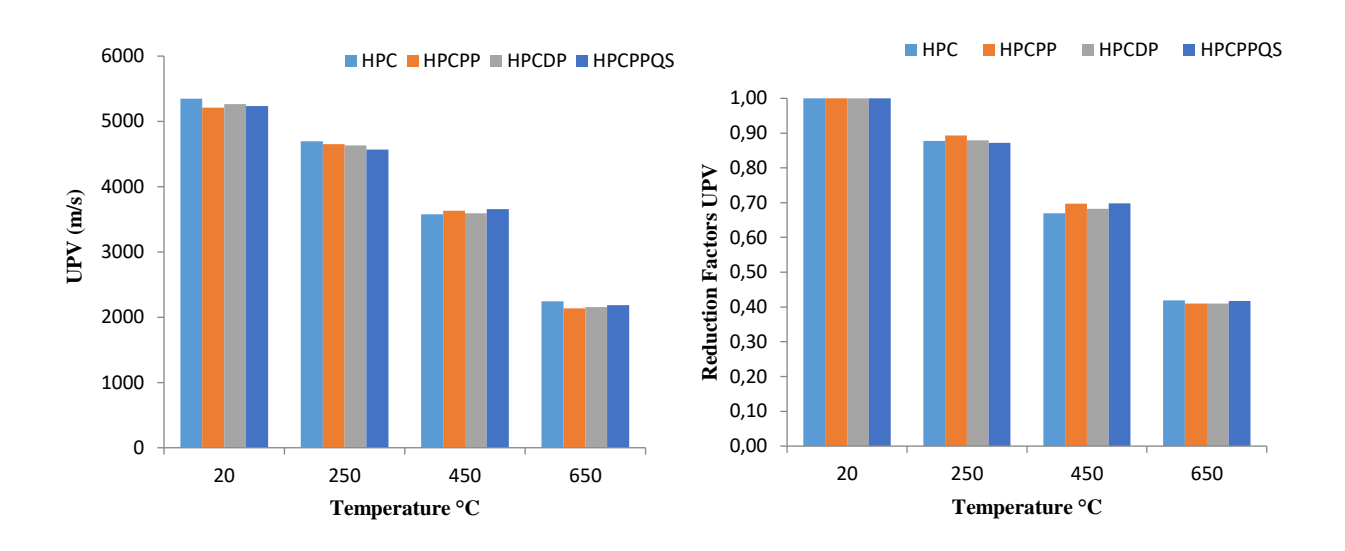


Figure III.9: Ultrasonic pulse velocity and reduction factors as a function of temperature

III .4.6 Observations of spalling behavior

An important aspect of this study involves the examination of the impact of palm fibers on the resistance of HPC to spalling. Following exposure to different elevated temperatures, we recorded observations related to physical characteristics, including spalling frequency, color alterations, and crack formation, to assess their behavior under high-temperature conditions. Fig. 7, 8 and 9 illustrate the concrete surfaces after being treated at high temperatures. An initial assessment of the potential damage due to high temperature exposure can be carried out by examining the external properties of the concrete surface. It is evident that the surface of the samples heated to 250 ° C shows no noticeable changes (Figure III. 10). However, the cracks in the concrete surface began to manifest at approximately 450 ° C (Figure III. 11) and continued to worsen as the temperature increased, reaching their peak at 650 ° C. After exposure to temperatures exceeding 600 ° C, HPCPPQS concrete, which includes polypropylene fibers along with varying proportions of quarry sand and siliceous sand, exhibited light brown discoloration, accompanied by the development of numerous cracks and surface bumps as shown in Figure III. 12d. Furthermore, Figure III. 12 illustrates a color change, providing a visual indication of a notable alteration in the properties of concrete for all types of concrete.

However, it is crucial to emphasize that all types of concrete showed robust resistance to spalling. Despite the presence of several raised bumps on the surface, severe concrete spalling was not observed in these samples, even when exposed to temperatures as high as 650 ° C. Figure III. 12 illustrates the state of these specimens after exposure to a temperature of 650 ° C. When analyzing concrete samples with palm fibers (Figure III. 13), it becomes evident that the spalling phenomenon is entirely absent. Furthermore, this type of concrete shows no cracks up to 450 degrees, and its surface remains intact up to 650 degrees, at which point we observed the appearance of some surface cracks. This clearly illustrates the positive impact of using palm fibers to prevent concrete spalling at high temperatures. This observation has significant economic value by reducing potential costs associated with the use of polypropylene fibers to mitigate spalling in concrete. The utilization of palm fibers proves to be effective not only in terms of performance, but also economically advantageous by preserving the structural integrity of concrete elements exposed to elevated temperatures. This solution offers economic and environmental benefits.

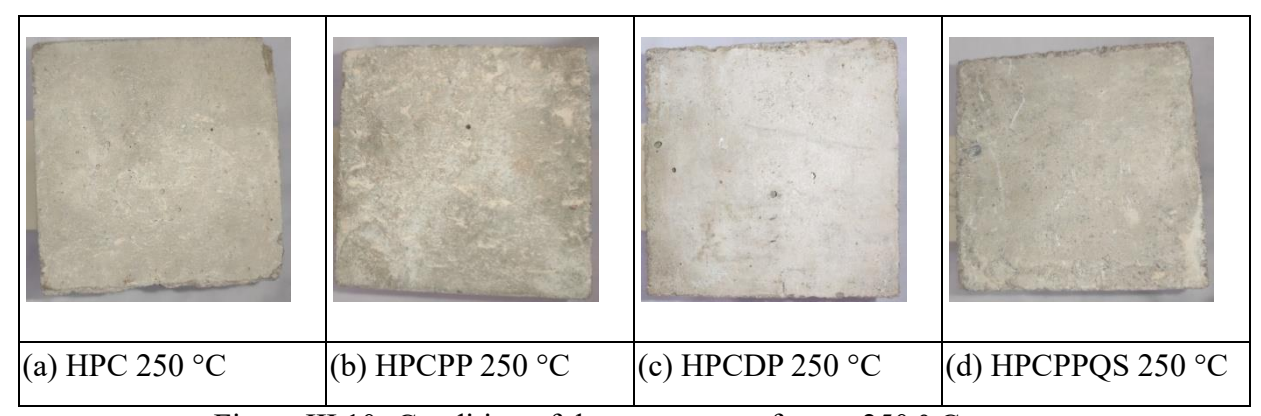


Figure III.10: Condition of the concrete surface at 250 ° C

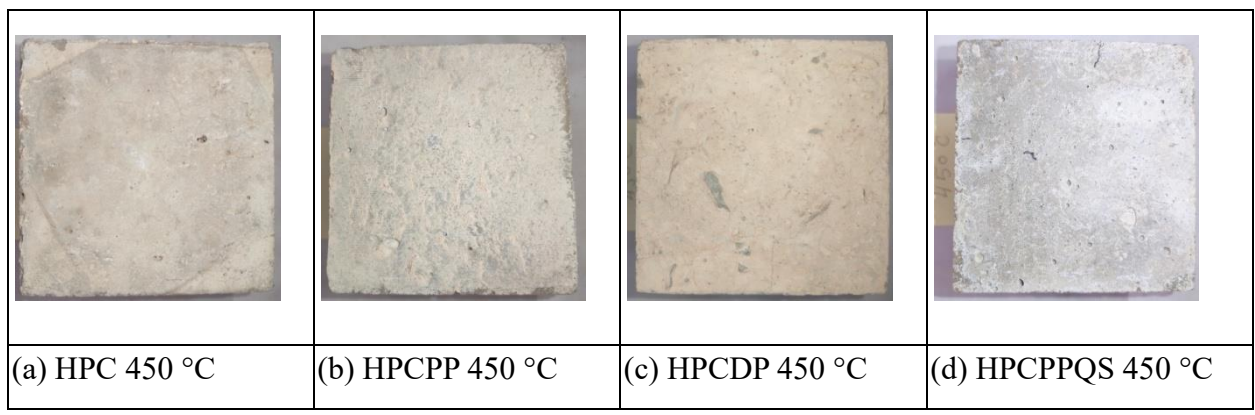


Figure III.11: Condition of the concrete surface at 450 ° C

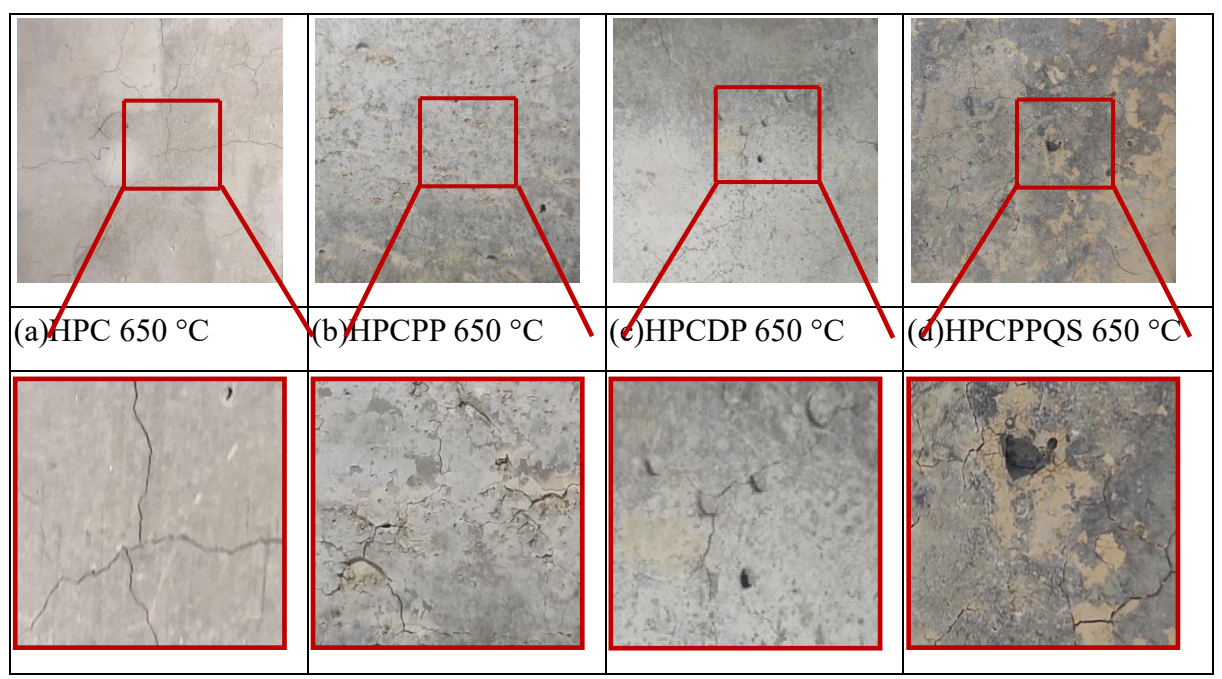


Figure III.12: Condition of the concrete surface at 650 ° C

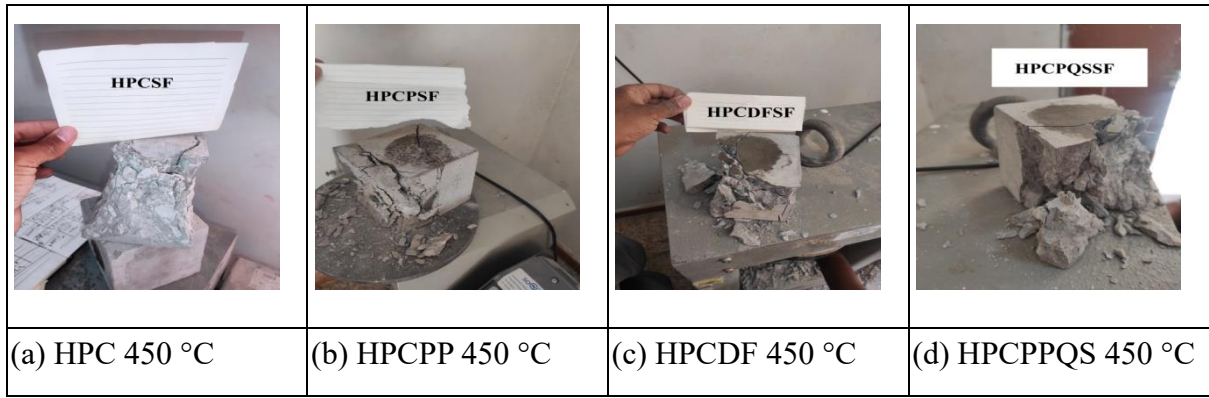


Figure III.13: Condition of the samples after testing their compressive strength after exposure at $450 \,^{\circ}$ C

III .5 Conclusion

This chapter investigated the behavior of high-performance concrete (HPC) under high temperatures, focusing on mechanical properties such as compressive strength, tensile strength, elastic modulus, mass loss, and spalling resistance. The findings demonstrate the significant impact of elevated temperatures on HPC performance and highlight the potential of palm fibers as an alternative reinforcement material.

Key observations include:

A substantial reduction in compressive strength was observed in all concrete types, with palm fiber-reinforced HPC exhibiting a 65% loss after prolonged high-temperature exposure, comparable to polypropylene-based HPC.

The Tensile strength of palm fiber-reinforced HPC decreased by approximately 55%, indicating a notable retention of structural integrity due to the fibers' ductile properties.

Mass loss remained relatively low between 250°C and 450°C, suggesting that palm fibers do not significantly compromise the concrete's density.

Palm fibers contributed to enhanced permeability and reduced thermal spalling, allowing vapor dissipation and mitigating explosive failure risks.

The experimental results align with previous studies, reinforcing the potential of palm fibers in improving HPC's fire resistance.

While these results highlight the feasibility of palm fibers as an eco-friendly and effective alternative for fire-resistant HPC, further research is needed to assess long-term durability, optimize fiber dosage, and evaluate additional properties such as thermal conductivity and microstructural evolution. These insights will be crucial for developing fire-resistant concrete formulations that balance sustainability, mechanical performance, and safety in structural applications.

In the next chapter, we will present an overview of the SAFIR software, detailing its theoretical foundations, algorithms, and validation processes for fire simulations. We then examine the structural resistance of columns, emphasizing the key factors influencing their performance. The core analysis focuses on numerical simulations assessing the load-bearing capacity of reinforced concrete columns under fire conditions. Critical parameters include heating duration, column dimensions, and support conditions. These simulations offer valuable insights into fire-induced structural behavior, aiding in the development of more resilient designs

CHAPTER. IV

Study of the load-bearing capacity of columns exposed to fire

IV.1 Introduction

The assessment of structural behavior under fire conditions requires a realistic representation of fire scenarios. including both the heating and cooling phases. In scenarios where a real fire approach is employed, the duration of required stability may exceed the heating phase and extend throughout the entire fire event until extinction. In such cases, evaluating the structure's load-bearing capacity at the peak gas temperature does not ensure stability at later stages. The structural capacity continues to diminish even after reaching the maximum temperature, hitting a minimum that may partially or fully recover as the structure cools to ambient temperatures. This necessitates a time-dependent, iterative, step-by-step verification method for structural evaluation.

The ongoing degradation of load-bearing capacity post-heating phase is primarily due to two factors:

- 1. Temperature increases during cooling: Temperatures within the structure can continue to rise during the cooling phase. especially in the core of larger sections. prolonging the thermal exposure.
- 2. Material behavior: While steel can recover its strength and stiffness partially or fully as it cools. depending on the type and maximum temperature reached. concrete remains significantly damaged post-cooling. The residual strength of concrete is influenced by the peak temperature during heating and the cooling regime. Additional strength loss of up to 33% has been observed under thermal shock conditions compared to natural cooling.

This study aims to analyze the performance of reinforced concrete columns subjected to natural fire scenarios to determine their residual vertical strength and overall load-bearing capacity. Columns are chosen due to their critical role in structural stability, where failure can lead to local or global instability of the structure. Simulations are conducted using the SAFIR finite element software, incorporating current thermal and mechanical models from Eurocode 2 [1], Eurocode 4 and Practical Guide for Calculating Reinforced Concrete

Sections: According to BAEL 91 Modified 99. [2,16]. Results from Chapter III are used to calculate the columns' load-bearing capacity.

Several physical and mechanical parameters are considered:

- 1. Fire parameters:
 - Heating duration with a stabilization phase
 - Cooling regime

2. Column parameters:

- Simulations on reinforced concrete columns of various heights and crosssections
- Different support conditions
- Exposure to fire on all faces

By focusing on these parameters, the study seeks to identify the most influential factors on the behavior of reinforced concrete columns under fire conditions, thereby enhancing the understanding of their performance and contributing to improved fire safety design guidelines.

IV.2 Introduction to the SAFIR code

Numerical modeling is an invaluable tool for predicting the fire resistance of structures or replicating real fire events. SAFIR (Safe-Fire) is a nonlinear analysis code developed at the University of Liège in Belgium by J.M. Franssen. It employs the finite element method to analyze both two-dimensional and three-dimensional structures. SAFIR is specifically designed to model the behavior of various structural types—steel. reinforced concrete. and composite (steel-concrete)—whether braced or unbraced. under fire conditions. whether conventional or natural. It calculates the temperatures within the structure during a fire and can also analyze structural behavior under ambient conditions. The program determines the load-bearing capacity of structural elements or the entire structure by finding successive equilibrium positions until failure. SAFIR integrates various elements such as SOLID 2D. SOLID 3D. BEAM. SHELL. and TRUSS. and supports multiple material models with linear-elliptical stress-strain laws for steel and nonlinear laws for concrete. It offers various calculation procedures.

Analyzing a structure exposed to fire involves two main steps. The first step. "thermal analysis." predicts the temperature distribution within structural elements. The second step. "structural analysis." determines the mechanical response of the structure to static and thermal loads. SAFIR enables both static and dynamic calculations and includes a comprehensive material library with thermal and mechanical properties. It also supports the modeling of composites made from different materials. Details about the SAFIR software are provided by Franssen. J.M. (2005) [3]. Franssen. J.M. and Gernay. T. (2017) [4]. Kodur VKR et al. (1999) [5]. and Nwosu. D.I. et al. (2007) [6]. The validity of the SAFIR code has been demonstrated in various references. such as Franssen. J.M. et al. (1994) [7]. Pintea. D. and Franssen. J.M. (1997) [8]. and Talamona. D. et al. (2003) [9].

This section outlines the key assumptions. capabilities. and validity of the SAFIR program. and presents comparisons between test results and simulations for concrete structures conducted using SAFIR.

IV.2.1 General organization of the software

The SAFIR software is designed to support various types of finite elements and materials. with its modular nature enabling continuous expansion of its elements and materials library. In the context of fire scenarios, structural analysis necessitates both the determination of temperatures within the structure (thermal analysis) and the assessment of stresses, deformations, and displacements (mechanical analysis). SAFIR facilitates both types of analysis, ensuring seamless information transfer between them. The adopted strategy employs a loosely coupled approach, integrating thermal analysis with mechanical analysis.

Initially, the temperature distribution across different parts of the structure is evaluated until the conclusion of the fire event. Subsequently, the mechanical behavior of the structure is determined through further analysis. The detailed calculation procedure is illustrated in Figure IV.1.

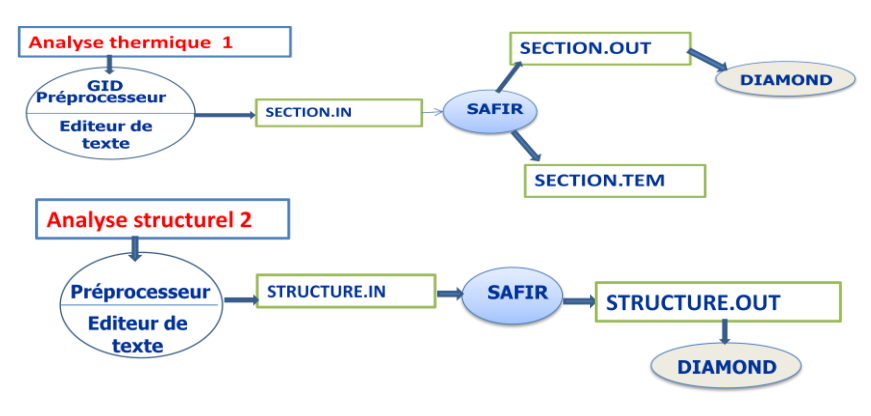


Figure IV.1: Analysis procedure using SAFIR

IV.2.2 Beam element presentation (BEAM)

The beam elements in SAFIR are designed based on several key assumptions:

- Displacement-Type element: Utilizes a total co-rotational description.
- Nodal line displacement:
 - For a 2D element, the displacement is defined by three nodes. Each end node
 accounts for two translations and one rotation, while a mid-length node supports
 the nonlinear longitudinal displacement.

- o For a 3D element. each end node accounts for three translations. three rotations. and warping. allowing for non-uniform torsion. The longitudinal displacement of the nodal line is modeled as a second-order polynomial function of the longitudinal coordinate. The transverse displacement is modeled as a third-order polynomial function of the longitudinal coordinate (see Figure IV.2).
- Bernoulli assumption: Assumes that the cross-section remains plane under bending moments.
- Von Karman assumption: Assumes small deformations.
- Small rotations: Rotations are considered small and are evaluated in the co-rotational configuration.
- Numerical integration: Longitudinal integrations are performed numerically using the Gauss method.
- Fiber model: Longitudinal stress and stiffness integration over the section is based on the fiber model. The section is considered to be made up of parallel fibers. using the same discretization as in the thermal analysis. Each finite element from the thermal analysis. with its known material type and temperature. is treated as a fiber.

This beam element is used to model linear elements such as beams and columns. It also represents truss bars, with at least two finite elements per bar to capture the buckling behavior of individual bars.

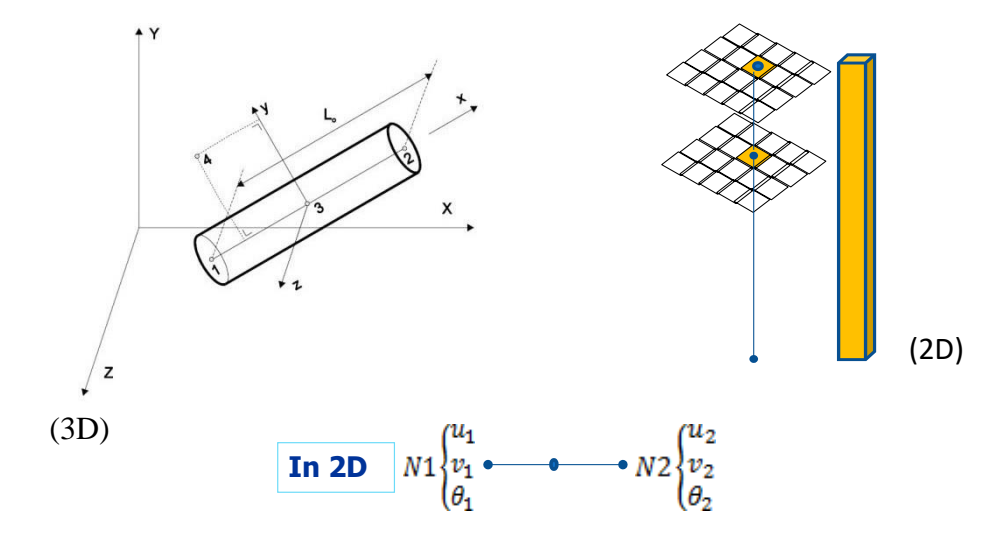


Figure IV.2: Presentation of the beam element

IV.2.3 Thermal actions

SAFIR can model various types of fires in its thermal analysis module. The thermal environment is specified in the code using temperature-time functions for standard fires (e.g. ISO 834. ASTM 119 (tabulated). external fire. hydrocarbon fire) and natural fires (parametric fires). including the cooling phase. Additionally, user-specific fire scenarios can be introduced.

IV.2.4 Thermal analysis

The thermal analysis in SAFIR operates under the assumption that heat conduction is the primary mechanism of heat transfer within elements. as described by Fourier's equation. The primary assumptions for this analysis include:

- Negligible temperature variation along the longitudinal direction.
- Materials are assumed to be isotropic. stationary. incompressible. and free from mechanical dissipation.
- The contact between concrete and steel is considered perfect. though a fictitious material with thermal resistance between 0.01-0.013 m²K/W can be introduced between them.
- Thermal exchanges via convection and radiation within cavities can be accounted for.
- No material discontinuity exists between adjacent elements.
- Temperature at the common boundary of two elements is assumed to be the same.
- The variation in thermal properties of materials with temperature is in accordance with Eurocode standards or user-defined values.
- The transport of water vapor is not considered.

The modeling elements are linear iso parametric. with 3 or 4 nodes for planar problems and 6 or 8 nodes for three-dimensional problems. Both the geometry of the elements and the temperature field are represented using the same interpolation functions. Discretization of plane sections with different shapes is possible using triangular and/or quadrilateral elements (Figure IV.3). Each element's material properties can be defined separately. allowing for analysis of any material based on its temperature-dependent properties.

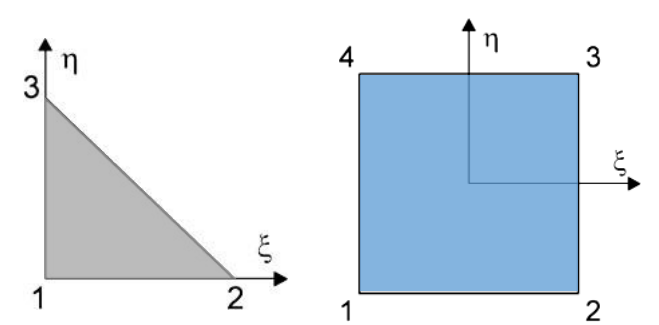


Figure IV 3: Linear iso parametric elements

Heat transfer by conduction in a solid is locally described by Fourier's equation:

$$\frac{\partial}{\partial x} \left(\lambda \frac{\partial T}{\partial x} \right) + \frac{\partial}{\partial y} \left(\lambda \frac{\partial T}{\partial y} \right) + \frac{\partial}{\partial z} \left(\lambda \frac{\partial T}{\partial z} \right) + Q = \rho c \frac{\partial T}{\partial t}$$
 (IV.1)

- T: The temperature at point x.y.z in [°C]
- ρ: The density in [kg/m3]
- c: The specific heat capacity in [J/kg°C]
- λ: The thermal conductivity of the medium in [W/m°C]
- t: The time in seconds [s]
- Q: The internally generated heat in [W/m2]

Classical shape functions N are used. and the temperature is replaced by the approximation T=NiTi. The geometry is represented by the same function: x =Nixi and y=Niyi. The solution discretized by these equations no longer satisfies the local equation at every point. Instead. we replace this equation (IV.1) with a weak form that will be respected on average over each element (method of weighted residuals). We multiply Eq. (IV.1) by weighting functions and integrate the result over the volume of the element.

If we choose the interpolation functions used for the discretization as the weighting functions (Galerkin method) and integrate the left-hand side by parts using Green's theorem. we obtain the following equation for each finite element:

$$\int_{V} \lambda \{\nabla \text{Ni}\} \langle \nabla \text{Nj} \rangle \, dV \text{Ti} + \int_{V} \rho \, c \text{NiNjV} \, dV \text{Ti} = \int_{S} \text{NiqndS} \qquad (IV.2)$$

- Volume of the element V: The three-dimensional region occupied by the finite element.
- Surface of the element S: The boundary surface enclosing the volume of the finite element.

• Heat flux at the surface: This includes both convection and radiation components. The heat flux qn at the surface is given by: $qn = \lambda \frac{\partial T}{\partial n}$

where λ is the thermal conductivity. $\frac{\partial T}{\partial n}$ is the temperature gradient in the direction normal to the surface, and n is the normal vector to the surface.

Finally, after assembling the contributions from each element. we obtain the following matrix equation that represents the equilibrium at the nodes of the analyzed structure:

$$M\frac{\partial T}{\partial t} + KT = F$$
 (IV.3)

- M is the mass matrix. representing the heat capacity contributions from each element.
- $\frac{\partial T}{\partial t}$ is the vector of temperature time derivatives at the nodes.
- K is the stiffness matrix. representing the thermal conductivity contributions from each element.
- T is the vector of nodal temperatures.
- F is the vector of external heat flux contributions. including both internal heat generation and surface fluxes such as convection and radiation.

it should be noted that in the SAFIR program. the integration over the volume of the elements is performed numerically. and the thermal properties of the materials are evaluated at each integration point. Detailed information on the method can be found in Franssen. J.M. (2009) [3]. and Kodur. V.K.R. and Dwaikat. M.M.S. (2008) [10].

IV.2.5 Structural analysis

Under the action of fire, structures are the seat of large displacements, and the need for accurate determination of displacements means that the non-linearity arising from the geometry (second-order effects associated with the deformed configurations of the structure) must be taken into account, in addition to a non-linearity characterized by the non-linear behavior of the construction materials.

To deal with this type of problem. the equilibrium of the structure must be expressed in its deformed configuration and the finite element formulation must be introduced in incremental form (by introducing a time variable to describe the loading and movement of the structure) and iteratively (to take account of non-linearities). which, starting from an approximate

solution. generates successive corrections to converge on the exact solution of the problem. The updated Lagrangian co-rotational description is adopted in the software. The formulation and assembly of the elements are based on the principle of virtual work expressed in this description, which is defined by Eq (IV.4).

Surface actions are not considered.

$$\int_{V} (\overline{D}ijkl \, d\overline{E}kl \, \delta \overline{E}ij + \, Sij \, \delta d\overline{E}ij) \, dv = \int_{V} (d\overline{f}i\delta \overline{u}i + \, \overline{f}i \, \delta \overline{u}i) \, dv \qquad \text{(IV.4)}$$

 $V = \bar{V}$: Unreformed volume of the element.

Sij: Piola-Khirchoff stress tensor n°2.

 $\overline{D}ijkl = Dijkl$: Tensor describing the incremental constitutive law of the material.

 $\delta \overline{E}ij$: Green's tensor of the virtual displacement field.

 $\delta \overline{E}ij$: Volume forces.

 $\delta \bar{u}i$: Virtual displacement field of the deformed position.

In a material where the temperature changes, the incremental constitutive law is given by Eq (IV.5).

$$\delta S_{ij} = D_{ijkl} \left(dS_{kl} - dE_{lk}^{th} \right) = D_{ijkl} dE_{kl}^{m}$$

Where:

 dE_{kl} : Total. mechanical and thermal strain tensor

 dE_{lk}^{th} :Incremental tensor of thermal deformations

 dE_{kl}^{m} Incremental mechanical strain tensor implicit form

The Green's tensor of the virtual displacement field is given by Eq (IV.6).

$$\delta \bar{E}ij = \frac{1}{2} (\delta \bar{u}i.j + \delta \bar{u}j.i + \bar{u}k.i \delta \bar{u}k.j + \delta \bar{u}k.i \bar{u}k.j)$$
(IV.6).

In order to solve Eq. (III.4) using a finite element formulation based on displacements. the displacement field is approximated by a discretized field u. This field is expressed as a function of the nodal displacements p through a set of appropriately chosen shape functions NNN. The matrix representation of the discretized displacement field is given by Eq. (IV.7).

$$u = Np$$
 (IV.7)

The strain field is provided in Eq. (IV.8).

$$de = Bdp$$
 (IV.8)

In this framework, the matrix B incorporates both the spatial derivatives of the shape functions, as in the small strain formulation, and the nodal displacements that are non-zero in

the deformed state. The matrix equilibrium equation governing the iterative process from one configuration to the next is defined in Eq. (IV.9).

$$\int_{V} B^{T} DB dv dp + \int_{V} S^{T} \delta de dv dp = (K_{u} + K_{s}) dp = f^{ext} - f^{int}$$
(IV.9)

Where:

- \bullet K_u : Includes the linear elastic stiffness matrix and the geometric stiffness matrix
- K_s : Represents the matrix of generated stresses
- f^{ext} : Vector of applied nodal forces
- f^{int} : Nodal forces obtained by integrating internal stresses (based on the principle of virtual work)

The 3D beam element is introduced in this section with the following assumptions:

- The element is considered prismatic in its reference configuration. Only straight beams are analyzed. as they represent the majority of practical applications.
- The spatial orientation of the element is defined by the positions of three nodes. as illustrated in Figure IV.4. Nodes 1 and 2 are located at the element's endpoints and are connected by a nodal line. which the user can arbitrarily define. These nodes share the same position within the cross-section, though not necessarily at the section's centroid or torsion center.
- The local x-axis is established along the nodal line. oriented from node 1 to node 2. with its origin at the midpoint between the two nodes.
- Node 4. which must not lie along the line passing through nodes 1 and 2. determines the orientation of the local y-axis. This axis is orthogonal to the x-axis and lies within the plane defined by the x-axis and node 4. with its direction oriented from the x-axis towards node 4.

• The z-axis is determined by the cross product of the x- and y-axes. ensuring orthogonality according to the right-hand rule.

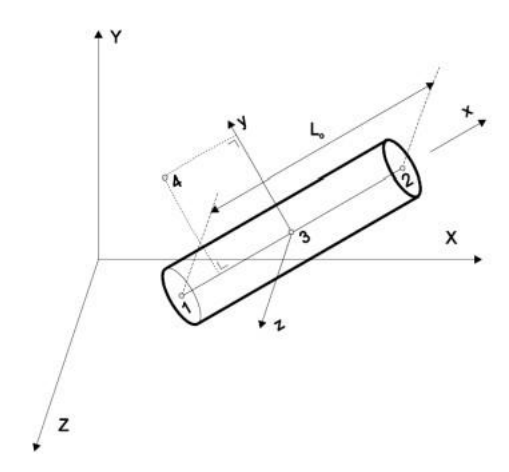


Figure IV.4: Description of the Beam Element.

- The displacement of the nodal line is governed by the motion of three nodes. Each of the end nodes (1 and 2) features 7 degrees of freedom. including 3 translational components. 3 rotational components. and a warping amplitude. Node 3. with a single degree of freedom. is incorporated to enrich the displacement field. This node transforms the longitudinal displacement of the nodal line into a second-degree nonlinear function in x. while the transverse displacements are modeled using a third-degree polynomial function.
- The Bernoulli hypothesis is adopted. implying that in the absence of torsion. shear deformations are negligible. Consequently. under pure bending. the cross-section remains perpendicular and planar to the element's axis. and shear energy is disregarded.
- Local buckling is not considered for the element. Only class 1 and class 2 cross-sections are used. corresponding to steel elements.
- The Von Karman hypothesis is applied. assuming small deformations. meaning that each deformation component is small relative to unity. with:

$$\frac{\partial u}{\partial r} \ll 1$$
 (IV.10)

u: Longitudinal displacement field

X: Longitudinal coordinate

• The rotations are assumed to be moderate. with the following approximation (distinct from corotational formulations):

$\sin \varphi \cong \varphi$. $\cos \varphi \cong 1$ with φ : the rotation

- The Vlasov hypothesis is adopted, stating that under pure torsion, the cross-section undergoes warping with an amplitude proportional to the increase in the torsional angle.
 This assumption neglects the strain energy associated with the shear deformation caused by the warping of the section.
- Longitudinal integrations are numerically performed using the Gauss method.
- The cross-section is discretized using triangular and quadrilateral elements. the same discretization employed in the thermal analysis. Each finite element, with its specific material properties and temperature, is treated as a fiber element. Thus, the section is assumed to consist of parallel fibers. The integration of stresses and stiffness across the section is based on this fiber model, where all variables, including temperature, stress, and strain, are assumed to be uniform within each fiber.
- The tangent stiffness matrix is evaluated at each iteration using the convergence process (pure Newton-Raphson method).
- Residual stresses are accounted for by introducing constant initial strains.
- The material behavior during unloading is assumed to be elastic. with the modulus of
 elasticity corresponding to the initial Young's modulus on the stress-strain curve.
 Within the same cross-section, some fibers that have undergone plastic deformation
 exhibit reduced stiffness, as they remain on the loading path, while other fibers behave
 elastically. Plastic deformation is assumed to be unaffected by changes in temperature.
- The elastic torsional stiffness at 20°C. calculated by the code. is iteratively adjusted to reflect the reduction in material stiffness at the critical temperature.
- The effect of thermal expansion of steel and concrete is incorporated into the behavioral models.

For the simulations conducted in this study. a 2D beam element is used, with two translational degrees of freedom and one rotational degree of freedom at each end node. A third node at the midpoint of the element supports a second-degree nonlinear displacement enrichment.

IV.2.6 Fundamental assumptions applied in the numerical simulations

The following assumptions were adopted for the numerical simulations of the structural behavior of the columns:

Each column is subdivided into n beam elements along its height. incorporating a lateral geometric imperfection described by the following expression:

$$y(x) = \frac{h}{1000} \sin\left(\frac{\pi x}{l}\right)$$
 (IV.11)

For steel and reinforced concrete columns, the mid-span deflection can reach a value on the order of h/1000

IV.2.7 Comparison and verification of the SAFIR code

IV.2.7.1 Validation of the thermal model

The SAFIR software was validated by comparison with multiple experimental tests and other computational models. Binh. C.T. (2009) [11] successfully reproduced the results of 27 tests conducted across Europe and Canada. These experiments were performed at various institutions: The University of Braunschweig. Germany (Kordina. K. and Klingsch. W. 1983). CTICM. France (Renaud. C. et al.. 2004). and in North America at the National Research Council of Canada (Chabot. M. and Lie. T.T. 1992; Myllymäki. J. et al. 1994).

Comprehensive details of the experimental setups can be found in [11]. with only the resulting temperature curves reported here.

Figure IV.5. Figure IV.6 and Figure IV.7 display the temperature evolution at specific locations for all tests: on the steel profile's surface. within the reinforcement, and at the core of the concrete section.

The simulation results demonstrate good agreement between the predicted temperatures for the concrete-filled steel hollow sections and the measured temperatures from the experiments.

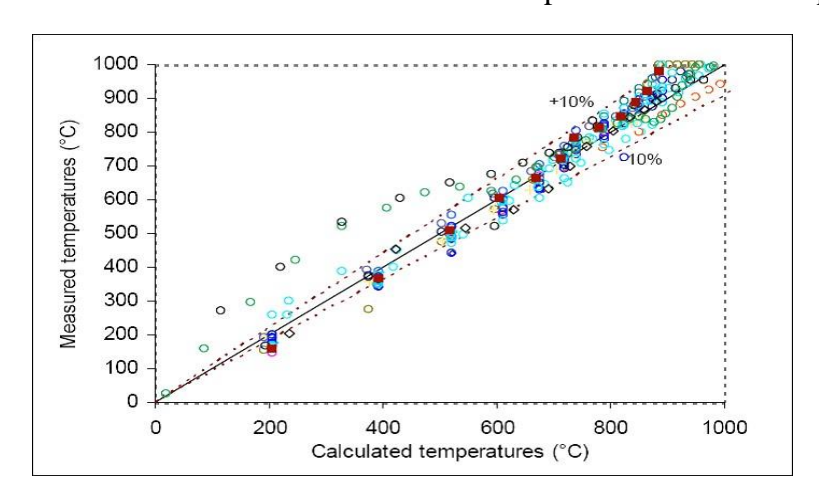


Figure IV.5: Comparison between the calculated and measured temperatures on the surface of the steel tube across various tests.

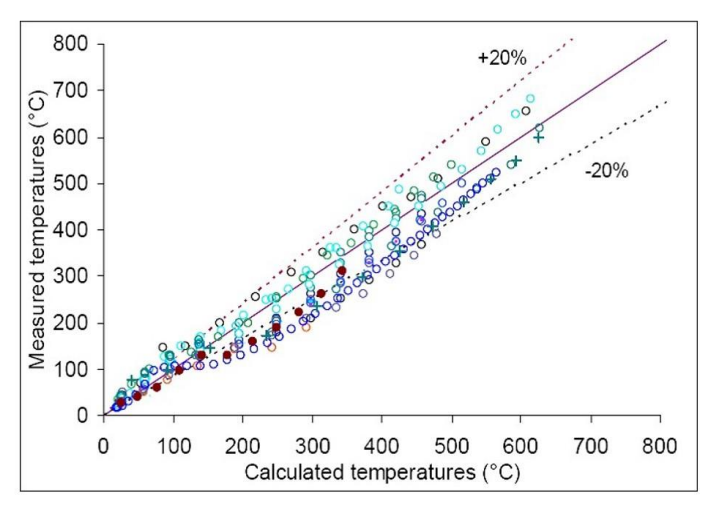


Figure IV.6: Comparison between the calculated and measured temperatures in the concrete core across various tests.

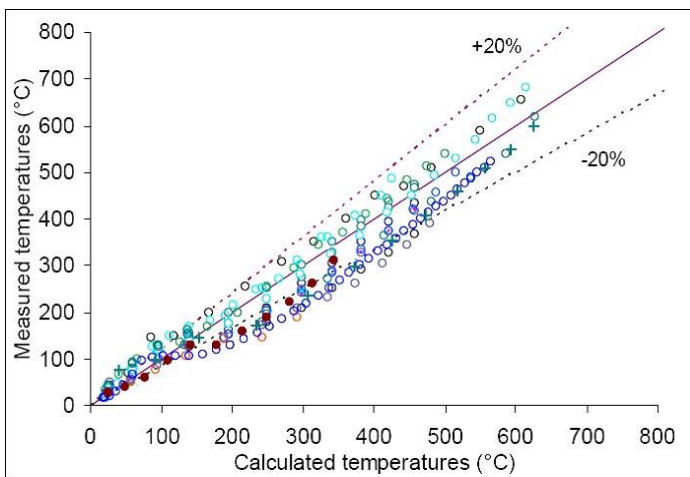


Figure IV.7: Comparison between the calculated and measured temperatures in the reinforcements across various tests.

IV.2.7.2 Structural model validation

For the validation of the structural model, a comparison was made between the calculated failure time and the measured failure time for the same tests referenced in the thermal validation. Table IV.1 summarizes all the results obtained through simulation and compares them with the measured results.

The model effectively simulates the behavior of composite columns and provides a reliable estimation of fire resistance due to the selection of appropriate material laws and the initial introduction of a geometric imperfection. Consequently, the model can be employed to study the parametric behavior of columns under fire conditions. Composite columns were selected because of the presence of three distinct materials in this type of element.

Table IV.4: Fire resistance of columns. measured and calculated

						Measured	Calculated	
Test			Length	Test loa	ding	failure time	failure	Rcal/Rtest
						Rtest	time Rcal	
Number	Section	Rebars	mm	Load (kN)	e (mm)	(min)	(min)	
1	200*6.3	4Ø18	4200	432	20	63	50.8	0.81
2	200*6.3	4Ø18	4200	318	50	58	53.8	0.93
3	200*6.3	4Ø18	4200	537	5	61	48.1	0.79
4	200*6.3	4Ø18	4200	213	100	79	60.4	0.76
5	260*7.1	4Ø18	4200	1237	26	37	49.6	1.34
6	300*7.0	4Ø18	4200	1000	30	90	89.2	0.99
7	200*6.3	4Ø18	3700	649	20	39	47.8	1.23
8	200*6.3	4Ø10	4200	551	20	23	24	1.04
10	200*6.3	4Ø18	3700	649	20	56	52.9	0.94
12	200*6.3	4Ø18	4200	550	5	59	51.4	0.87
13	200*6.3	4Ø18	3700	294	20	82	66.3	0.81
15	220*6.3	4Ø18	4200	375	22	68	60.5	0.89
16	220*6.3	6Ø20	4200	421	22	88	83.6	0.95
17	260*7.1	6Ø22	4200	869	26	64	75.3	1.18
18	300*7.0	6Ø25	4200	1507	30	56	70.1	1.25
24	203*6.35	4Ø16	3810	500	0	150	84	0.56
25	254*6.35	4Ø16	3810	1440	0	113	82	0.73
	•		•		•			
							Rmean=	0.95
							standard	
							deviation=	0.201

A. Tests considering the cooling phase

A series of fire experiments was conducted by Wu. B. and Chen. S.L. (2010) [12] on 12 reinforced concrete columns with different cross-sections (T. +. and L) at the South China University of Technology. For each type of section. four columns were prepared. Each column was reinforced with 12 Ø10 bars. uniformly distributed. with a steel reinforcement ratio of 2.36%. The columns were 2340 mm in length. with only the central section (1650 mm) exposed to ISO 834 fire on all sides. The fire was extinguished when approximately 50% of the working load had been transferred from the column to the bracing beam. followed by a cooling phase. The SAFIR software was used for the numerical simulation of the tests. performing both thermal and structural analyses. Figure IV.8 presents the typical temperature profiles recorded at four different points along the mid-height section of the column. The temperature curves show a satisfactory correlation. although the calculated values are slightly lower than those recorded during the cooling phase.

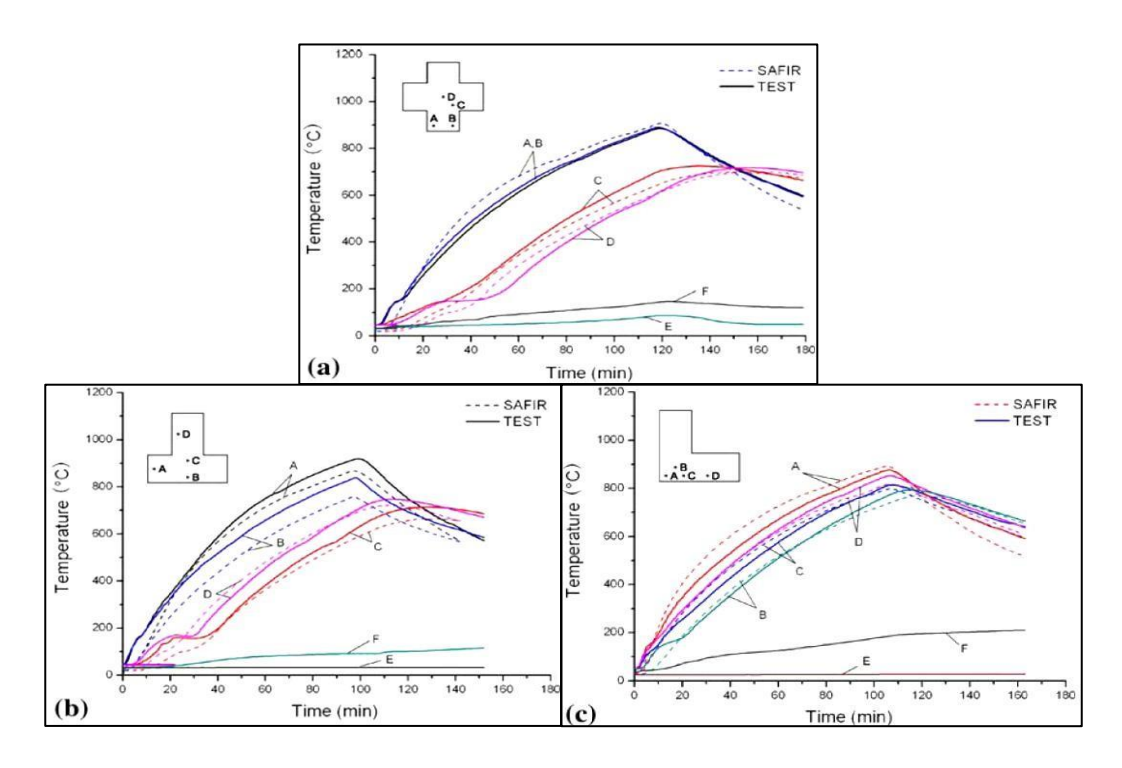
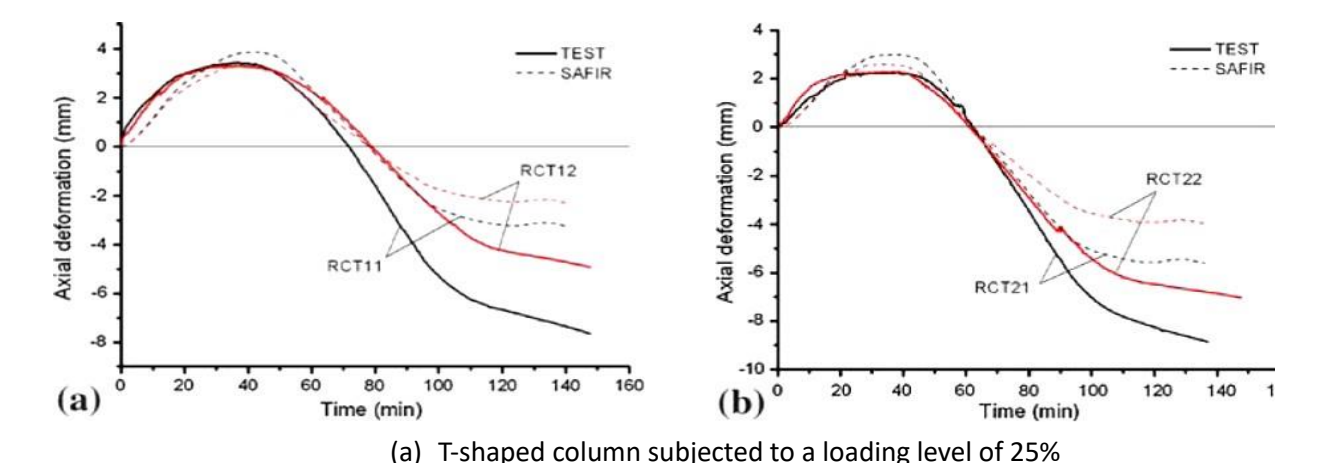


Figure IV.8: Comparison of temperatures calculated by SAFIR and measured in different sections: (a) RC+12. (b) RCT11. and (c) RCL12 [5]

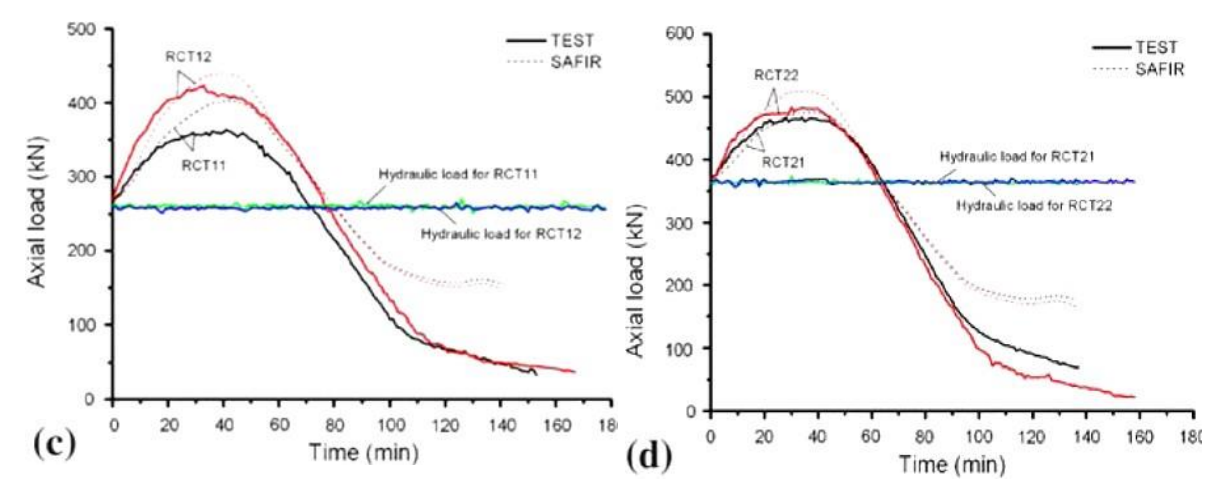
For the structural analysis. Figure IV.9 and Figure IV.10 compare the simulation results obtained using SAFIR with the measured values of axial displacement and normal force in the columns over time.

During the heating phase, the predictions from SAFIR closely align with the measured displacement values. However, discrepancies in the normal force remain unexplained, potentially due to handling issues during the experiments. In the cooling phase, the observed differences can likely be attributed to the reversible nature of the model.



(b) T-shaped column subjected to a loading level of 35%

Figure IV.9: Axial displacement-time relationships



- (c) T-shaped column subjected to a loading level of 25%
- (d) T-shaped column subjected to a loading level of 35% Figure IV.10: Axial force-time relationships.

IV.3 Description of the study

IV.3.1 Physical and mechanical properties of materials

IV.3.1.1 Thermal model

The thermal properties of concrete and steel during the heating phase are derived from EN 1994-1-2 (Eurocode 4) [2]:

A- Concrete

The concretes HPC. HPCPP. HPCDP. and HPCPPQS have been selected, each with its unique properties summarized in the following table. Their densities vary as shown, and water content is provided accordingly. During heating, the specific mass of the concrete decreases due to the complete evaporation of internal moisture. However, during cooling, it is assumed that the specific mass remains constant, corresponding to the value at the maximum temperature reached. Each type of concrete has a characteristic compressive strength at 28 days (f_c28) measured at ambient temperature, as listed in the Table IV.2. Tensile strength for all types is neglected in calculations.

Additionally, the thermal conductivity of the concrete is taken at its upper limit. As the temperature within the concrete increases, the thermal conductivity tends to decrease (EN 1994-1-2 [2]). This decrease is not reversible upon cooling, and the thermal conductivity is maintained at a constant value corresponding to the one determined at the maximum temperature.

Table IV.5: Characteristics of the HPC mix

Concrete type	Density (kg/m³)	Compressive strength (MPa)
HPC	2583.8	113.5
HPCPP	2460.9	105.92
HPCDP	2425.8	92.12
HPCPPQS	2455.9	95.17

B- Steel

The behavior law and thermal properties are specified with EN 1994-1-2 [2]. These properties are assumed to be fully reversible during the cooling phase. The thermal properties required to calculate heat transfer and temperature distributions within the structures include thermal conductivity and specific heat. both of which are considered nonlinear.

The key physical property required for structural analysis is thermal elongation. The emissivity of steel is set to 0.7. and the convection coefficient is taken as 35 W/m²K.

IV.3.1.2 Mechanical properties

The reinforcement bars used in reinforced concrete are classified as S400. with their mechanical properties assumed to be reversible. This implies that both stiffness and strength are fully restored to their initial values upon cooling. In the thermal elongation curve, the plateau corresponds to a phase transformation occurring around 800° C, with an elongation value of 11×10^{-3} . This transformation may initiate at slightly lower temperatures, approximately 700° C, with a corresponding value of 9×10^{-3} . Upon cooling, as the steel returns to ambient temperature, no residual thermal expansion is observed.

For concrete, residual thermal expansion or shrinkage was considered when the material returned to ambient temperature. Its residual value depends on the maximum temperature reached and is determined through experimental testing (Schneider U. 1985) [13]. Spalling is not considered in this study by assumption. The compressive strength of concrete does not recover upon cooling. According to EN 1994-1-2, an additional 10% loss in compressive strength is accounted for during cooling. For example, if the compressive strength decreases from 1.00 to 0.50 at a given temperature, it will further decrease to 0.45 upon returning to ambient temperature. This assumption is crucial for all the predictions presented in this research regarding the residual vertical load-bearing capacity of the columns under study. following the complete duration of the fire scenario to which they were exposed.

In a recent study. Li and Franssen (2011) [14] demonstrated, based on the analysis of certain experimental results reported in the literature, that the additional reduction in compressive strength during cooling can be even greater than the 10% reduction specified in EN 1994-1-2 (Figure IV.11). In the stress-strain relationship of concrete, the strain corresponding to the peak stress during cooling is considered fixed, corresponding to the value prevailing at the maximum temperature (Felicetti, R. et al., 2002) [15].

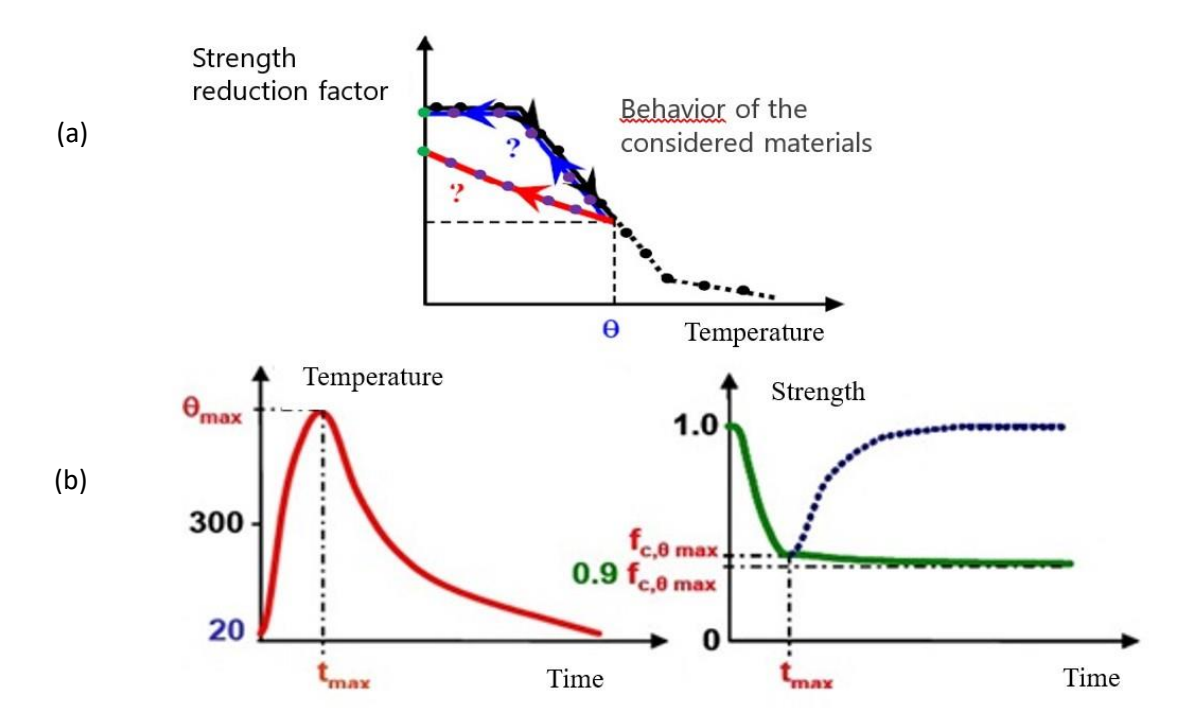


Figure IV.11: Behavior of materials exposed to fire. a) Evolution of strength as a function of temperature (T°). (b) Behavior of concrete after cooling.

IV.3.2 Numerical analysis process

During the thermal analysis phase. the temperature distribution within the cross-sections was determined using nonlinear 2D transient analyses. The SAFIR software models heat transfer within solid structures predominantly through conduction. while at the structural boundaries. heat exchange with the environment occurs via convection and radiation.

For heat conduction in concrete, the heat exchange is governed by Fourier's equation, expressed in a cartesian coordinate system. The software employs an iterative process that evaluates temperatures across multiple time steps until thermal equilibrium is achieved. The results from the thermal analysis were subsequently implemented in the structural modeling.

For the structural analysis, the columns were discretized longitudinally using Bernoulli beam elements, and the cross-sections of these beam elements were divided into fibers corresponding to the 2D elements used in the thermal analysis.

IV.3.2.1 Thermal analysis of reinforced concrete columns

For the present analysis, the same time-temperature curves used in Chapter III for the experimental study have been selected to be applied as the thermal load for the columns under study (Figure IV.12). In the discussion of the results, the following terms will be used:

Phase 1: Increasing Temperature Phase (ITP)

The heating cycle involved a heating rate of approximately 3 to 8°C/min until the target temperature was reached.

Phase 2: Stabilization Phase (SP)

During this phase. the temperature was maintained constant for a duration of 90 minutes.

Phase 3: Fire Cooling Phase (FCP)

In this phase, the gas temperature decreases from the maximum temperature to ambient temperature (20°C) with an average cooling rate of about 1°C/min at the beginning of the cooling phase.

Phase 4: Residual Phase (RP)

This phase occurs when the concrete temperature returns to ambient temperature (20°C). It corresponds to the post-fire phase.

These temperature curves are applied to the reinforced concrete columns on all four sides

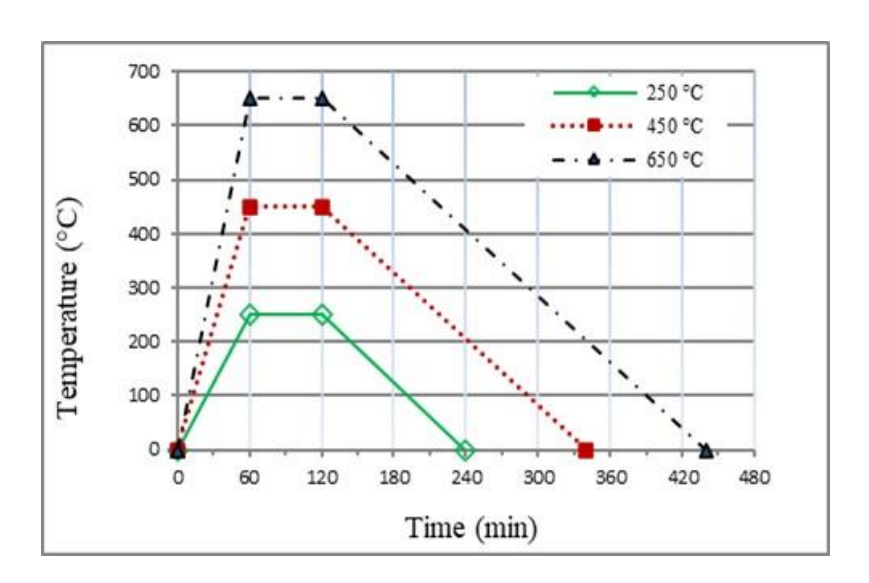


Figure IV.12: Thermal treatment curve of the column: heating – stabilization – cooling

IV.3.2.2 Structural analysis

A. Analysis for the evaluation of vertical load-bearing capacity

The selected sections are commonly used in construction in Algeria. The studied columns have square sections of 30x30 cm and 40x40 cm. The square sections are reinforced with 4 or 6 bars with a concrete cover of 30 mm.

One of the objectives of this chapter is to provide insights into the parameters and conditions that may influence the residual load-bearing capacity of the column during the cooling phase or after cooling. The parameters considered are:

- Influence of heating duration (various fire scenarios).
- Influence of the effective height of the column.
- Influence of section variation.
- Influence of support conditions.
- Influence of concrete mix types

In this section, a reference column with a height of 3.00 meters and a 30x30 cm section is presented in most cases.

IV.3.3 Thermo-Mechanical modeling of the behavior of columns

IV.3.3.1 Temperature distribution in the sections

Figure IV.13 and Figure IV.14 depict the evolution of temperature distribution across the 30x30 cm column section with a 30 mm cover during the heating and cooling phases of fires at 250°C. 450°C. and 650°C. The results highlight the influence of different concrete mix types—HPC. HPCPP. HPCDP. and HPCPPQS—on the temperature distribution.

At the end of the warm-up phase (60 minutes). the maximum temperatures at the corner of the columns were 186.7°C. 188.0°C. 187.6°C. and 188.1°C for HPC. HPCPP. HPCPP. and HPCPPQS. respectively. under the 250°C fire. For the 450°C fire. these temperatures increased to 395.4°C. 397.4°C. 398.0°C. and 397.4°C. and for the 650°C fire. they reached 623.2°C. 624.5°C. 624.8°C. and 624.6°C. This demonstrates that the temperature distribution is influenced by both the fire intensity and the concrete mix type.

At the end of the stabilization phase (120 minutes). the temperatures at the exposed face were 192.0°C. 193.4°C. 193.9°C. and 193.5°C for the 250°C fire. 392.9°C. 394.8°C. 395.5°C. and 394.8°C for the 450°C fire. and 608.3°C. 609.8°C. 610.3°C. and 609.9°C for the 650°C fire. These results indicate that the addition of fibers (polypropylene or date palm) slightly influenced the temperature distribution. with HPCDP showing marginally higher temperatures compared to other mixes.

During the cooling phase (940 minutes). the temperatures at the center of the section decreased significantly but remained higher than at the surface. For the 250°C fire, the center temperatures were 39.6°C, 38.3°C, 37.8°C, and 38.3°C for HPC, HPCPP, HPCPP, and HPCPPQS, respectively. For the 450°C fire, these values were 58.7°C, 56.2°C, 55.4°C, and 56.2°C, and for the 650°C fire, they reached 120.3°C, 115.2°C, 113.5°C, and 115.2°C. This confirms that the center of the section retains heat longer, even after the cooling phase, due to the thermal inertia of the concrete.

The temperatures of the reinforcement bars near the exposed face also varied significantly. At the end of the stabilization phase, under the 250°C fire, the bar temperatures were 150.3°C. 152.5°C. 153.3°C. and 152.7°C for HPC. HPCPP, HPCPP, and HPCPPQS, respectively. For the 450°C fire, these values increased to 295.0°C. 299.4°C. 300.9°C, and 299.4°C, and for the 650°C fire, they reached 566.9°C. 444.1°C. 446.1°C, and 444.5°C. The higher temperatures in the bars for the 650°C fire highlight the critical role of the 30 mm cover in providing thermal insulation and delaying the temperature rise in the reinforcement.

These results demonstrate that the type of concrete mix and the presence of fibers influence the thermal behavior of columns under fire conditions. The addition of date palm fibers (HPCDP) showed a slight improvement in thermal resistance compared to other mixes. particularly at higher temperatures. These findings emphasize the importance of material selection and cover thickness in ensuring the structural integrity of columns during and after fire exposure.

Table IV.3 illustrate the evolution of the maximum temperature at different points in the concrete and reinforcement bars for the 30x30 cm column exposed to fires of 250°C. 450°C. and 650°C

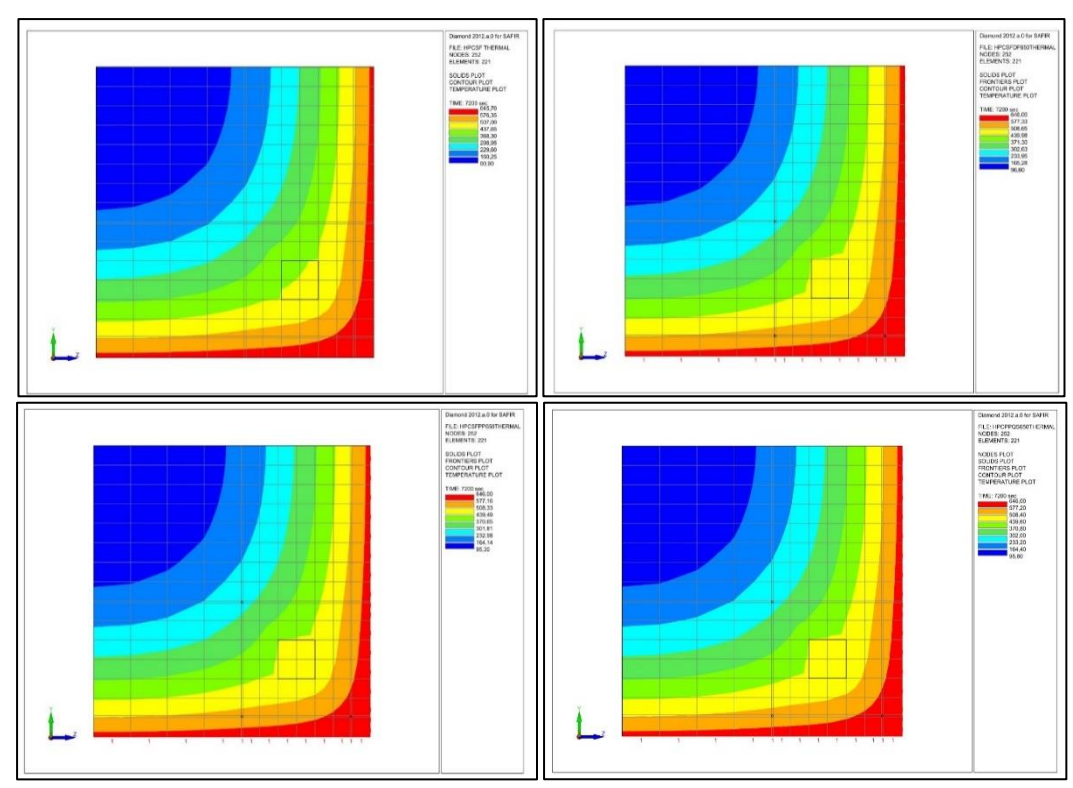


Figure IV.13: Evolution of temperature distribution during heating phase

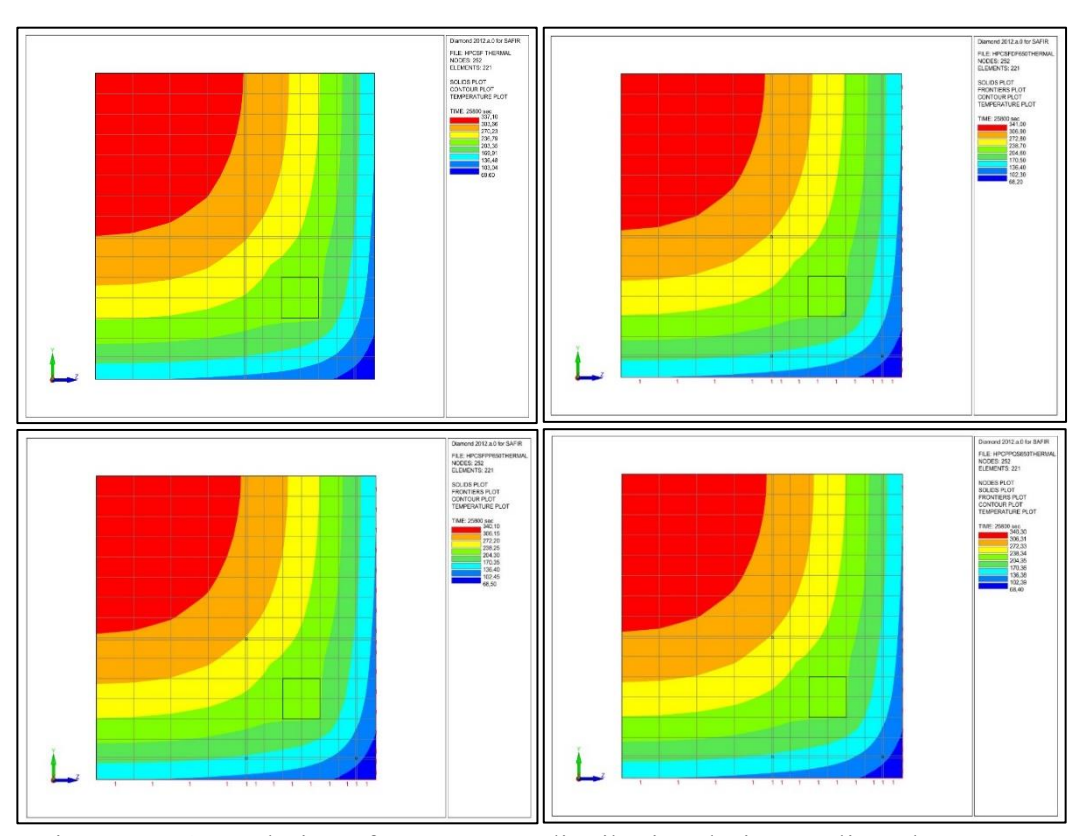


Figure IV.14: Evolution of temperature distribution during cooling phase

Table IV.6: Temperatures at selected points in the column section.

			Max T (°	°C) after 60 m	in (End of wa	rm-up phase)	Max T (° phase)	C)after 120 n	nin (End of sta	abilization	Max T (°C) after 940	min (End of c	ooling phase)
			HPC	HPCPP	HPCDP	HPCPPQS	HPC	НРСРР	HPCDP	HPCPPQS	HPC	НРСРР	HPCDP	HPCPPQS
	14	CORNER	186.7	188.0	187.6	188.1	228.0	228.7	228.6	228.8	29.1	28.5	28.3	28.5
	79	bars	80.4	82.1	82.8	82.3	150.3	152.5	153.3	152.7	33.4	32.5	32.2	32.5
205	126	Exposed face	137.0	138.3	138.7	138.4	192.0	193.4	193.9	193.5	32	31.2	30.9	31.2
V	239	Centre- section	22.2	22.6	22.8	22.7	51.1	54.1	55.1	54.3	39.6	38.3	37.8	38.3
arni	27	FIBER IN CORNER	-	147.5	146.1	147.6	2	210.1	209.4	210.2	-	29.7	49.4	29.7
ıemperatures	20	FIBER IN FACE	15	110.4	109.7	110.5	2	174.7	174.2	174.8	850	31.9	31.6	31.9
ָ ע	118	FIBER IN CENTER	-	49.9	50.5	50.0		107.2	108.0	168.8	121	34.8	34.4	34.8

			Max T (°C) after 60 m	nin (End of wa	arm-up phase)	Max T phase)	(°C)after 120	0 min (End o	of stabilization	Max T (°C) after 940	min (End of c	cooling phase
			HPC	HPCPP	HPCDP	HPCPPQS	HPC	HPCPP	HPCDP	HPCPPQS	HPC	НРСРР	HPCDP	HPCPPQS
	14	CORNER	395.4	397.4	398.0	397.4	438.3	438.8	439.0	438.8	35.5	34.5	34.2	34.5
	79	bars	128.9	132.1	133.2	132.1	295.0	299.4	300.9	299.4	45	43.4	42.9	43.4
	126	Exposed face	291.8	294.9	295.9	294.9	392.9	394.8	395.5	394.8	41.7	40.3	39.9	40.3
	239	Centre- section	24.2	25.1	25.4	25.1	73.1	77.4	78.9	77.4	58.7	56.2	55.4	56.2
iemperara:	27	FIBER IN CORNER	-	308.5	309.7	308.5	9-	410.3	410.8	410.3	×	37.1	36.7	37.1
	20	FIBER IN	858	215.1	216.3	215.1	in the second	352.7	353.8	352.7	8	42	41.5	42
	118	FIBER IN CENTER	120	72.6	73.4	72.6	- E	193.9	195.8	193.9	9	48.5	47.9	48.5

			Max T (°	'C) after 60 m	in (End of wa	arm-up phase)	Max T phase)	(°C)after 120	0 min (End o	of stabilization	Max T (°C) after 940	min (End of c	ooling phase)
			HPC	HPCPP	HPCDP	HPCPPQS	HPC	HPCPP	HPCDP	HPCPPQS	HPC	HPCPP	HPCDP	HPCPPQS
	14	CORNER	623.2	624.5	624.8	624.6	645.7	646.0	646.0	646.0	52	50.4	49.9	50.4
	79	bars	197.7	203.4	205.3	203.8	566.9	444.1	446.1	444.5	79.1	76.3	75.3	76.3
2,049	126	Exposed face	512.6	516.4	517.7	516.7	608.3	609.8	610.3	609.9	68.9	66.5	95.4	66.5
	239	Centre- section	26.2	27.4	27.8	27.5	90.9	95.3	96.6	95.6	120.3	115.2	113.5	115.2
iemperatures	27	FIBER IN CORNER		493.3	494.7	493.7	-	612.2	612.6	612.3	5	57.8	57.2	57.8
	20	FIBER IN	121	358.6	360.5	359.1	8	537.8	538.9	538.1	¥	71.5	70.7	71.5
ָּטְ	118	FIBER IN CENTER	220	93.6	94.6	93.8	-	285.4	288.2	286.1	-8	91.5	90.2	91.5

IV.3.3.2 Simulation process

The material model used in the simulation must accurately replicate the behavior of the structure under combined thermal and mechanical loading. The response of the structure is highly dependent on the load path. meaning that deformations can vary significantly. sometimes even taking on opposite signs for the same combination of stress and temperature. Axial thermal expansion is notably influenced by mechanical stress during the heating phase. which can be interpreted as a dependence of thermal deformation on the path taken within the stress-temperature space. Thus, thermal deformation is no longer viewed simply as a function of temperature but also as reliant on the stress state applied during heating. The selected models are expected to replicate this phenomenology by introducing transient creep deformation, either implicitly or explicitly.

All simulations were conducted using the SAFIR software. utilizing the current thermal and mechanical models of EN 1992-1-2 [1] and EN 1994-1-2 [2]. The temperature distribution across the different column sections is obtained through a nonlinear transient 2D analysis. Each column under study is initially subjected to a constant load, and then the column section is exposed to natural fire, encompassing all three phases (heating, cooling) to evaluate the residual characteristics of the columns. The load is applied in a decreasing, monotonic manner, and the failure time is calculated for each load level. This process continues until no further failure occurs, with the final load level representing the column's load-bearing capacity under natural fire conditions.

Figure IV.15 illustrates the simulation principle applied to columns exposed to natural fire. For instance, a load of 1000 kN is applied to the column, followed by natural fire exposure with a heating phase lasting 60 minutes. The compartment temperature returns to ambient 440 minutes from the start of the fire, with cooling observed until the section temperature stabilizes at ambient levels.

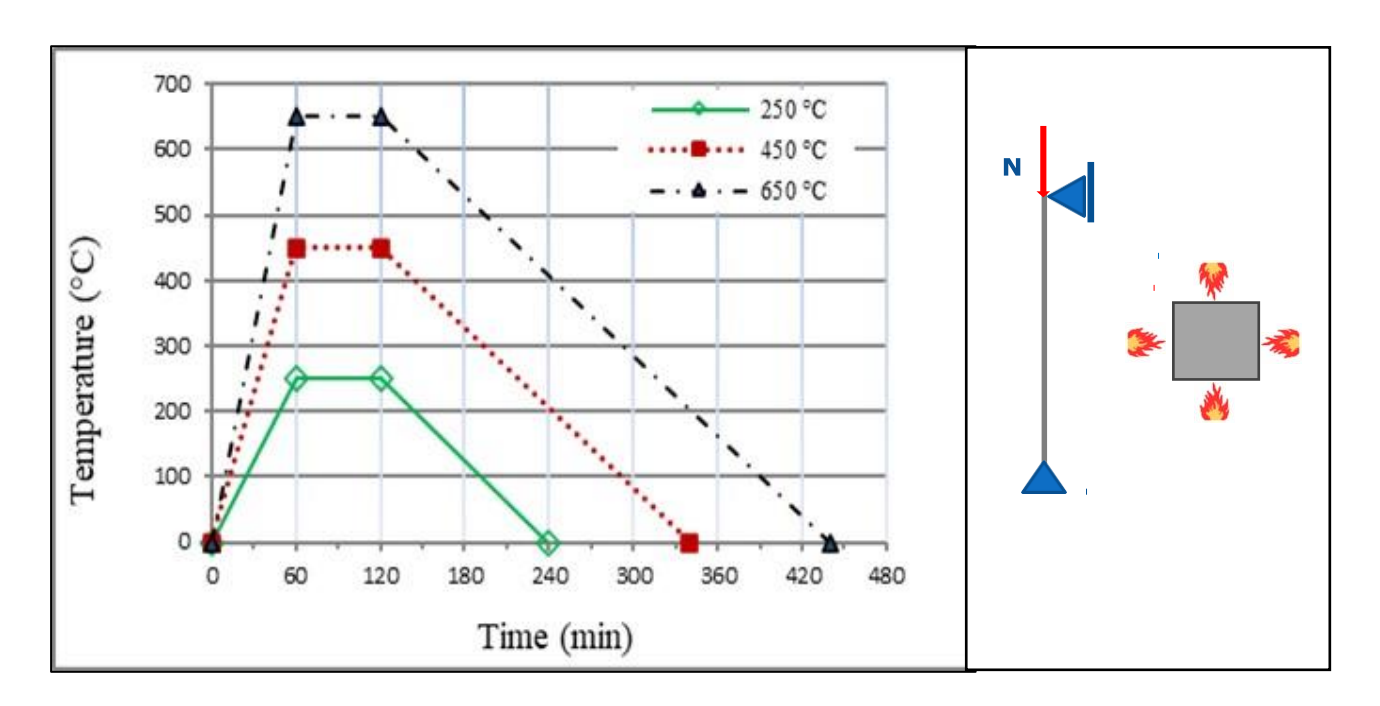


Figure IV.15: Evolution of the load and applied temperature.

IV.3.4 Parametric analysis for evaluating vertical load-bearing capacity (N_r)

IV.3.4.1 Evolution of (N_r) as a function of temperature

Figure IV.16 summarizes the analytical processes applied to the reference column (a column with a cross-section of 30 cm x 30 cm and a height of 3 m) exposed to natural fire at varying maximum temperatures (250°C. 450°C. and 650°C). Starting from its initial load-bearing capacity at time t=0. N20 (cold capacity). the load was gradually reduced. and multiple simulations were conducted to calculate the fire resistance time. Based on the determined resistance time. failure could be tracked through the different fire phases. This relationship between the applied load and fire resistance time illustrates the evolution of the column's load-bearing capacity. As observed, the load-bearing capacity continues to decrease even after the compartment's gas temperature reaches its peak. The load indicating the residual load-bearing capacity of the column, denoted as Nr. corresponds to the load value beyond which no failure is observed, indicated by a horizontal asymptote on the curve. In Figure IV.16(b), the residual load value is identified from the horizontal asymptote shown in Figure IV.16(a). The load ratio Nr/N20 is evaluated for each fire scenario once the temperatures in the column section return to ambient levels. The values on the horizontal axis represent the maximum gas temperature for each fire scenario.

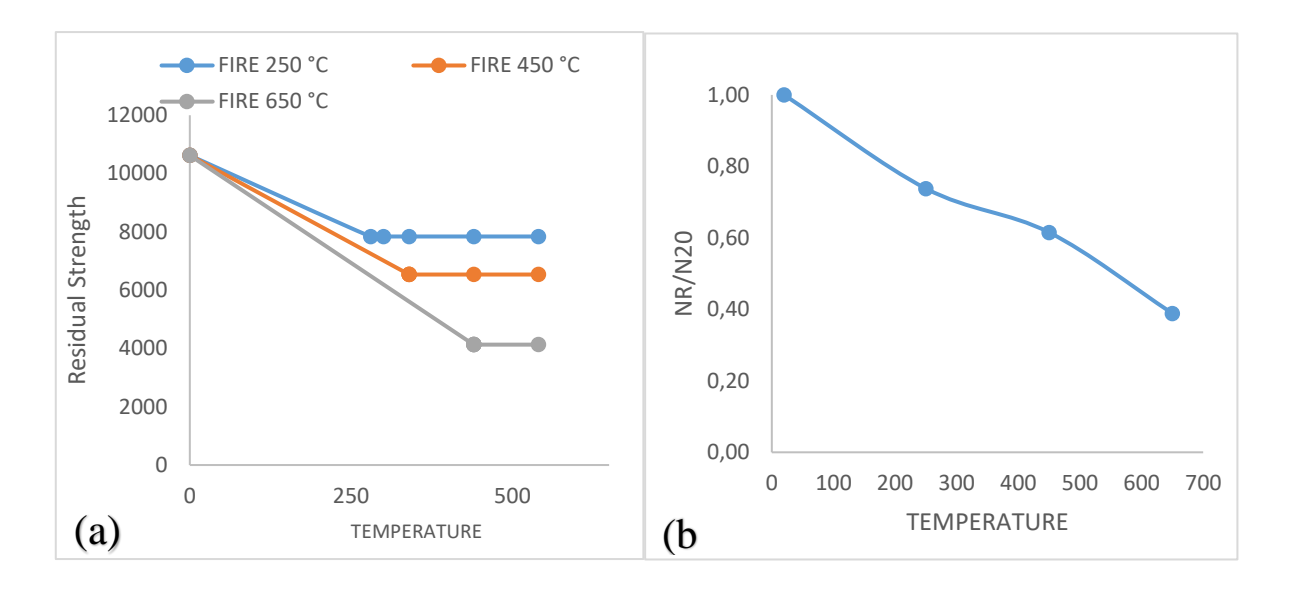


Figure IV.16: Evolution (N_r) of the column as a function of temperature.

IV.3.4.2 Influence of the effective height of the column on (N r)

The influence of column height on the residual strength (Nr) was analyzed for columns with heights of 3 m. 4 m. and 5 m. maintaining a constant cross-section of 30x30 cm². The results are presented in Table IV.7 and Figure IV.207. which shows the ratio of the load-bearing capacity for columns of varying heights (Nh/NRef) relative to the reference column (NRef) for columns exposed to a natural fire with a maximum temperature of 650° C.

As shown in Table IV.4. the cold load-bearing capacity (N20) at ambient temperature decreased with increasing column height due to buckling effects. The load-bearing capacity of the 5 m column (N20 = 9436.88 kN) was reduced by 12% compared to the 3 m column (N20 = 10621.88 kN). Similarly. the 4 m column showed a 3% reduction. with a load-bearing capacity of N20 = 10336.88 kN. Figure IV.17 illustrates the influence of height-induced instability on the cold load-bearing capacity.

The residual load-bearing capacity (Nr) was also analyzed for columns exposed to fire scenarios at 250°C. 450°C. and 650°C. The results show that the residual strength decreases nonlinearly as column height increases. For instance, at 250°C, the residual strength (Nr/N20) was 74% for the 3 m column, 73% for the 4 m column, and 72% for the 5 m column. At 450°C, these values dropped to 62%, 60%, and 56%, respectively. At 650°C, the residual strengths were 39% for the 3 m column, 33% for the 4 m column, and 31% for the 5 m column.

The analyses confirm that increasing the height of columns significantly reduces their residual load-bearing capacity. primarily due to buckling effects. These findings highlight the importance of considering height and thermal exposure in the design of columns to maintain structural integrity during and after fire events.

Table IV.4: Evolution of the bearing capacity as a function of (H) and (T).

Н	3m		4m		5m	
Nr	N20(KN)	Nr/N20	N20(KN)	Nr/N20	N20(KN)	Nr/N20
N20	10621.88	1.00	10336.88	1.00	9436.88	1.00
N250	7840.00	0.74	7560.50	0.73	6780.50	0.72
N450	6535.00	0.62	6160.00	0.60	5315.00	0.56
N650	4130.00	0.39	3450.00	0.33	2885.00	0.31

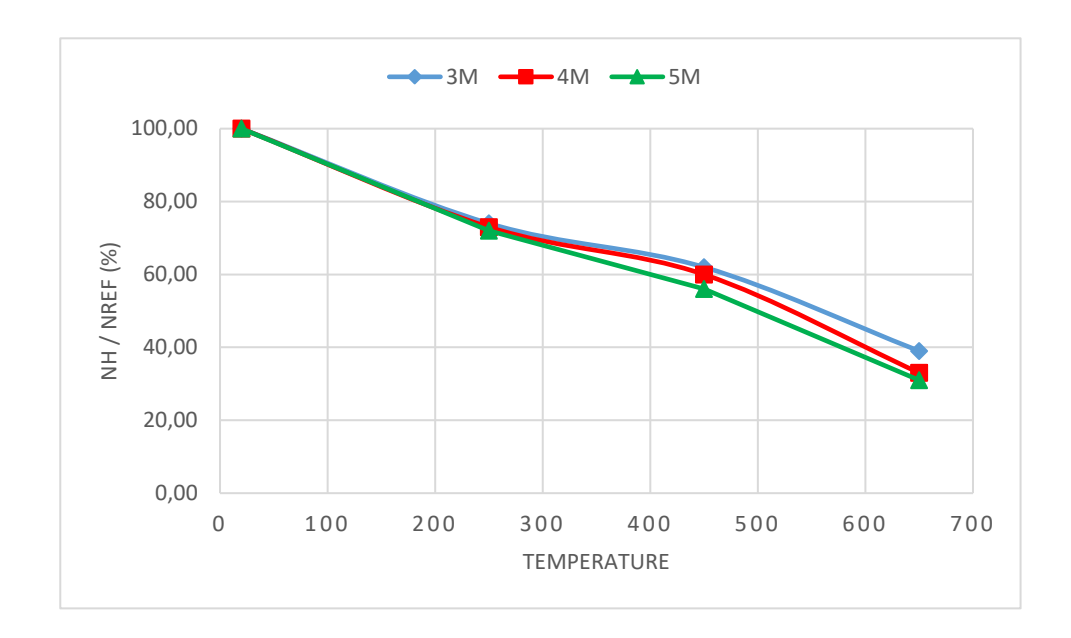


Figure IV.17: Influence of the variation in the height of the column on (N r).

IV.3.4.3 Influence of column section dimensions on (N r)

The influence of column section dimensions on the residual strength (Nr) was analyzed for columns with a height of 3.00 m. considering cross-sections of 30x30 cm² and 40x40 cm². exposed to fire scenarios with maximum temperatures of 250°C. 450°C. and 650°C. The results are presented in Table IV.5 and Figure IV.18.

As shown in Table IV.5. the evolution of the residual load-bearing capacity (Nr) for the 40x40 cm² column was consistently higher than that of the 30x30 cm² column. At 20°C. the load-bearing capacity increased by approximately 76% for the larger section. At 250°C. the residual strength (Nr/N20) was 74% and 76% for the 30x30 cm² and 40x40 cm² sections. respectively. Similarly, at 450°C. these values dropped to 62% and 65%. while at 650°C. they further decreased to 39% and 49%. highlighting the influence of section size on thermal performance.

Figure IV.18 (a) illustrates the evolution of the relative residual strength (Nr/N20) as a function of fire temperature. For the fire scenario at 250°C, the relative strength of the 30x30 cm² column was approximately 0.74 compared to 0.76 for the 40x40 cm² section. At 450°C, these values were 0.62 and 0.65, respectively, while at 650°C, they reduced to 0.39 and 0.49. These results indicate that increasing the section size improves the residual strength of the column, thereby enhancing its fire resistance.

Figure IV.18 (b) presents the residual strength ratio (Nr/N20) for both column sections across the range of temperatures. At 20°C. both sections retained 100% of their load-bearing capacity. As the temperature increased, the larger section consistently showed higher relative residual strength, retaining 49% of its initial capacity at 650°C compared to 39% for the smaller section. The analyses confirm that increasing the cross-sectional dimensions of a column significantly improves its residual strength under fire exposure. These findings emphasize the importance of section size in ensuring the structural integrity and post-fire serviceability of columns.

Table IV.5: Evolution of the bearing capacity as a function of the column section.

Н	30X30 cm ²		40X40 cm ²	
Nr	N20 (KN)	Nr/N20	N20 (KN)	Nr/N20
N20	10621.88	1.00	18751.88	1.00
N250	7840.00	0.74	14190.00	0.76
N450	6535.00	0.62	12125.00	0.65
N650	4130.00	0.39	9200.00	0.49

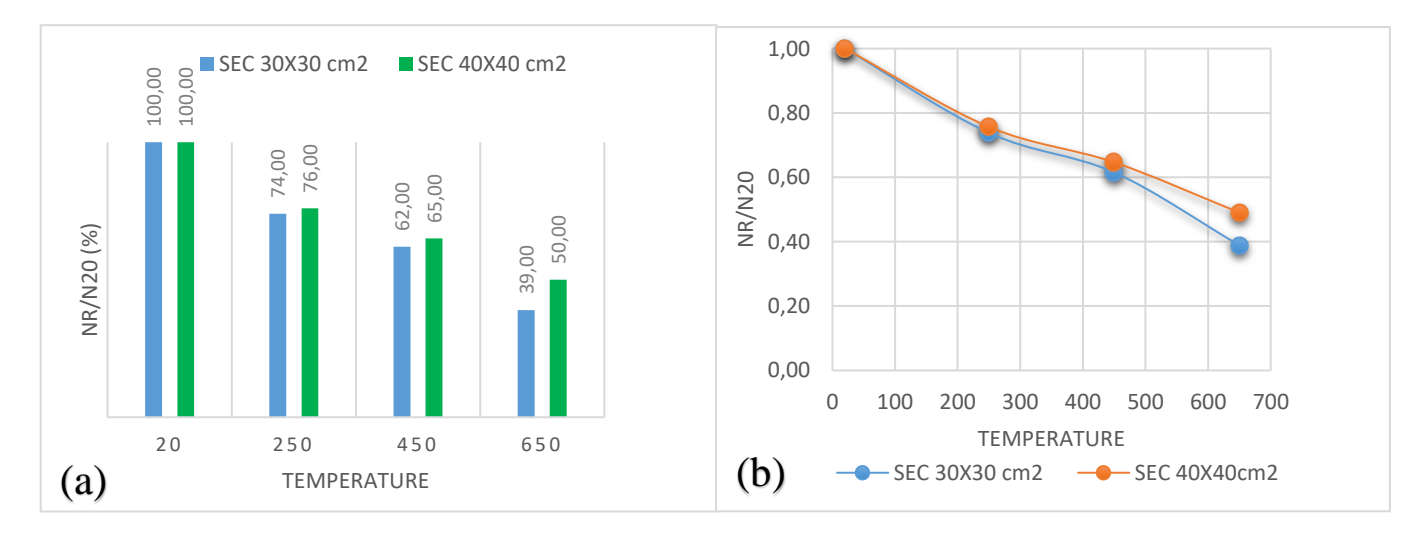


Figure IV.18: Evolution of (N r / N 20) as a function of section and temperature.

IV.3.4.4 Influence of support conditions on load-bearing capacity (N r)

The effect of support conditions on the residual strength of columns under elevated temperatures was analyzed using two configurations. with results summarized in Figure IV.19 and Table IV.6. In the first configuration, columns with double support at the base and single support at the top (SS-DS) exhibited a notable reduction in residual strength (Nr) as the temperature increased. At 20°C, the residual strength reached its maximum value (N20) but progressively declined to 74% at 250°C, 62% at 450°C, and 39% at 650°C. This trend confirms the substantial negative impact of high temperatures on the structural performance of columns. As summarized in Table IV.6, these results indicate that the columns become non-functional beyond 650°C under these support conditions.

In the second configuration, columns with triple support at the base and single support at the top (SS-TS) showed slightly higher residual strength compared to the first configuration, although the general decreasing trend with increasing temperature persisted. At 20°C, the residual strength was slightly higher, decreasing to 74% at 250°C, 62% at 450°C, and 41% at 650°C. These results, detailed in Table IV.6, highlight the influence of support conditions on the ability of columns to retain residual strength after thermal exposure.

As shown in Figure IV.19. the relationship between residual strength and temperature demonstrates that support conditions significantly affect the columns' load-bearing capacity under thermal stress. Nevertheless, regardless of the configuration, columns lose their structural functionality after prolonged exposure to temperatures beyond 650°C. This underscores the importance of considering thermal effects and support conditions in the structural design of columns subjected to fire scenarios.

Table IV.6: Evolution of the bearing capacity as a function of the support conditions.

	Double su	ipport and	Triple sup	port and
	single suppor	t	single suppo	ort
Nr	N20(KN)	Nr/N20	N20(KN)	Nr/N20
N20	10621.88	1.00	10833.75	1.00
N250	7840.00	0.74	8040.00	0.74
N450	6535.00	0.62	6725.00	0.62
N650	4130.00	0.39	4460.00	0.41

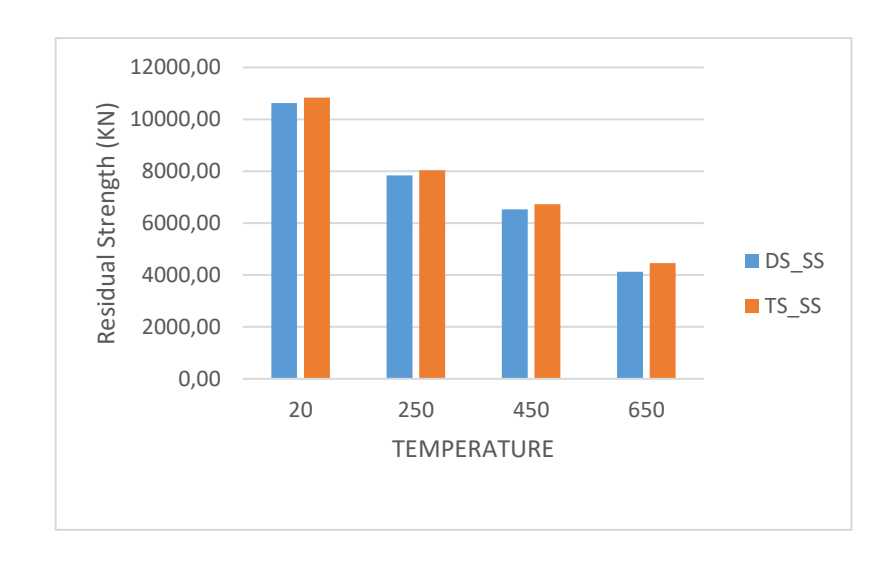


Figure IV.19: Evolution of the bearing capacity as a function of the support conditions.

IV.3.4.5 The influence of different concrete mix types on the residual strength (Nr)

The influence of different concrete mix types on the residual strength (Nr) was analyzed for columns exposed to elevated temperatures. Four types of high-performance concrete (HPC) mixes were evaluated:

- 1. HPC
- 2. HPC with polypropylene fibers (HPCPP).
- 3. HPC with date palm fibers (HPCDP).
- 4. HPC with polypropylene fibers based in quarry sand (HPCPPQS)

The results are presented in Table IV .7 and Figure IV.20. which show the residual load-bearing capacity (Nr) for each mix type at ambient temperature (20°C) and after exposure to fire scenarios at 250°C. 450°C. and 650°C.

At ambient temperature, the reference mix (HPC) demonstrated the highest load-bearing capacity (N20 = 10621.88 kN), followed by HPCPP (N20 = 9965.5 kN). HPCPPQS (N20 = 9543.84 kN), and HPCDP (N20 = 8791.87 kN). The incorporation of fibers, particularly date palm fibers, reduced the initial load-bearing capacity compared to the reference mix, while the addition of quarry sand in HPCPPQS resulted in a higher initial capacity compared to HPCDP but lower than HPC and HPCPP.

When exposed to elevated temperatures, the residual load-bearing capacity (Nr) was evaluated as a percentage of the cold load-bearing capacity (Nr/N20). At 250°C, the residual strength was 74% for HPC. 75% for HPCPP, 77% for HPCDP, and 71% for HPCPPQS. At 450°C, these values decreased to 62%, 61%, 71%, and 70%, respectively. At 650°C, the residual

strengths further declined to 39% for HPC. 39% for HPCPP. 57% for HPCDP. and 58% for HPCPPQS.

The results indicate that the addition of polypropylene fibers (HPCPP) had a marginal effect on residual strength compared to the reference mix (HPC). In contrast, the inclusion of date palm fibers (HPCDP) significantly enhanced the residual strength at higher temperatures, particularly at 650°C, where HPCDP retained 57% of its load-bearing capacity compared to 39% for HPC and HPCPP. The HPCPPQS mix, which combines polypropylene fibers with quarry sand, exhibited a similar trend to HPCDP at 650°C, retaining 58% of its load-bearing capacity. This suggests that quarry sand, when used in conjunction with polypropylene fibers, can also contribute to improved fire resistance, albeit to a slightly lesser extent than date palm fibers.

These findings highlight the importance of fiber type and composition. as well as the role of quarry sand, in enhancing the fire resistance of high-performance concrete. Date palm fibers, in particular, demonstrate significant potential for improving structural integrity under fire conditions, while the HPCPPQS mix offers a viable alternative for applications requiring enhanced fire resistance.

Table IV.7: Influence of different concrete mix types on the residual strength.

	HPC		НРСРР		HPCDP		HPCPPQS	
	N20(KN)	Nr/N20	N20 (KN)	Nr/N20	N20(KN)	Nr/N20	N20 (KN)	Nr/N20
N20	10621.88	1.00	9965.5	1.00	8791.87	1.00	9543.84	1.00
N250	7840	0.74	7448	0.75	6750	0.77	6789.16	0.71
N450	6535	0.62	6115	0.61	6227	0.71	6695.67	0.70
N650	4130	0.39	3840	0.39	5040	0.57	5580.47	0.58

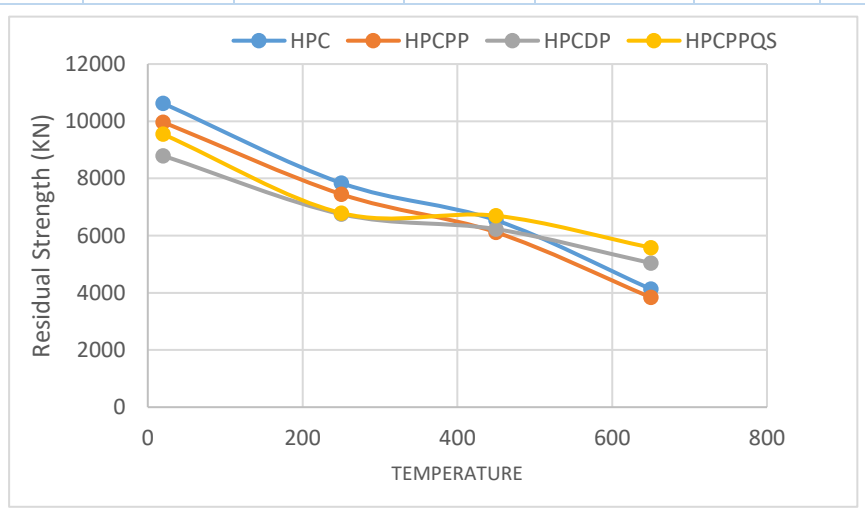


Figure IV.20: Bearing capacity evolution across different concrete mixes.

IV.4 Conclusion

This chapter investigate the behavior of reinforced concrete columns under natural fire conditions. focusing on residual strength and load-bearing capacity during heating and cooling phases. Key findings reveal that fire duration and thermal exposure significantly reduce residual strength. particularly in larger sections, while column geometry and support conditions influence stability. Concrete mix composition plays a critical role, with date palm fibers (HPCDP) demonstrating superior fire resistance, retaining 57% of capacity at 650°C compared to 39% for HPC and HPCPP. The mix incorporating polypropylene fibers and quarry sand (HPCPPQS) also performed well, retaining 58% of its capacity at 650°C, highlighting the potential of quarry sand in enhancing fire resistance. Steel reinforcement recovers strength upon cooling, while concrete experiences irreversible damage, exacerbated by thermal shock. Numerical modeling using SAFIR software effectively simulated column behavior, providing insights into degradation and recovery. These findings emphasize the importance of holistic fire-resistant design, incorporating innovative materials and realistic fire scenarios. Future research should explore advanced materials and refined modeling techniques to further optimize structural fire performance.

General conclusion

This research offers a comprehensive understanding of how concrete, particularly high-performance concrete (HPC), behaves under high-temperature conditions and its implications for the structural integrity of reinforced concrete (RC) columns. The study reveals the complex interactions between physical, chemical, and mechanical processes that drive concrete degradation when exposed to thermal stress. Factors such as heating and cooling cycles, material composition, and structural geometry play a significant role in shaping the thermal and mechanical responses of concrete. The presence of water, in both liquid and vapor forms, further complicates these interactions, leading to issues like mass loss, microcracking, and spalling.

When exposed to high temperatures, concrete undergoes a combination of physical processes (e.g., heat transfer, water evaporation), chemical reactions (e.g., dehydration, carbonation), and mechanical changes (e.g., deformations, microcracking), all of which contribute to its degradation. The residual mechanical properties of concrete after such exposure vary widely, with heating and cooling regimes being critical determinants. While steel reinforcement can partially or fully recover its strength and stiffness after cooling, concrete experiences irreversible damage. Rapid cooling, or thermal shock, can cause up to 33% additional strength loss compared to gradual cooling.

The choice of materials, including cement, silica fume, quarry sand, and reinforcing fibers like polypropylene and date palm, significantly influences the performance of HPC. Silica fume, for instance, enhances the density and compressive strength of the concrete matrix, while fibers such as polypropylene and date palm improve crack resistance and energy absorption. However, the addition of fibers generally reduces workability, with date palm fibers having a more noticeable impact on viscosity compared to polypropylene. Quarry sand helps maintain the compactness and stability of the concrete structure, even when fibers are present.

Palm fiber-reinforced HPC showed a 65% reduction in compressive strength after three hours of high-temperature exposure, a performance comparable to polypropylene-based concrete. This highlights the potential of palm fibers as a sustainable alternative. The flexural strength of palm fiber concrete was only slightly lower (55% reduction) than that of polypropylene-based concrete, thanks to the fibers' ductile nature, which enhances flexibility and crack resistance. Minimal mass loss was observed in palm fiber concrete between 250°C and 450°C,

as the fibers only melt at extremely high temperatures. Additionally, palm fibers improved the permeability and spalling resistance of HPC by absorbing water pressure and allowing vapor to escape, thereby preserving the concrete's strength.

The duration of heating and cooling significantly affects the residual load-bearing capacity of RC columns. Prolonged exposure to high temperatures leads to substantial strength reduction, which continues during the cooling phase. Taller columns are more susceptible to buckling, reducing their residual load-bearing capacity. Larger cross-sectional dimensions, however, enhance residual strength, underscoring the importance of section size in maintaining structural integrity. Support conditions also play a critical role, with fixed supports generally improving load-bearing capacity compared to pinned supports. Nevertheless, all configurations lose functionality at temperatures above 650°C. Date palm fiber-reinforced HPC (HPCDP) outperformed other mixes, retaining 57% of its load-bearing capacity at 650°C, compared to 39% for polypropylene fiber-reinforced HPC (HPCPP). Numerical modeling using SAFIR software effectively simulated the behavior of RC columns under fire conditions, providing valuable insights into the time-dependent degradation and recovery of structural capacity.

These findings emphasize the need for a holistic approach to fire safety design, incorporating realistic fire scenarios, advanced modeling techniques, and innovative materials. Future research should focus on developing advanced analytical models that account for factors like biaxial bending, multi-side fire exposure, spalling, and creep to better simulate real-world conditions. Further exploration of sustainable materials like date palm fibers and other eco-friendly additives is essential to enhance the fire resistance and overall performance of HPC. Comprehensive experimental studies and parametric analyses are also needed to validate advanced models and establish reliable design guidelines. Structural assessments must consider the cooling phase of fires, as it significantly impacts residual strength and load-bearing capacity. Adopting a performance-based approach to fire safety design will enable the development of cost-effective and innovative solutions for evaluating residual load-bearing capacity and seismic performance after a fire.

Referances

- [1] Stefano D. P., « Lien entre la perméabilité et l'endommagement dans les bétons à haute température », thèse de doctorat, Ecole Nationale des Ponts et Chaussées, 2004.
- [2] Kanema M. T., « Influence des paramètres de formulation sur le comportement à haute température des bétons », thèse de doctorat, Université de Cergy-Pontoise, 2007.
- [3] Mindeguia J. C., « Contribution expérimentale a la compréhension des risques d'instabilité thermique des bétons », thèse de doctorat, Université de Pau et des Pays de l'Adour, 2009.
- [4] Baroghel-Bouny V., « Caractérisation des pâtes de ciment et des bétons-Méthode, analyse, interprétations », publié par Laboratoire Central des Ponts et Chaussées et Ministère de l'Equipement, des Transports et du Tourisme, 1994.
- [5] Guillon. E., « Durabilité des matériaux cimentaires Modélisation de l'influence des équilibres physico-chimiques sur la microstructure et les propriétés mécaniques résiduelles », ENS de Cachan.
- [6] Baroghel Bouny V., « Caractérisation microstructurale et hydrique des pâtes de ciment et des bétons ordinaires et à très hautes performances », thèse de doctorat, Ecole Nationale des Ponts et Chaussées, 1994.
- [7] Ruiz A. L., « Analyse de l'évolution de la microstructure de la pâte de ciment sous chargements thermiques », Thèse de doctorat, Ecole Nationale des Ponts et de Chaussées, 2003. [8] Sabeur H., « Etude du comportement du béton a hautes températures, une nouvelle approche
- [8] Sabeur H., « Etude du comportement du beton à hautes temperatures, une nouvelle approche thermo-hygro-mécanique couplée pour la modélisation du fluage thermique transitoire », thèse de doctorat, Université De Marne La Vallée, 2006.
- [9] Regourd, M. (1982). Le béton hydraulique, chapitre l'eaul. Presse de l'Ecole Nationale des Ponts et Chaussées. pp. 59-68
- [10] Nguyen, VT. (2013). Comportement Des Bétons Ordinaire et à Hautes Performances Soumis à Haute Température : Application à Des éprouvettes de Grandes Dimensions Thèse de doctorat, Université de Cergy Pontoise. France.
- [11] Diamond, S. (1986). The microstructure of cement paste in concrete. In proceeding of the 8th international on the chemistry of cement, Rio de Janeiro, Brazil, Vol. 1, pp. 122-147. [12] Aïtcin, P. C., Carles-Gilbergues, A. (1999). Mesure de la perméabilité aux gaz des bétons : perméabilité apparente et perméabilité intrinsèque. Partie II étude de l'influence de la taille des éprouvettes et de la variabilité des résultats dans le cas d'un BHPI. Bulletin des Laboratoires des Ponts et Chaussées, Vol 221, pp. 79-87.
- [13] Mouret, M., Bascoul, A., Escadeillas, G. (1999). Microstructural features of concrete in relation to initial temperature SEM and ESEM characterization. Cement and Concrete Research, Vol. 29, pp. 369-375.
- [14] Diamond, S. (2004). —The microstructure of cement paste and concrete-a visual primer. Cement and Concrete Composites, Vol. 26, pp. 919-933
- [15] Metha, P. K. (1986). Concrete structure, properties, and materials. Englewood cliff, New Jersey: Prentice-Hall.
- [16] Noumowé, A. (1995). Effet de hautes températures (20°C-600°C) sur le béton. Cas particulier du BHP". Thèse de Doctorat de l'INSA de Lyon.
- [17] Kalifa, P and Tsimbrovska, M. (1998). Comportement des BHP à hautes températures :État de la question et résultats expérimentaux". Cahier de CSTB N° 3078, Vol. 394
- [18] IREX. (2005) Synthèse des travaux du Projet National BHP 2000 sur les bétons à hautes performances". Presses de l'Ecole Nationale des Ponts et Chaussées, 298 pages.
- [19] Khoury, G.A., Grainger, B.N, and Sullivan, Patrick J. E. (1985b) __Strain of concrete during first heating to 600°C under load ". Magazine of concrete research. Vol. 37, pp195-215.

- [20] Li,Y.-H., and Franssen, J.-M. (2011). Test Results and Model for the Residual Compressive Strength of Concrete After a Fire ". Journal of Structural Fire Engineering, Vol. 2 No. 1, pp. 29-44.
- [21] Schneider, U. (1985). Properties of materials at high temperatures: concrete ". Kassel, Germany: RILEM
- [22] Hager, I. Gaweska. (2004). __Comportement à haute température des bétons à haute performance-évolution des principales propriétés mécaniques. Thèse de doctorat, Ecole Nationale des Ponts et Chaussées et Ecole Polytechnique de Croatie.
- [23] Thelandersson, S. (1972). Effect of High Temperatures on Tensile Strength of Concrete ". (Bulletines of Division of Structural Mechanics and Concrete Construction, Bulletin 26; Vol. Bulletin 26). Lund Institute of Technology.
- [24] TC44-PHT. (1985) RILEM Technical Committees 44-PHT Behaviour of Concrete at high temperature ". Technical Report Ed. by, U. Schneider, Dept. of Civil Engineering. Germany: 122 pages.
- [25] Xu Y, Wong, Y.L., Poon, C.S. and Anson, M., (2003). Influence of PFA on cracking of concrete and cement paste after exposure to high temperatures ". Cement and Concrete Research, 33, pp. 2009-2016.
- [26] Felicetti R., Gambarova, P.G, Sora, MP.N., KHOURY, G.A. (1995) __Mechanical Behaviour of HPC and UHPC in Direct Tension at High Temperature and After Cooling ".
- [27] Schneider U. (1988) Concrete at high temperatures: A general review ". Fire safety Journal, vol 13, pp 55-68.
- [28] Harada T, Takeda J., Yamane S. and Furumura F. (1972). Strength, elasticity and thermal properties of concrete subjected to elevated temperatures ". In International Seminar on Concrete for Nuclear reactors. ACI Special Publication, paper SP34, pp 377-406.
- [29] Heinfling, G. (1998) Contribution à la modélisation numérique du comportement du béton et des structures en béton armé sous sollicitations thermo-mécaniques à hautes températures". Thèse de l'Institut National des Sciences Appliquées de Lyon et Univ. Lyon I, p227.
- [30] Felecitti, R. and Gambarova, P.G. (1999) On the residual proprieties of high-performance siliceous concrete exposed to high temperatures. Mechanics of Quasi-Brittle materials and structures ". Edited by G. Pijaudier-Cabot, Zdenek Bittnar & Bruno Gérard. Paris: Hermes, pp 167-186.
- [31] Menou, A. (2004). Etude du comportement thermomécanique des bétons à haute température : approche multi échelles de l'endommagement thermique. Thèse de doctorat, Université de Pau et des Pays de l'Adour, France
- [32] Farage, M.C.R., Sercombe, J. G., Gallé, C. (2003) Rehydration and microstructure of cement paste after heating at temperatures up to 300 °C. Cement and Concrete Research, Vol. 33, pp 1047-1056.
- [33] Luccioni, B.M., Figueroa, M.I. and Danesi, R.F. (2003). Thermo-mechanic model for concrete exposed to elevated temperatures ". Engineering Structures, vol 25 Issue 6, pp729-742.
- [34] Maréchal, J.C. (1970). Variations in the modulus of elasticity and Poisson's ratio with temperature ". In: ACI. Int. Seminar on Concrete for Nuclear Reactors, (CNR). Berlin.
- [35] Gernay, T. (2012). A multiaxial constitutive model for concrete in the fire situation including transient creep and cooling down phases ". Thèse de Doctorat : Université de liège, Belgique, 269 pages.
- [36] Anderberg, Y. and Thelandersson, S. (1976). Stress and deformation characteristics of concrete at elevated temperatures ". Part II: Experimental investigation and material behaviour model. Bulletin 54. Lund Institute of Technology, Lund.

- [37] Chang, Y.F., Chen Y.H., Sheu, M.S. and Yao G.C. (2006). __Residual stress-strain relationship for concrete after exposure to high temperatures. Cement and Concrete Research 36, pp. 1999–2005.
- [38] Guergah, C., Dimia, M. S., & Guenfoud, M. (2018). Contribution to the numerical modelling of the spalling phenomenon: case of a reinforced concrete beams. Arabian Journal for Science and Engineering, 43, 1747-1759.
- [39] Cherif, G., Salah, D. M., & Abdelaziz, B. (2021). Numerical modelling of one-way reinforced concrete slab in fire taking into account of spalling. Civil Engineering Journal, 7(3), 477-487.
- [40] Abrams M.S. (1971). Compressive stength of concrete at temperature to 1600F, temperature and concrete. ACI SP-25, American Concrete Institute, Detroit, pp 33-58.
- [41] Corsi, F. (2005). Damage to concrete in tunnels after fire exposure Evaluation report Milestone 4.3UPTUNII (Upgrading of existing tunnels report xxx Work Package 4 Project N° GRD1-2001-40739) ENEA, Italy.
- [42] Lee, J., Xi, Y and Willam, K. (2008). Properties of Concrete after High Temperature Heating and Cooling. ACI Materials Journal, vol 105 issue 4, pp 334–341.
- [43] Kodur V. Spalling in high strength concrete exposed to fire: concerns, causes, critical parameters and cures. Adv Technol Struct Eng 2000:1–9.
- [44] Hertz KD. Limits of spalling of fire-exposed concrete. Fire Saf J 2003;38(2):103–16.
- [45] Aldea C-M, Franssen J-M, Dotreppe J-C. Fire test on normal and high-strength reinforced concrete columns. NIST Spec Publ 1997; 919:109–24.
- [46] Ali FA, O'Connor D, Abu-Tair A. Explosive spalling of high-strength concrete columns in fire. Mag Concr Res 2001;53(3):197–204.
- [47] Kodur V, Mcgrath R. Fire endurance of high strength concrete columns. Fire Technol 2003; 39:73–87.
- [48] Ali F, Nadjai A, Silcock G, Abu-Tair A. Outcomes of a major research on fire resistance of concrete columns. Fire Saf J 2004;39(6):433–45.
- [49] Kodur VKR, Cheng F-P, Wang T-C, Sultan MA. Effect of strength and fiber reinforcement on fire resistance of high-strength concrete columns. J Struct Eng 2003;129(2):253–9.
- [50] Khaliq W, Kodur V. Effectiveness of polypropylene and steel fibers in enhancing fire resistance of high-strength concrete columns. J Struct Eng 2018;144(3): 04017224. https://doi.org/10.1061/(ASCE)ST.1943-541X.0001981.
- [51] Benmarce, A. and M. Guenfoud (2005). "Experimental behavior of high strength concrete columns in fire." Magazine of Concrete Research 57(5): 283-287.
- [52] Franssen, J. M. and J. C. Dotreppe (2003). "Fire tests and calculation methods for circular concrete columns." Fire Technology 39: 80-97.
- [53] EC2-1-2 (2004). Design of concrete structures Part 1-2, General rules Structural Fire design, CEN.
- [54] T. Gernay and M. S. Dimia, "Structural Behavior of Concrete Columns Under Natural Fires Including Cooling Down Phase," in International Conference on Recent Advances in Nonlinear Models Structural Concrete Applications, 2011, pp. 1-20.
- [55] ACI-318 (2008). Building Code Requirements for Reinforced Concrete and Commentary. Farmington Hills, MI, American Concrete Institute.
- [56] ACI-216.1 (2007). Code requirements for determining fire resistance of concrete and masonry construction assemblies. Farmington Hills, MI, American Concrete Institute.
- [57] ASTM-E119 (2007). Standard test methods for fire tests of building construction and materials. West Conshohocken, PA, American Society for Testing and Materials.

- [58] V. R. Kodur and F. P. Cheng, "Effect of Strength and Fiber Reinforcement on the Fire Resistance of High Strength Concrete Columns," ASCE Journal of Structural Engineering,pp. 253-259, 2003.
- [59] AS-3600 (2001). Concrete Structures. Australia, Committee BD-002.
- [60] Lie TT, and Woollerton J L (1998) Fire resistance of reinforced-concrete columns: Test results.Internal Rep. No. 569, National Research Council of Canada, Quebec, Canada.
- [61] Guergah, C., Dimia, M. S., & Samp; Guenfoud, M. (2016). Numerical Investigations of spalling behaviour of reinforced concrete beams Subjected to HC Fire. Academic Journal of Civil Engineering, 34(1), 1015-1022.
- [62] BAGHDADI, M., DIMIA, M. S., GUERGAH, C., RABEHI, R., & ELAKHDAR, A. R. (2025). Experimental and Numerical Investigation on the Behavior and Strengthening of Fire-Damaged Reinforced Concrete Walls Using Self-Compacting Concrete Jacketing. Materials Science.
- [63] BAGHDADI, M., DIMIA, M. S., GUERGAH, C., RABEHI, R., & ELAKHDAR, A. R. (2025). Experimental and Numerical Investigation on the Behavior and Strengthening of Fire-Damaged Reinforced Concrete Walls Using Self-Compacting Concrete Jacketing. Materials Science.
- [64] Gherabli, S., Dimia, M. S., & Dimia, M. S
- [65]GUERGAH, C. (2018). Contribution à l'étude au feu des éléments en béton armé-Prise en compte de l'écaillage du béton (Doctoral dissertation).

- [1] EN 197-1 2012 « Composition, Specifications and Conformity Criteria for Common Cements ». AFNOR, La Plaine Saint-Denis, France (in French), Cement Part 1, 2012.
- [2] NA 442 2005 « Ciment, composition, spécifications et critères de conformité des ciments courants », 2005
- [3] NF EN 13263-1 2009 « Fumée de silice pour béton Partie 1 : définitions, exigences et critères de conformité », 2009.
- [4] XP P18-545 2008 « Granulats : éléments de définition, conformité et codification », 2008.
- [5] NF EN 933-1 1997 « Essais pour déterminer les caractéristiques géométriques des granulats Partie 1 : détermination de la granularité. Analyse granulométrique par tamisage », AFNOR, 1997.
- [6] Kalifa P., Chene G., Galle C., «High-temperature behaviour of HPC with polypropylene fibres from spalling to microstructure », Cement and Concrete Research, p. 1487–1499, 2001.
- [7] Kriker, A., Bali, A., Debicki, G., Bouziane, M., & Chabannet, M. (2008). Durability of date palm fibres and their use as reinforcement in hot dry climates. Cement and Concrete Composites, 30(7), 639-648. https://doi.org/10.1016/j.cemconcomp.2007.11.006
- [8] Aïctin P.C., « Bétons a Haute Performance », Editions Eyrolles, 2001.
- [9] NF EN 12390-1 2001 « Essai pour béton durci, Partie 1: Forme, dimensions et autres exigences relatives aux éprouvettes et aux Moules, Indice de classement P 18-430 », AFNOR, 2001.
- [10] NF EN 12390-2 2001 « Essai pour béton durci, Partie 2 : Confection et conservation des éprouvettes pour essais de résistance, Indice de classement P 18-438 », AFNOR, 2001.
- [11] NF EN 12350-2 1999 « Essai pour béton frais. Partie 2 : Essai d'affaissement », AFNOR, 1999.

- [12] NF EN 12350-6 2012 « Essai pour béton frais Partie 6 : masse volumique », 2012.
- [13] NF EN 12350-7 2012 « Essais pour béton frais Partie 7 : teneur en air Méthode de la compressibilité », 2012.

- [1] Pliya P., Beaucour A-L., Noumowé A., « Contribution of cocktail of polypropylene and steel fibres in improving the behaviour of high strength concrete subjected to high temperature », Construction and Building Materials, vol. 25, p. 1926–1934, 2011.
- [2] Xiao H., Falkner, « On residual strength of high-performance concrete with and without polypropylene fibres at elevated temperatures », Fire Safety Journal, vol. 41, p. 115–121,2006.
- [3] NF EN 12390-3 2012 « Essais pour béton durci Partie 3 : résistance à la compression des éprouvettes », 2012.
- [4] Li, Y., & D. (2021). Effect of lateral restraint and inclusion of polypropylene and steel fibers on spalling behavior, pore pressure, and thermal stress in ultra-high-performance concrete (UHPC) at elevated temperature. Construction and Building Materials, 271, 121879. https://doi.org/10.1016/j.conbuildmat.2020.121879
- [5] Chan, S. Y., Peng, G. F., & Samp; Chan, J. K. (1996). Comparison between high strength concrete and normal strength concrete subjected to high temperature. Materials and Structures, 29, 616-619. https://doi.org/10.1007/BF02485969
- [6]. Hamda, M., Guergah, C., & Benmarce, A. (2023) Cherif, G., Mohamed, B., Salah, D. M., de Oliveira Siqueira, A. M., & Campos, J. C. C. (2024). Assessing Delayed Collapse Risks in Load-Bearing Reinforced Concrete Walls Exposed to Parametric Fires: A Numerical Investigation. The Journal of Engineering and Exact Sciences, 10(8), 19442-19442.
- [7]. Al-Ameri, R. A., Abid, S. R., Murali, G., Ali, S.H., & Dzakça, M. (2021). Residual repeated impact strength of concrete exposed to elevated temperatures. Crystals, 11(8), 941. https://doi.org/10.3390/cryst11080941
- [8] EC2, Eurocode 2. (2004), EN 1992-1-2. "Design of Concrete Structures Part 1-2: General Rules Structural Fire Design", CEN European Committee for Standardization, Brussels. https://www.phd.eng.br/wp-content/uploads/2015/12/en.1992.1.2.2004.pdf
- [9]. Hager, I., & Dimienta, P. (2004, September). The impact of the addition of polypropylene fibres on the mechanical properties of high-performance concretes exposed to high temperatures. In 6th International RILEM Symposium on Fibre Reinforced Concretes (pp. 575-582). https://www.rilem.net/publication/publication/44?id_papier=689
- [10] Kriker, A., Debicki, G., Bali, A., Khenfer, M.M., & Debicki, M. (2005). Mechanical properties of date palm fibres and concrete reinforced with date palm fibres in hot-dry climate. Cement and Concrete Composites, 27(5), 554-564. https://doi.org/10.1016/j.cemconcomp.2004.09.015
- [11] Gideon, R., & D. (2022). Mechanical and water absorption properties of Jute/Palm leaf fiber-reinforced recycled polypropylene hybrid composites. International Journal of Polymer Science, 2022. https://doi.org/10.1155/2022/4408455
- [12] Hamda, M., Guergah, C., & Benmarce, A. (2025). The Impact of Natural Fibers on Thermal Resistance and Spalling in High-performance Concrete. Periodica Polytechnica Civil Engineering, 69(1), 84-97.
- [13] Dias, W. P. S., Khoury, G. A., & Sullivan, P. J. E. (1990). Mechanical properties of hardened cement paste exposed to temperatures up to 700 C (1292 F). Materials Journal, 87(2), 160-166. https://doi.org/10.14359/1981
- [14] Mindeguia, J. C., Pimienta, P., Noumowé, A., & Digital Experimental and numerical discussion on spalling risk. Cement and concrete

- research, 40(3), 477-487. https://doi.org/10.1016/j.cemconres.2009.10.011
- [15], Kuswa, F. M., & Darmawan, A. (2023, April). Investigation of Slagging Fouling Aspect of Palm Fiber and Palm Leaves Waste in Drop Tube Furnace. In 6th Mechanical Engineering, Science and Technology International conference (MEST)
- 2022) (pp. 15-23). Atlantis Press. https://doi.org/10.2991/978-94-6463-134-0_3
- [16] Xiao, J., Xie, Q., & D., Xie, W. (2018). Study on high-performance concrete at high temperatures in China (2004–2016)-An updated overview. Fire safety journal, 95, 11-24. https://doi.org/10.1016/j.firesaf.2017.10.007
- [17] Zhang, B. (2011). Effects of moisture evaporation (weight loss) on fracture properties of high-performance concrete subjected to high temperatures. Fire Safety Journal, 46(8), 543-549.https://doi.org/10.1016/j.firesaf.2011.07.010

- [1] EN 1992-1-1-2004, Eurocode 2. Calcul des structures en béton Partie 1-1 : Règles générales et règles pour les bâtiments. Comité Européen de Normalisation (CEN), Brussels, 2004.
- [2] EN 1994-1-2-2005, Eurocode 4. Calcul des structures mixtes acier-béton-Partie1-2: Règles générales Calcul du comportement au feul. Comité Européen de Normalisation (CEN), Brussels, Août 2005.
- [3] Franssen, J.M. (2005). SAFIR: A thermal/structural program for modeling structures under fire ". Engineering Journal A.I.S.C, 42(3), pp. 143-158.
- [4] Franssen, J.M. and Gernay, T. (2017) Modelling structures in fire with SAFIR: Theoretical background and capabilities . Journal of Structural Fire Engineering, 8(3), pp. 300-323.
- [5] Kodur, V. K. R., Nwosu, D. I., Sultan, M. A., and Franssen, J. M. (1999). Application of the SAFIR computer program for evaluating fire resistance ". In Proceedings third international conference on fire research and engineering, SFPE-NIST-IAFSS, Chicago,pp. 287-295.
- [6] Nwosu, D. I., Kodur, V. K. R., and Franssen, J. M., and Hum, J. K. (2007). SAFIR-A Computer-Program for Analysis of Structures at Elevated Temperature Conditions ". University of Liege, Belgium.
- [7] Franssen, J.M., Schleich, J.B., Cajot, L.G., Talamona, D., Zhao,B., Twilt,L. and Both,K. (1994) A comparison between five structural fire codes applied to steel element". Fourth International Symposium on Fire Safety Science, Ottawa, pp.1125-1136
- [8] Pintea,D. and Franssen,J.M.(1997). Evaluation of the thermal part of the code SAFIR by comparison with the code TASEF ". Proceeding of the eighth international conference on steel structures, volume 2, M. Ivan ed., MIRTON, Timisoara, pp.636-643.
- [9] Talamona, D. and Franssen, J.M. (2002-2003). Nonlinear Thin Shell Finite Element for Steel and Concrete Structures Subjected to Fire: Theoretical Development ". Journal of Applied Fire Science, Baywood Publishing Company Inc., Vol. 11, N°4, pp. 291-310.
- [10] Kodur, V.K.R. and Dwaikat, M.M.S. (2008). A Numerical Model for Predicting the Fire Resistance of Reinforced Concrete Beams. Cement and Concrete Composites, 30(5), 431 443.
- [11] Binh, C. T. (2009). hollow steel section columns filled with self-compacting concrete under ordinary and fire conditions ". Thèse de doctorat en sciences de l'ingénieur université de liège, Belgique.
- [12] Wu, B., Li Y.H., and Chen, S.L. (2010). Effect of heating and cooling on axially restrained RC columns with special-shaped cross section ". Fire Technology, Vol 46 (1), pp. 231-249.générales Actions du vent".
- [13] Schneider, U. (1985) Properties of material at high temperatures-concrete. RILEM-Committee 44-PHT. Department of Civil Engineering, University of Kassel, Germany.

[14] Li, Y.H., and Franssen, J. M. (2011). Test results and model for the residual compressive strength of concrete after a fire. Journal of Structural Fire Engineering, vol 2(1), pp. 29-44. [15] Felicetti, R., Gambarova, P.G., Silva, M., and Vimercati, M. (2002). Thermal diffusivity and Residual Strength of High-Performance Light-Weight Concrete Exposed to High Temperature. 6th Int. Symp, on Utilization of HSC/HPC, Leipzig, pp.935-948. [16] GUERGAH C. (2025). Practical Guide for Calculating Reinforced Concrete Sections: According to BAEL 91 Modified 99. Elyaa Publishing House.

Annex



NOTICE PRODUIT

Sika® Fibre 12-34

Fibre polypropylène spéciale pour béton

INFORMATIONS SUR LE PRODUIT

Sika® Fibre 12-34 est constituée de fibres de polypropylène multifilament 100% vierge de haute qualité spécialement traitées pour faciliter leur dispersion. Elle se présente en sacs palpables pré-dosés pour béton ou micro-béton.

Elle est conçue aussi pour la prévention de l'écaillage du béton en cas d'incendie. Au-delà de cela, il réduit l'apparition de retrait plastique et de fissuration par tassement plastique tout en améliorant les propriétés de surface et la durabilité d'une matrice cimentaire dans les climats chauds. Sika® Fibre 12-34 est enrobé d'un tensioactif pour améliorer la dispersion initiale et une bonne liaison avec la pâte de ciment. Ce produit est adapté pour une utilisation dans des conditions climatiques tropicales et chaudes.

DOMAINES D'APPLICATION

Sika® Fibre 12-34 est utilisé pour les bétons courants:

- Dalles et Dallages
- Eléments préfabriqués
- Eléments de voirie (chaussée, trottoirs et rampes
- d'accès) · Chape én micro-béton

fibres fondent à l'intérieur du béton, créant les vides nécessaires pour que la vapeur s'échappe, empêchant ainsi l'écaillage et préservant ainsi l'intégrité de l'élément structurel:

- Béton, principalement lorsque le HPC et le béton à faible perméabilité sont spécifiés, en raison des pressions interstitielles plus élevées qui s'accumulent pendant le chauffage
- Voussoirs de tunnel en béton préfabriqué
- Béton soumis à des températures très élevées

CARACTÉRISTIQUES / AVANTAGES

- Améliore la cohésion à l'état frais
- Limite le faïençage et des fissurations dues au retrait
- plastique Augmente la résistance aux chocs
- Offre une meilleure imperméabilité à l'état durci
- Réduit les risques de ségrégation et de ressuage
- Garde l'intégrité de l'ensemble de la structure en cas d'incendie
- Réduit les coûts de réparation futurs
- Fournit une protection passive contre le feu pour le béton projeté et le béton coulé et une solution extrêmement rentable par rapport aux alternatives telles que les revêtements projetés ou les méthodes de

DESCRIPTION DU PRODUIT

Base chimique	Polypropylène			
Conditionnement	Dose de 600 g de sac hydrosoluble fournie en boîtes de 35 sacs			
Durée de Conservation	24 mois de la date de production si le produit est stocké correctement dans son emballage d'origine non ouvert.			
Conditions de Stockage	Conserver dans un endroit sec dans son emballage d'origine intact et scelle à des températures comprises entre + 5°C et + 35°C. Protéger de la lu- mière directe du soleil et de la chaleur.			
Aspect / Couleur	Fibre blanche			
Dimensions	Longueur	~12 mm		
	Diamètre	~34 μm		
Densité	~0.91 kg/l (+25 °C)			
Point de Fusion	~160 °C			

INFORMATIONS TECHNIQUES

Résistance à la Traction	Étirement amélioré 300-400 N/mm²		
Allongement à la Rupture	≥ 120%		
Résistance à l'Alcalinité	100 %		

Dosage	Sika® Fibre 12-34 est prêt à l'emploi.
	Pour bétons courants: 1 dose de 600 g pour 1 m³ de béton ou de micro-
	béton.
	Pour la prévention de l'écaillage du béton en cas d'incendie : La détermi- nation précise de la dose minimale de fibres pour fournir une résistance à
	l'éclatement explosif ne peut être établie que par des essais au feu à grande échelle du béton à utiliser sur un projet spécifique. À titre de référence, la section 6.1 de la norme européenne EN 1992 Eurocode 2 fait ré-
	férence à l'utilisation de 2 kg/m³ de fibres de polypropylène pour contrôle
	l'écaillage explosif dans le béton à haute résistance. Ce dosage fournira une très bonne marge de sécurité, mais n'empêche pas l'utilisation de
	doses plus faibles lorsque des essais au feu sur de gros échantillons de bé- ton ont été effectués. Des doses de 1,5 kg/m³ ou moins ont été utilisées après des essais précis.
	apres des essais precis.

VALEURS DE BASE

Toutes les valeurs indiquées dans cette Notice Produit sont basées sur des essais effectués en laboratoire. Les valeurs effectives mesurées peuvent varier du fait de circonstances indépendantes de notre contrôle.

ÉCOLOGIE, SANTÉ ET SÉCURITÉ

Pour obtenir des informations et des conseils sur la manipulation, le stockage et l'élimination en toute sé-curité des produits chimiques, les utilisateurs doivent consulter la fiche de données de sécurité (FDS) la plus récente contenant les données physiques, écologiques, toxicologiques et autres données relatives à la

RESTRICTIONS LOCALES

Veuillez noter que du fait de réglementations locales spécifiques, les données déclarées pour ce produit peuvent varier d'un pays à l'autre. Veuillez consulter la Notice Produit locale pour les données exactes sur le produit.

INFORMATIONS LÉGALES

Les informations, et en particulier les recommanda-

Notice produit Sika® Fibre 12-34 Juillet 2023, Version 01.04 021408021010000102



tions concernant les modalités d'application et d'utilisation finale des produits Sika sont fournies en toute bonne foi et se fondent sur la connaissance et l'expérience que Sika a acquises à ce jour de ses produits lorsqu'ils ont été convenablement stockés, manipulés et appliqués dans des conditions normales, conformément aux recommandations de Sika. En pratique, les différences entre matériaux, substrats et conditions spécifiques sur site sont telles que ces informations ou recommandations écrites, ou autre conseil donné, n'impliquent aucune garantie de qualité marchande autre que la garantie légale contre les vices cachés, ni aucune garantie de conformité à un usage particulier, ni aucune responsabilité découlant de quelque rela-tion juridique que ce soit. L'utilisateur du produit doit vérifier par un essai sur site l'adaptation du produit à l'application et à l'objectif envisagés. Sika se réserve le droit de modifier les propriétés de ses produits. Notre responsabilité ne saurait d'aucune manière être engagée dans l'hypothèse d'une application non conforme à nos renseignements. Les droits de propriété détenus par des tiers doivent impérativement être respectés. Toutes les commandes sont soumises à nos conditions générales de vente et de livraison en vigueur. Les utilisateurs doivent impérativement consulter la version la plus récente de la Notice Produit correspondant au produit concerné, accessible sur internet ou qui leur sera remise sur demande.

Sika El Djazair SPA 08 route de Larbaa 16111 Les Eucalyptus

ALGERIE Tél.: 0 23 88 89 92 09 Fax: 0 23 88 89 92 08 dza.sika.com







Notice produit Sika® Fibre 12-34 Juillet 2023, Version 01.04 021408021010000102 SikaFibre12-34-fr-DZ-(07-2023)-1-4.pdf





NOTICE PRODUIT

Sika® ViscoCrete® TEMPO-12

Superplastifiant/Haut Réducteur d'eau polyvalent pour bétons prêts à l'emploi.

INFORMATIONS SUR LE PRODUIT

Sika® ViscoCrete® TEMPO-12 est un superplastifiant/haut réducteur d'eau polyvalent de nouvelle génération non chloré à base de copolymère acrylique.

DOMAINES D'APPLICATION

- Sika® ViscoCrete® TEMPO-12 permet la fabrication de bétons plastiques à autoplaçants transportés sur de longues distances et pompés.
- Dans les bétons autoplaçants, Sika® ViscoCrete® TEMPO-12 améliore la stabilité, limite la ségrégation du béton et rend les formules moins susceptibles aux variations d'eau et des constituants.

CARACTÉRISTIQUES / AVANTAGES

Sika® ViscoCrete® TEMPO-12 est un superplastifiant puissant qui confère aux bétons les propriétés suivantes :

- longue rhéologie (>2h),
- robustesse à la ségrégation,
- qualité de parement.

AGRÉMENTS / NORMES

Marquage CE et NF selon la norme NF EN 934-2 tab $3.1\,\mathrm{et}\,3.2.$

PV CNERIB: DTEM/108/2017

DESCRIPTION DU PRODUIT

Conditionnement	Fût de 230 kgCubi de 1100 kgVrac
Durée de Conservation	12 mois dans son emballage d'origine intact.
Conditions de Stockage	A l'abri du gel. En cas de gel accidentel, le produit retrouve ses qualités d'origine une fois dégelé lentement et réhomogénéisé.
Aspect / Couleur	Liquide brun clair à foncé
Densité	1,06 ± 0,01
Valeur pH	4,5 ± 1,0
Teneur Totale en Ions Chlorure	≤ 0,1 %
Équivalent Oxyde de Sodium	≤1%

Notice produit Sika® ViscoCrete® TEMPO-12

RENSEIGNEMENTS SUR L'APPLICATION

Dosage Plage de dosage : 0,2 à 3,0% du poids du liant ou du ciment selon la fluidité

et les performances recherchées.

Plage d'utilisation usuelle : 0,4 à 1,5 % du poids du ciment ou du liant.

VALEURS DE BASE

Toutes les valeurs indiquées dans cette Notice Produit sont basées sur des essais effectués en laboratoire. Les valeurs effectives mesurées peuvent varier du fait de circonstances indépendantes de notre contrôle.

ÉCOLOGIE, SANTÉ ET SÉCURITÉ

Pour obtenir des informations et des conseils sur la manipulation, le stockage et l'élimination en toute sécurité des produits chimiques, les utilisateurs doivent consulter la fiche de données de sécurité (FDS) la plus récente contenant les données physiques, écologiques, toxicologiques et autres données relatives à la sécurité.

INSTRUCTIONS POUR L'APPLICATION

Sika® ViscoCrete® TEMPO-12 est ajouté, soit en même temps que l'eau de gâchage, soit en différé dans le béton préalablement mouillé avec une fraction de l'eau de gâchage.

RESTRICTIONS LOCALES

Veuillez noter que du fait de réglementations locales spécifiques, les données déclarées pour ce produit peuvent varier d'un pays à l'autre. Veuillez consulter la Notice Produit locale pour les données exactes sur le produit.

INFORMATIONS LÉGALES

Les informations, et en particulier les recommandations concernant les modalités d'application et d'utilisation finale des produits Sika sont fournies en toute bonne foi et se fondent sur la connaissance et l'expérience que Sika a acquises à ce jour de ses produits lorsqu'ils ont été convenablement stockés, manipulés et appliqués dans des conditions normales, conformément aux recommandations de Sika. En pratique, les différences entre matériaux, substrats et conditions spécifiques sur site sont telles que ces informations ou recommandations écrites, ou autre conseil donné, n'impliquent aucune garantie de qualité marchande autre que la garantie légale contre les vices cachés, ni aucune garantie de conformité à un usage particulier, ni aucune responsabilité découlant de quelque relatinanijuridinse que ce soit. L'utilisateur du produit doit veridie அள்ள essai sur site l'adaptation du produit à l'application vetsà l'objectif envisagés. Sika se réserve le dশঙাই de modifier les propriétés de ses produits. Notre responsabilité ne saurait d'aucune manière être engagee dans in your application non conforme à nos renseignements. Les droits de propriété détenus







Notice produit Sika® ViscoCrete® TEMPO-12 Juillet 2023, Version 01.03 021301011000000110 par des tiers doivent impérativement être respectés. Toutes les commandes sont soumises à nos conditions générales de vente et de livraison en vigueur. Les utilisateurs doivent impérativement consulter la version la plus récente de la Notice Produit correspondant au produit concerné, accessible sur internet ou qui leur sera remise sur demande.

SikaViscoCreteTEMPO-12-fr-DZ-(07-2023)-1-3.pdf

